TIME-DOMAIN ULTRA-WIDE BAND MICROWAVE MEASUREMENT TECHNIQUES FOR MINIATURIZED DIELECTRIC SPECTROSCOPY AND CHIPLESS RFID SYSTEMS

A Dissertation

by

REZA EBRAHIMI GHIRI

Submitted to the Office of Graduate and Professional Studies of
Texas A&M University
in partial fulfillment of the requirements for the degree of

DOCTOR OF PHILOSOPHY

Chair of Committee,	Kamran Entesari
Committee Members,	Samuel Palermo
	Robert D. Nevels
	Jay R. Porter
Head of Department,	Miroslav M. Begovic

December 2020

Major Subject: Electrical Engineering

ABSTRACT

Dielectric spectroscopy is a versatile experimental technique for identifying materials based on their electrical properties. Dielectric spectroscopy measures complex relative permittivity of materials as a function of frequency. Time-domain dielectric spectroscopy is a fast, simultaneous, and highly accurate technique for unique detection and characterization of materials over broad frequency ranges. In time-domain technique, the complete characterization of material is rapidly obtained by using a short-duration excitation pulse that simultaneously contains all the desired frequencies.

In this study, three miniaturized time-domain dielectric spectroscopy systems are presented for material sensing in ultra-wide band frequency range. The first system is a contactless spectroscopy system based on using a pair of Vivaldi antennas located in the near-field region for sensing liquid materials. The response of this sensing unit is measured in a combined time-frequency-domain system as well as a pure time-domain system. The second system is a miniaturized contact-based spectroscopy system that uses planar wide band sensors with a few μL amount of test material for sensing in a wide dynamic range. The contact-based sensor is initially designed for phase measurement and in an extended version for phase and magnitude measurement of material responses. The third system is based on dual-comb spectroscopy technique. In dual-comb spectroscopy, the microwave properties of test material is mapped to the baseband frequency that significantly reduces the receiver complexity. The implementation and experimental results of the above-mentioned time-domain spectroscopy systems are reported.

In addition, a high capacity chipless RFID tag for identification is presented in this research. Chipless RFID tags are passive and printable structures with unique electromagnetic signatures that are considered as substitutes for traditional barcodes and as alternatives to chipped RFID tags. Moreover, three chipless RFID readers in time-domain including IR-UWB, chirped pulsed Fourier transform microwave, and dual-comb technique are demonstrated for identifying the chipless RFID tag.

DEDICATION

To my father, my mother, and my sister Mohaddeseh.

ACKNOWLEDGMENTS

First and above all, I praise God, the almighty for providing me this opportunity and granting me the capability to proceed successfully. This research would have taken far longer to complete without the encouragement from many others. It is a delight to acknowledge those who have supported me over the last four years.

I am grateful to my supervisor, Professor Kamran Entesari, for his guidance through each stage of my PhD program. Your insightful feedback pushed me to sharpen my thinking and brought my work to a higher level. I would like to extend my thanks to my Committee members Professor Jay Porter, Dr. Samuel Palermo, and Dr. Robert Nevels.

I very much appreciated the academic support of Professor Jay Porter, Professor Behbood Zoghi, Professor Walter Buchanan, Professor Wei Zhan, Mr. Pat Wallace, Dr. Rainer Fink, Dr. Ana Goulart, and Dr. John Bosshard whom I have worked for them as graduate teaching assistant.

I would like to acknowledge my colleagues at Professor Entesari Group for their wonderful collaboration in analyzing and measurement of various systems developed in this work.

Finally, I wish to thank my parents for their wise counsel and sympathetic ear. You are always there for me.

CONTRIBUTORS AND FUNDING SOURCES

Contributors

This work was supported by Professor Kamran Entesari of the Department of Electrical & Computer Engineering.

The contactless antenna design in Chapter 2, Section 2.1.2.1, was performed by the second author in [1]. The simulations and measurements conducted in Chapter 2, Section 2.1.1 were conducted with the help of the third author in [1].

All other work conducted for the dissertation was completed by the student independently.

Funding Sources

This work was completed without outside financial support

NOMENCLATURE

MUT	Material Under Test
TDS	Time-domain Dielectric Spectroscopy
TD	Time Domain
FD	Frequency Domain
VNA	Vector Network Analyzer
FFT	Fast Fourier Transform
UWB	Ultra-wide Band
DCS	Dual-comb Spectroscopy
RFID	Radio Frequency Identification
IDC	Interdigital Capacitor
BDS	Broadband Dielectric Spectroscopy
IF	Intermediate Frequency
LO	Local Oscillator
HFSS	High-frequency Structure Simulator
SRD	Step Recovery Diode
MSE	Mean-squared Error
PET	Polyethylene Teraphalate
PP	Polypropylene
HPF	High-pass Filter
LPF	Low-pass Filter
PRF	Pulse Repetition Frequency
BB	Baseband

CNC	Computer Numerical Control
DAC	Digital-To-Analog Converter
ADC	Analog-To-Digital Converter
REF	Reference
IFFT	Inverse Fast Fourier Transform
IR	Impulse Radio
CPFT-MW	Chirped-pulse Fourier Tranform-Microwave
AWG	Arbitrary Waveform Generator
FSS	Frequency Selective Surface
MEFSS	Miniaturized Element Frequency Selective Surface

TABLE OF CONTENTS

Page

LIST OF FIGURES

FIGURE Page

LIST OF TABLES

TABLE Page

1. INTRODUCTION

1.1 Miniaturized Ultra-wideband Time-domain Dielectric Spectroscopy Systems

Microwave broadband dielectric spectroscopy is a powerful experimental method for unique characterization of materials based on their dielectric properties. This technique precisely extracts the complex relative permittivity, $\epsilon^* = \epsilon' - j\,\epsilon''$, of a material under test (MUT) versus frequency according to the interaction of the MUT with an external microwave electric field. Microwave broadband dielectric spectroscopy has been proven to be highly valuable due to the fact that the dielectric property of materials over a broad range of frequencies is unique for each material, and therefore, a relatively straightforward material sensing and characterization can be performed with a low cost. This area has actively been the focus of research for about a few decades due to its vast areas of applications such as biomedical, food and drug safety, oil industry, and chemical/biological sensing [10, 11, 12, 13, 14].

Time-domain dielectric spectroscopy (TDS) is an important technique for measuring the complex permittivity of MUTs over a wide frequency range. In TDS, a short duration pulse with a wide bandwidth is sent through an MUT and the reflected or transmitted signal from the MUT is captured in time domain (TD). The captured information contains broadband dielectric properties of the MUT. TDS can be considered as an alternative for frequency-domain (FD) spectroscopy techniques that are commonly utilized for broadband sensing using a vector network analyzer (VNA). In FD techniques, the resolution of the captured data depends on the frequency sweep step, while for most of the TD methods it is contingent upon the length of excitation pulse and fast Fourier transform (FFT) postprocessing of the TD data.

This thesis consists of three miniaturized TDS systems for characterization of MUTs in 3–10 GHz ultra-wide band (UWB) frequency range.

The first system is a contactless sensing system that uses combination of TD and FD techniques for measuring the frequency response of MUTs [2]. A contactless sensing system can be

applied for measuring hazardous materials like acidic liquids, and it is long-lasting and cost effective because the sensing unit is separate from the electronic circuits which makes the sensor and the MUT container replicable and reusable. The miniaturization and contactless sensing in UWB are achieved by using two Vivaldi antennas placed in the near-field distance of each other for sensing a liquid MUT located in between. An extended version of this system proposed based on a pure TD technique [1]. In the extended version, a 3–10 GHz pulse input is utilized for measuring the UWB properties of MUT by only a single measurement. The full characterization of liquid MUTs is reported by using this system.

The second system is a miniaturized contact-based dielectric spectroscopy system that employs printed sensors with periodic structures for sensing MUTs in UWB range [4]. Although in [4], the system can only measure the phase response of different MUTs, in an extended version [5], the sensor is optimized for measurement of both magnitude and phase response of MUTs by only using 0.3 μL of the MUT. The complete characterization of liquid MUTs is reported by using the measurement results of this system.

The third system is based on dual-comb spectroscopy (DCS) technique that enables fast, miniaturized, self-sustained, and low-cost sensing system with the possibility of being self-sustained and independent of laboratory facility [6]. With DCS technique, the microwave UWB properties of the MUT is mapped to the baseband frequency significantly reducing the receiver complexity. In an extended version of the DCS system [7] that operates with mutually coherent sources, the complex permittivity of ethanol, methanol, and their mixtures are extracted by using the results of this system and through calibration.

For the three systems introduced above, the system design, sensor design, fabrication and measurement results, calibration and characterization of unknown MUTs are presented in chapter 2.

1.2 Chipless RFID Systems

Chipless radio frequency identification (RFID) is a smart, robust, and low cost solution for identification and sensing. Chipless RFID tags are passive and printable electromagnetic structures that are considered as substitutes for traditional barcodes and as alternatives to chipped RFID

tags. The chipless (/chipped) RFID shows its usefulness in a wide range of applications including item tracking, transportation, supply chain management, asset management, security and access control, and point-of-sales systems. The development of miniaturized and high-capacity chipless RFID tags has attracted immense attention in the past decade. In this thesis, a high capacity 50.7-bit retransmission-based chipless RFID tag with miniaturized resonators is presented. 32 resonators each consisting of an interdigital capacitor (IDC) in parallel with a meander inductor build miniaturized LC resonators placed next to a microstrip line. Beside 32 resonance positions designed from 3.4 GHz to 10 GHz, Q of each resonator is also coded in two separate states by adjusting the LC distance from the microstrip line. Therefore, each frequency position has three states: (i) no resonance, (ii) low Q, and (iii) high Q that generates 50.7 bits for the tag.

In addition to the tag, every chipless RFID system requires a microwave UWB reader to interrogate the tag by a UWB transmitter and then acquires the reflected response form the tag by a UWB receiver. Unlike the chipless RFID tags, there is limited research about UWB chipless RFID readers. The focus of Chapter 3 is implementation of the high capacity Chipless RFID tag comparison of time-domain UWB chipless RFID readers and proposing the dual-comb reader as a novel technique for Chipless RFID application.

2. TIME-DOMAIN DIELECTRIC SPECTROSCOPY SYSTYEMS*

2.1 Contactless UWB Microwave Dielectric Spectroscopy System

Contact-less material characterization has multiple advantages compared with the contact-based counterpart specially when the MUT sample is in liquid form. First, having contact between a liquid and the sensing unit can make the sensor hardly re-usable. In this case, the sensing unit needs to be replaced after each measurement trial, which makes the contact-based approaches more expensive. On the other hand, in the case of contact-less sensing, only the cuvette carrying the MUT needs to be replaced, which is significantly more cost effective. Another advantage of having the MUT in a cuvette, and performing the material characterization in contact-less fashion is that the user requires minimum special expertise to perform the experiment as the sensing unit remains the same in all measurement trials, and only the cuvette and the MUT need to be changed. Moreover, in some cases, the material could be hazardous, i.e. acidic liquids, or it might leak to some other parts of the sensor circuitry, and therefore it damages the entire system electronics. As a result, contact-less sensing has attracted attention over the recent years.

Free-space techniques are commonly used for contact-less measurement of dielectric properties of materials [15, 16, 17, 18]. These techniques are mainly based on using two antennas placed

in the far-field and faced in each other with the MUT in the middle. Horn antennas are most commonly utilized for this purpose [15]. In [16], two microstrip quasi-horn antennas are utilized for UWB sub-surface sensing suitable for ground penetrating radar applications. The far-field techniques can also be implemented with a single antenna, and based on measuring the reflection back from the MUT [19]. In all these contact-less sensing approaches performed at microwave range, the antennas' dimensions, the required volume of the sample MUT, and the overall setup sizes are significantly large. Therefore, such systems are unable to characterize liquid materials with small volumes within few mm^3 range. In order to achieve a more compact contact-less setup size, with relatively lower volume of the MUT, free-space techniques are applied at millimeter-wave (mm-wave) range [18, 17]. Despite their smaller setup size, such systems are unable to characterize the materials at microwave frequencies and many materials, i.e. biomaterials [20], are solely responsive at microwave range. As a result, a miniaturized UWB contact-less sensing system with the fast time-domain measurement procedure performing at microwave range seems demanding. In order to achieve contact-less broad-band microwave sensing suitable for time-domain material characterization with a compact setup size, and relatively low volume of the sample, near-field sensing is proposed as a solution.

2.1.1 Combination of Time-Domain and Frequency-Domain Techniques

In this section, a contact-less broadband dielectric spectroscopy system with a combined frequency-domain/time-domain technique for 3–10 GHz frequency range is presented.

2.1.1.1 Introduction

The broadband dielectric spectroscopy (BDS), with its label-free nature, is a powerful technique for unique characterization of materials under test MUT. Therefore, it has been em-ployed for a wide variety of applications such as chemical/biological sensing, disease diagnosis, and food safety [21].

Existing microwave BDS techniques are performed in either FD or TD. FD spectroscopy can achieve high detection resolution, but distinct calibra-tion at each single frequency is necessary

which makes this technique time consuming [22]. On the other hand, TD spectroscopy is fast and provides information in a wide frequency span with single measurement, and achieves high signal to noise ratio by averaging the many scans taken for a given sample [13]. However, both TD and FD systems require expen-sive bulky sources and high speed signal analyzers. To address this issue, several miniaturized FD spectroscopy systems have been reported at microwave range [21, 23]. In these systems, the fluidic carrying the MUT is in direct contact with the sens-ing element making its replacement a challenge. On the other hand, reported TD contact-less sensing units are either large at microwave range [16] or designed for mm-wave applications to have a compact setup [17]. However, many materials have responsive dielectric behavior to microwave excitation and do not show dispersive properties at mm-wave range.

In this section, a contact-less 3-10 GHz BDS system is pro-posed based on a combined FD/TD technique. It is imple-mented by generating a 450 MHz bandwidth baseband pulse and then up-converting it to only 9 number of microwave sub-bands within 3-10 GHz frequency range one at a time, passing each upconvereted pulse through MUT and detecting the output signal using a UWB receiver. This approach addresses the time-consuming nature of all FD measurements by taking advantage of TD measurement properties. Also, to realize a miniaturized contact-less sensor at microwave frequencies, two UWB Vivaldi antennas are coupled in their radiative near-field with MUT placed in the middle, to achieve a compact-size and a flat group delay and proper impedance matching over 3-10 GHz.

2.1.1.2 System Design and Implementation

2.1.1.2.1 System Analysis

The block diagram of the proposed contactless UWB spectroscopy system is shown in Fig. 2.1. This system consists of a contactless sensing unit, a UWB direct-conversion transmitter, and a UWB low-IF receiver. The changes in phase and magnitude of a signal passing through the sensing unit are related to ϵ' and ϵ'' properties of the MUT. The effects of sensing unit, transmitter, and receiver on the transmitted signal will be cancelled out by subtracting the output of the system from a reference test (container filled with air, without any MUT); thus, the proposed system

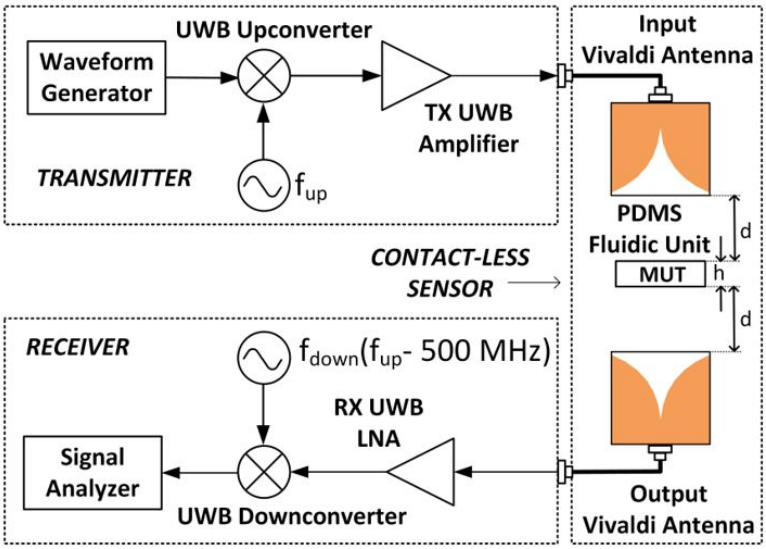

Figure 2.1: Block diagram of the proposed contact-less dielectric spectroscopy system. Reprinted with permission from [2].

reflects only the properties of MUTs.

The direct-conversion UWB transmitter including upcon-verter (mixer and local oscillator) and amplifier, is compact, has flat gain and group delay in the frequency range of 3-10 GHz. It is optimal to send only one UWB signal in the span of 3- 10 GHz to measure the dielectric properties of MUT with a single test; however, the sampling constraints of available digital-to-analog converter (1250 MSps) generating the baseband UWB signal, limits the transmitted signal bandwidth. Therefore, the transmitter generates a 450 MHz baseband signal and upconverts it to nine sub frequency bands within the frequency range of 3-10 GHz (combined FD/TD approach). To overcome the flicker noise effect at the receiver and avoid self-corruption of the asymmetric received signal due to material dispersion, low-IF receiver (f_{IF} = 500 MHz) architecture consisting of a UWB amplifier and downconverter is targeted. To achieve the minimum number of measurements with an efficient frequency planning, the local oscillator in the transmitter (LO_{TX}) generates frequencies of 3.4, 4.2, 5, 5.8, 6.6, 7.4, 8.2, 9, and 9.8 GHz, while the receiver one (LO_{RX}) produces frequencies of $f_{LO,TX}$-500 MHz. Furthermore, LO amplitudes are large enough (+18 dBm for LO_{TX} and +10 dBm for LO_{RX}) to provide flat conversion gain and abrupt switching. Besides, isolations of

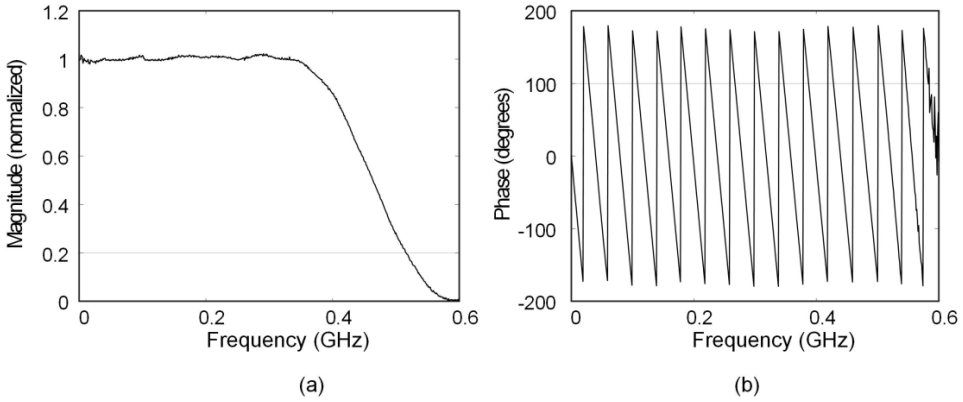

Figure 2.2: Generation of a flat frequency spectrum pulse by adding five Gauss-ian pulses (a) magnitude, (b) phase. Reprinted with permission from [2].

the up/down converters are high enough (about 30 dB) to eliminate the effects of LO-IF/ LO-RF leakages.

Gaussian pulse and its derivatives are generally used in UWB applications [24]. However, such pulses alone are not suitable for the proposed UWB system, since to detect the effect of the MUT on the magnitude of the input signal, a test signal with flat frequency spectrum all over the bandwidth is required. To generate such a signal, five Gaussian signals with 125 MHz 3-dB bandwidth at center frequencies of 0, 100, 200, 300 and 400 MHz are added. The amplitude and phase of the generated UWB pulse, captured by infiniium DSA91304A oscilloscope, are shown in Fig. 2.2. Comparing with a single Gaussian pulse, the phase of the new flat frequency spectrum signal shown in Fig. 2.2 (b) changes faster with frequency, which does not affect the phase detection accuracy while it has a flat amplitude response improving amplitude detection accuracy, or ϵ", of MUT. The group delays of the sensing unit and all the transmitter/receiver blocks need to have very small variations; therefore, the phase of the output signal only represents the dispersive properties, or ϵ', of MUT.

2.1.1.2.2 Contact-less Sensor

In order to achieve a contact-less UWB microwave sensor with a reasonably compact mea-

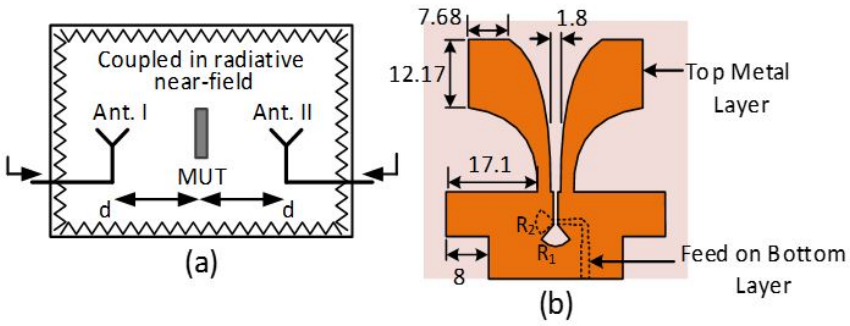

Figure 2.3: (a) Conceptual setup for time-domain UWB near-field sensing, (b) Top view of the printed UWB Vivaldi Antenna [3], R1, and R2 are 3.8 mm, and 3.1 mm (all other dimensions are in mm as well). Reprinted with permission from [2].

surement setup, time-domain near-field sensing is proposed. Fig. 2.3 (a) shows the conceptual setup of the proposed near-field solution. Two antennas are coupled to each other in their radiative near-field regions with the MUT placed in the middle. The whole setup is placed in a box with absorbing walls in order to minimize the reflections from the surrounding environment. Since the two antennas are not in the reactive near-field regions of each other, they have minimum effect on each others return loss characteristics. Each MUT perturbs the electromagnetic field around the two coupled an-tennas based on its dielectric properties, which can be detected and used for material characterization. The broad-band sensing element needs to be non-dispersive to be able to detect the dispersive properties of solely the MUT. Otherwise, any dispersion caused from the sensor itself results in distortion in the received signal, and makes post processing and calibration more cumbersome. As a result, two printed UWB Vivaldi antennas are utilized based on the structure first proposed in [3], due to their broad bandwidth, low cross polarization, and constant group delay. Fig. 2.3 (b) shows the top view of the utilized printed UWB Vivaldi antenna with both inner and outer edges tapered. Fig. 2.4 (a), and (b) show the simulated and measured S11 response of the antenna, and the simulated group delay over the interested frequency band, respectively. As can be seen, the antenna provides UWB operation with nearly constant group delay in each sub-band.

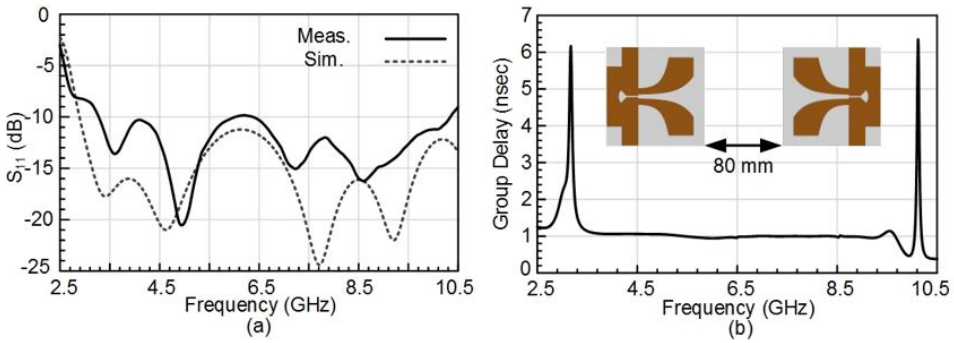

Figure 2.4: (a) Simulated, and measured S11, (b) simulated group delay of the printed UWB Vivaldi sensing antenna. Reprinted with permission from [2].

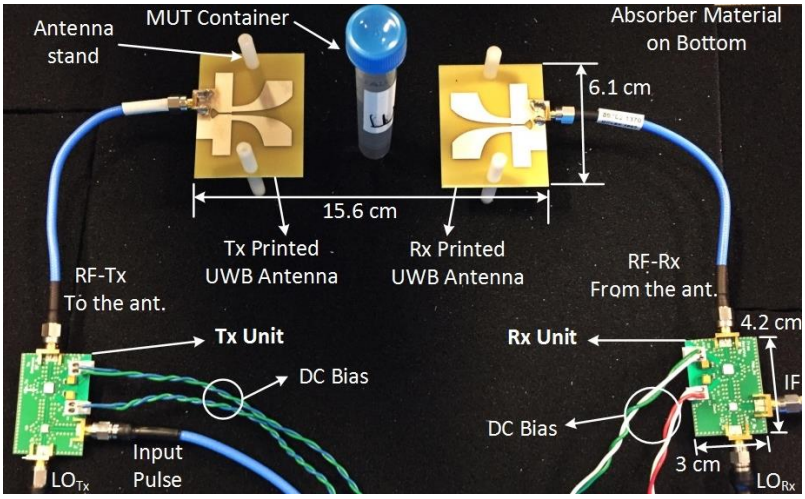

Figure 2.5: Photograph of the fabricated contactless UWB spectroscopy system. Reprinted with permission from [2].

2.1.1.3 Fabrication and Measurements

The contactless UWB dielectric spectroscopy system setup is shown in Fig. 2.5 The absorbing box around antennas was taken out for clarification. The transmitter and receiver are fabricated using Rogers 4350B substrate with $epsilon'$ = 3.66 and thickness of 0.338 mm, and both printed Vivaldi antennas are fabricated using standard FR4 substrate with ϵ' = 4.4 and thickness of 0.8 mm. The transmitter includes HMC787ALCB mixer and HMC772LC4 amplifier where the

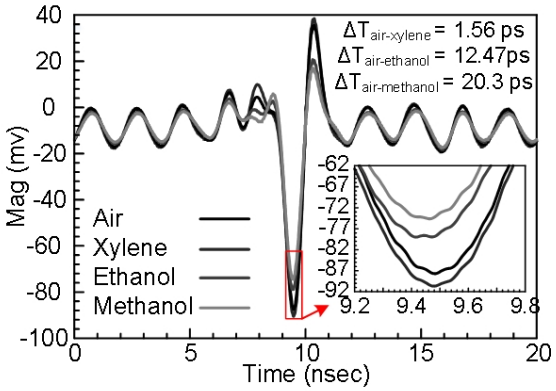

Figure 2.6: Measured received signal in time-domain, sub-band with 6.6 GHz center frequency. Reprinted with permission from [2].

E8267D PSG Vector Signal Generator is used as oscillator. The receiver uses the same amplifier and HMC1048LC3B mixer for downconversion. The radius of MUT cylindrical container depends on the pulse duration to prevent multiple reflections which distort the main transmitted pulse. In this work, a standard tube pipet (made from polypropylene with a diameter of 17 mm) is used as the liquid container between the two antennas.

The input signal with flat amplitude and linear phase prop-erties in frequency domain is applied using the N8241 arbitrary waveform generator. Fig. 2.6 shows the received signal in TD (upconverted to 6.6 GHz and downconverted with 6.1 GHz LO frequency). For different MUTs, distinct amplitudes and delays are observed. Fig. 2.7 (a), and 2.7 (b) show the measured amplitude and phase differences between air and three different MUTs (Xylene ,Ethanol, and Methanol). The measurement is repeated multiple times, and the results are averaged to consider any possible deviation between various trials. The measurement results are in good agreement with the direct measurements of vector network analyzer (VNA). Hence, the proposed system is able to characterize liquid MUTs over the entire UWB frequency band. The higher attenuation of are comapred with Xylene can be related to the shape of the tube container. In order to detect unknown liquids, a post-processing calibration procedure is required.

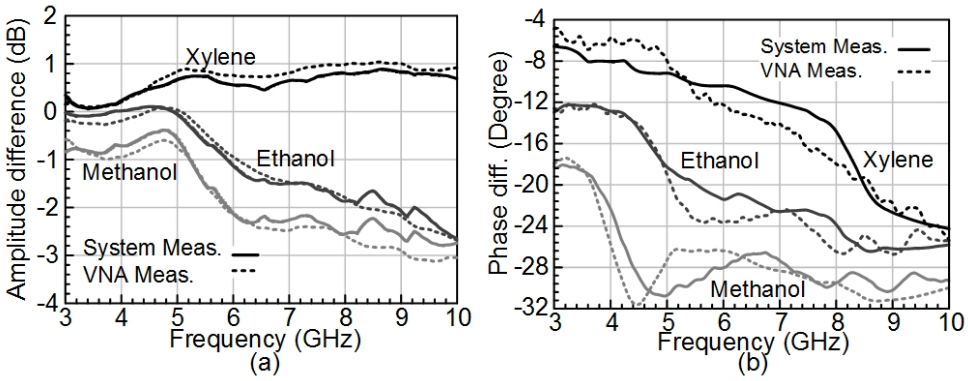

Figure 2.7: Difference between air and MUT measurements (a) in magnitude (dB) and (b) in phase. Reprinted with permission from [2].

2.1.1.4 Conclusion

A miniaturized contact-less UWB spectroscopy system is proposed. The system functionality is based on applying a combined FD/TD technique and using two near-field-coupled UWB antennas as sensing elements. As a result, various chem-icals were characterized successfully within 3-10 GHz band.

2.1.2 Pure Time-Domain Technique

A miniaturized time-domain dielectric spectroscopy system for contactless material characterization over the UWB microwave range is presented in this section. The proposed system includes a pulse generator, a transmitter, a compact contact-less sensing unit, and a receiver. The picosecond pulse generator unit delivers a quasi-monocycle pulse with 3.5GHz 10-dB bandwidth to the transmitter unit. The generated pulse provides the capability to perform the material characterization in a fast pure time-domain method. The transmitter unit provides the 3–10GHz excitation pulse based on utilizing a direct up-conversion architecture. The excitation pulse is transmitted to the receiver through the sensing unit. Two Vivaldi antennas are coupled to each other in their radiative near-field to construct the sensing unit, while the MUT is placed in between. A custom-designed Quartz-Glass cuvette is utilized with optimized MUT volume of $\sim$5 mL.

The details of contact-less sensor and pulse generation are given in next sections.

2.1.2.1 Contact-less Sensor

Fig. 2.8 (a) shows the conceptual setup of the proposed near-field solution. Two antennas are coupled in their near-field region while the MUT is placed in between. The setup is surrounded with absorbing materials (ECCOSORB AN) to provide an anechoic environment [19]. The near-field region of each antenna has two sub-regions; reactive, and radiative (Fresnel) regions. The former is in the immediate vicinity of the antenna, where the reactive fields predominate. In this case, the electric and magnetic fields are not necessarily in phase to each other, and the angular field distribution is highly dependent on the distance and direction away from the antenna. However, in the latter case the radiating fields predominate, and electric and magnetic fields are in phase. The angular field distribution in the Fresnel region still is highly dependent upon the distance from the antenna. In the proposed setup shown in Fig. 2.8 (a), the distance between the two antennas (d) needs to be adjusted accurately, so that the two antennas are coupled to each other in their Fresnel regions, and therefore, have minimum effect on each other's return loss characteristics. As a result, the overall size of the setup depends on the targeted frequency range, antenna size, and

its Fresnel region distance, which determines the value for d. Due to the complex electromagnetic field distribution in the Fresnel region full-wave simulations are required to finalize the overall dimensions of the setup adequately. The Fresnel region is commonly defined as follows [25]:

$$0.62\sqrt{\frac{D^3}{\lambda}} < R < \frac{2D^2}{\lambda}, \tag{2.1}$$

where, D is the largest dimension of the antenna, and λ is the operating wavelength. The separation of regions is also shown in Fig. 2.8 (b). Each MUT perturbs the near-field electromagnetic fields around the two coupled antennas based on its specific dielectric properties, which will be translated into phase and amplitude variations of S_{21}, and could be used for material detection and characterization.

The antenna type for the setup shown in Fig. 2.8 (a) requires to satisfy two main criteria. First, the system design is based on covering the complete 3-10 GHz UWB frequency range. Therefore, impedance matching within this band is needed for the sensing antennas. Second, the antenna element needs to be non-dispersive in order to be able to detect the dispersive properties of solely the MUT. Otherwise, any dispersion caused from the sensor itself results in error in reading, and makes post processing and calibration even more cumbersome. As a result, the sensing antenna has to provide UWB operation with relatively constant group-delay over the entire band. In this setting, the Vivaldi antenna is one of the best candidates due to its broad bandwidth, low cross-polarization, and constant group delay. Fig. 2.9 (a) shows the utilized printed UWB Vivaldi antenna first proposed in [3]. The antenna excitation, on the back side of the substrate, is a stepped microstrip line in order to cover the UWB frequency range. Both the inner and outer edges of the top metal patches are tapered to achieve the optimized group delay and impedance matching performance as discussed in [3].

The antenna is fabricated on FR-4 substrate with a dielectric constant of 4.4, and a thickness of 0.8 mm. Fig. 2.9 (b) shows the fabricated prototype using common single-layer printed circuit board (PCB) technology. Fig. 2.10 (a) shows the simulated and measured return losses of the

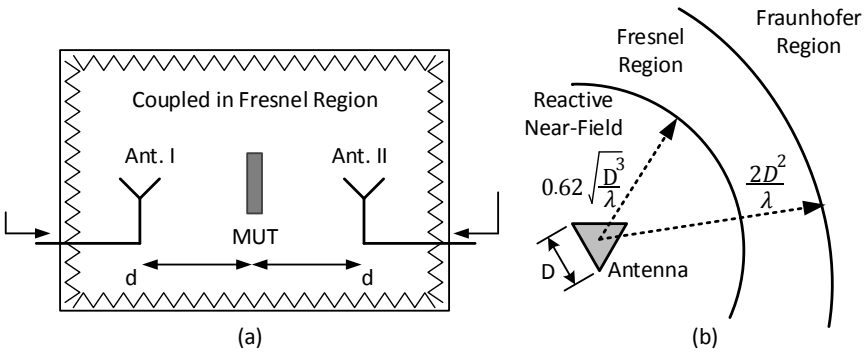

Figure 2.8: (a) conceptual contact-less sensor setup, (b) field regions of the antenna. Reprinted with permission from [1].

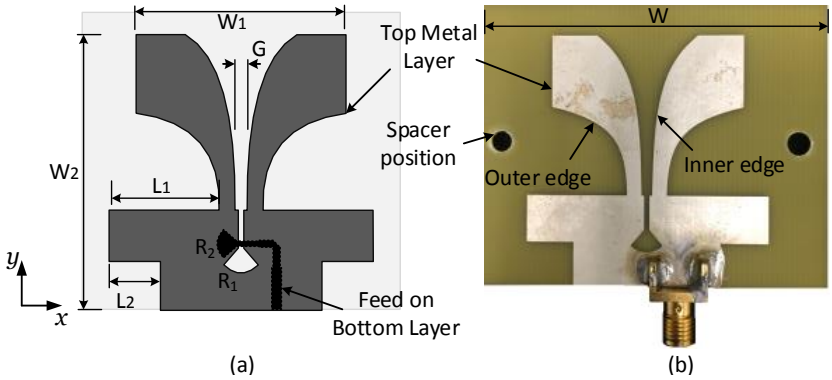

Figure 2.9: (a) printed UWB antenna used for contact-less sensing, and (b) the top view of the fabricated antenna prototype. The parameter values are: W = 41 mm, W_1 = 32.5 mm, W_2 = 42.7 mm, L_1 = 17.1 mm , L_2 = 8 mm , R_1 = 3.5 mm , R_2 = 2.85 mm. Reprinted with permission from [1].

designed Vivaldi antenna, which covers the interested bandwidth of 3-10 GHz. In order to extract the group delay of the utilized Vivaldi antenna in the proposed setup, first the distance between the two antennas (d) needs to be determined according to (2.1). The largest dimension of the utilized antenna is D = 51.4 mm, and the wavelength of the interested frequency range covers 3-10 cm. According to (2.1), and performing fine tuning simulations using Ansys High Frequency Structure Simulator (HFSS), the distance between the two antennas is chosen, $2d$ = 60 mm, in order to couple the two antennas in their Fresnel regions while the mutual coupling and the MUT have negligible effects on the return loss characteristics of the two antennas. In this setting, the simulated and measured group delay is extracted and shown in Fig. 2.10 (b). The slight differences between the

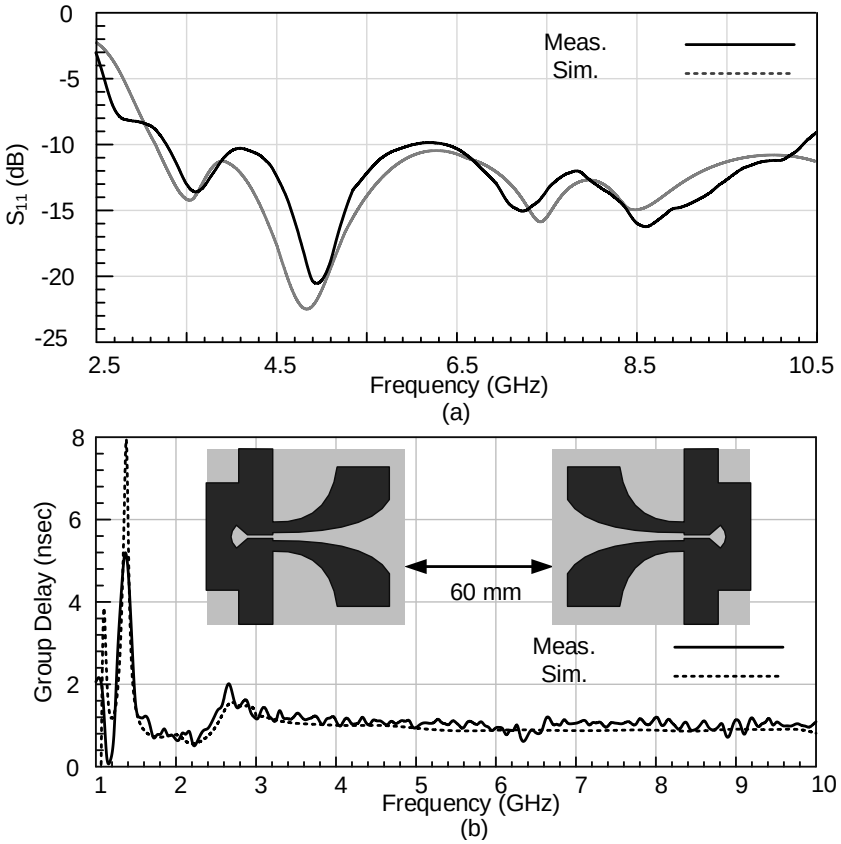

Figure 2.10: (a) Simulated and measured return loss characteristics of the utilized UWB Vivaldi antenna, and (b) simulated and measured group delay of the setup when the distance between the two antennas is $2d$ = 60 mm. Reprinted with permission from [1].

simulation and measurement is due to the tolerances between the SMA connector model in HFSS, and the actual SMA connector used in measurement. In order to better show that the two near-field coupled antennas remain matched to 50 Ω regardless of the MUT in between, the simulated S_{11} response is plotted in Fig. 2.11 when different MUTs are placed in middle. Debye-based relaxation models of MUTs are imported into HFSS in order to take into account the frequency dependence of the dielectric constants in full-wave simulations [23]. As can be seen, the antenna element shows return losses better than 10 dB over the entire bandwidth for all the materials with a broad range of dielectric constants ($2.45 < \epsilon' < 42$ for xylene at 10 GHz as the minimum and dmso at 3 GHz as the maximum, and $0.045 < \epsilon'' < 20$ for xylene at 3 GHz as the minimum and dmso at 8.5 GHz as the maximum).

Another important factor in the proposed contact-less setup is the cuvette used to place the

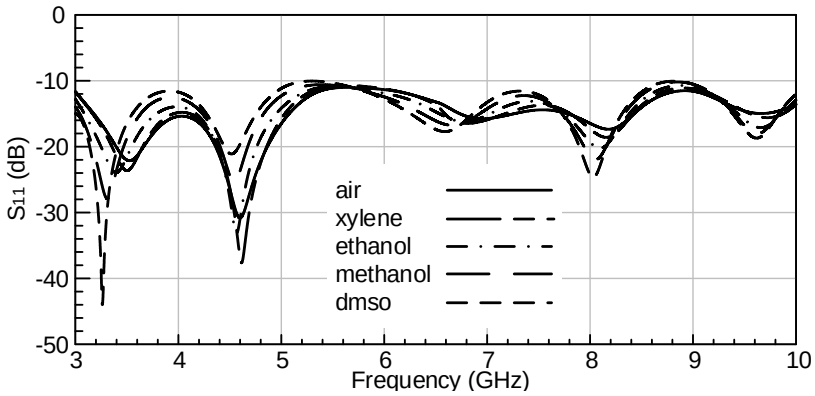

Figure 2.11: Simulated S11 of the setup when different MUTs are placed in between, and the distance between the two antennas is $2d$ = 60 mm. Reprinted with permission from [1].

liquid MUT in between the two antennas. Since the proposed setup is based on sensing in the Fresnel region in a controlled environment, the shape, dimensions, and the material of the cuvette also require to be designed and set for all the measurement trials. At the same time, the cuvette needs to be low-cost in order to make inexpensive repeating of the measurement for various MUTs feasible. In [26], a standard tube pipet (made from polypropylene with a diameter of 17 mm) is utilized as the liquid cuvette between the two antennas. Using this cuvette, roughly 15 mL of the sample is required. Moreover, this cuvette has a cylindrical shape, which is not optimized for having minimum diffraction from the edges of the cuvette due to discontinuity in the dielectric constant. However, the required volume of the sample can be reduced, and the accuracy of the sensor improves if the shape and dimensions of the cuvette are custom designed. In order to better show the importance of the cuvette shape, and dimensions, the E-field distribution is plotted in between the two antennas, and where the MUT is placed, and shown in Fig. 2.12 at different frequencies. As can be seen, the cuvette requires to cover the area where the E-field distribution is concentrated. Otherwise, considerable amount of energy will be diffracted from the edges of the MUT and cuvette, which reduces the accuracy of the sensor specially for MUTs with large dielectric constants, such as dmso (ϵ' = 42 at 3 GHz).

Fig. 2.13 shows the cuvette used in the proposed work. This cuvette is made of Quartz glass with a dielectric constant of 3.78 and a loss tangent of below 0.0004, which is roughly independent

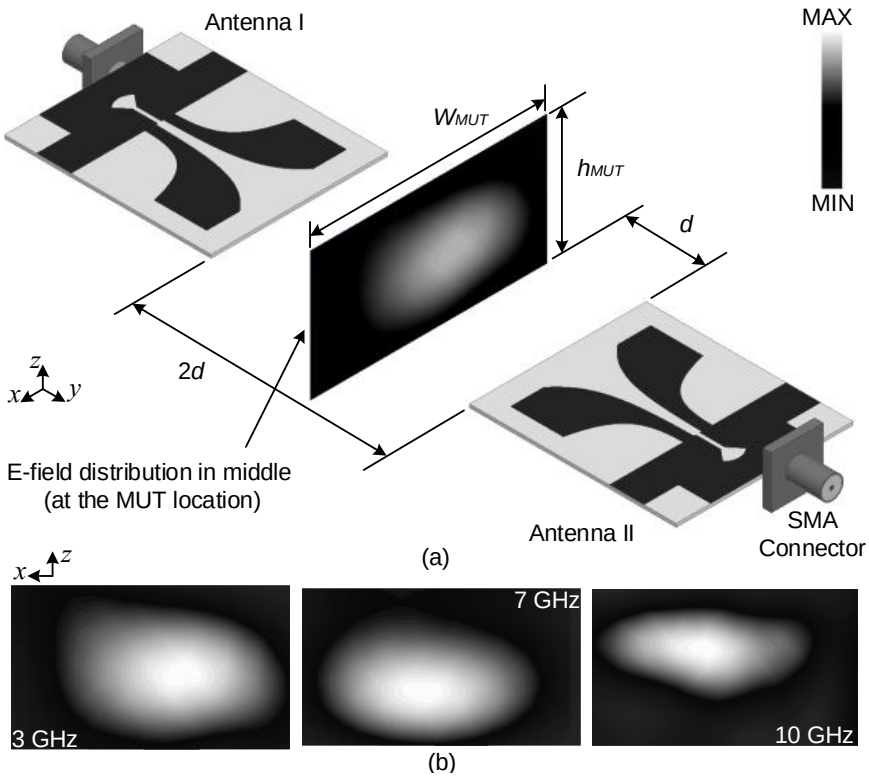

Figure 2.12: (a) The two near-field coupled antennas faced each other, and the E-field distribution is shown in middle and at the position of MUT at f = 3 GHz, and (b) the E-field distribution in a plane in between the two antennas where the MUT is located at different frequencies. The design values are: W_{MUT} = h_{MUT} = 51 mm, and d = 30 mm. Reprinted with permission from [1].

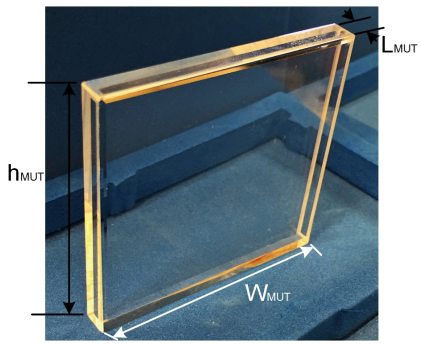

Figure 2.13: The cuvette used to place the liquid MUT in between the two antennas is made of Quartz glass with a volume of ∼5 mL. Reprinted with permission from [1].

of the frequency over the desired UWB range. The width and height of the cuvette are chosen to cover the main concentration of the E-field distribution in the middle plane, as was shown in Fig.

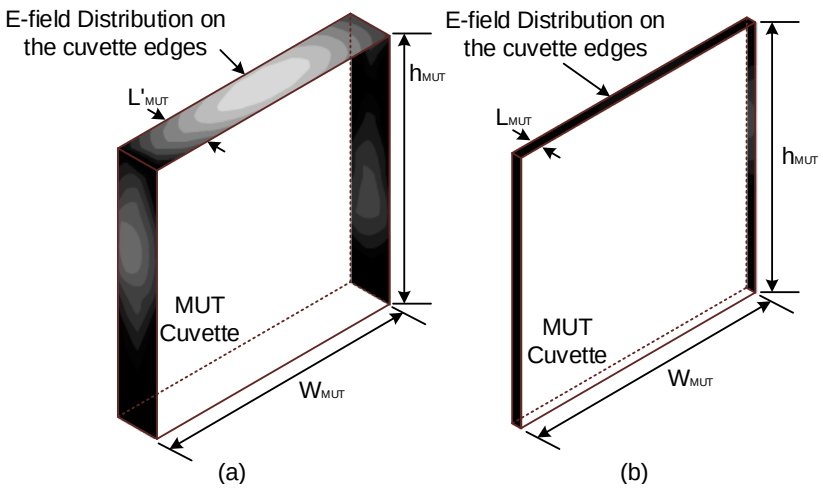

Figure 2.14: The E-field distribution on the edges of the MUT cuvette at 3 GHz, when (a) L'_{MUT} = 8.5 mm $>\lambda/10$ at 10 GHz, and (b) L_{MUT} = 2 mm $<\lambda/10$ at 10 GHz. Reprinted with permission from [1].

2.12(b) at different frequencies. As a result, W_{MUT}, and h_{MUT} are both chosen 51 mm. On the other hand, the length of the cuvette, L_{MUT}, needs to be lower than λ/10 at the upper limit (10 GHz) in order to avoid multiple reflection, and electromagnetic bouncing inside the MUT. A lower length for the cuvette also reduces the required volume of the MUT. Moreover, an L_{MUT}, smaller than λ/10 at 10 GHz results in negligible diffraction from the edges of the MUT, while having a larger L_{MUT} can result in significant electromagnetic diffraction from the edges. This is better shown in Fig. 2.14, where the E-field distribution is plotted on the edges of the cuvette at 3 GHz for two different values of L_{MUT}. As can be seen, when the length is as large as 8.5 mm, which is $\sim 0.28\lambda$ at 10 GHz, there are E-field maximums on each edge of the cuvette, while reducing the length to 2 mm ($\sim 0.06\lambda$ at 10 GHz) would result in negligible E-field concentration on the edges. As a result, the length of the cuvette, L_{MUT}, is chosen to be 2 mm $<\lambda/10$ at 10 GHz, in order to (1) reduce the required volume of the sample liquid MUT, (2) avoid Electromagnetic bouncing and multiple reflection issues, and (3) significantly reduce the diffraction from the edges of the cuvette. In this case, the required volume is $\sim$ 5 mL, which is $\sim$ 67% less than the cylindrical tube used in [26].

2.1.2.2 Pulse Generation

The step recovery diode (SRD) has various useful applications such as wave-shaping, harmonic generation, division, switching, sampling, and up-conversion [27]. In this section, the development of a picosecond pulse generator for UWB application is presented.

Most of low-power picosecond pulse generators use SRDs for generation of Gaussian or monocycle pulses [28]. SRD stores charge when it is forward biased, but when the biasing changes from forward to reverse bias state, unlike a normal diode, the SRD will not immediately turn off. Instead, it continues to have a low impedance until its stored charge is depleted in a time duration of τ_R. τ_R is the effective life time of minority carriers that have been injected across the junction during forward bias condition. After this time, the SRD impedance will suddenly increase to its normal high reverse impedance in a very short transition time, τ_t, essentially stopping the reverse current of SRD. This short transition is applicable in generating small duration pulses.

Fig. 2.15 shows the circuit schematic of the pulse generator. This pulse generator is composed of an SRD, a short-circuited shunt stub with length of L_A, a series Schottky diode, and an attenuator, R_S, added externally after fabrication. Lack of any biasing network makes this design simple and power efficient, and it eliminates DC blocking capacitors. The attenuator R_S is used to improve input impedance matching. However, because SRD impedance is voltage- and frequency-dependent [29], the signal reflection between SRD and Schottky diode is unavoidable, although it can be reduced by choosing the proper length, L_A. An external 5 Vp-p square-wave input with 5 ns rise time, turns the SRD ON and OFF periodically. The rise time of the clock should be less than minority carrier lifetime, τ_R, in order to obtain maximum achievable pulse amplitude [28]. In this design, an SRD is selected for τ_t = 50 ps and τ_R = 20 ns. Before the SRD turns OFF, an abrupt transition in its output voltage occurs which is used in generating the desired sharp pulse. The step-like output of SRD propagates through the main line as well as the stub. The wave in the stub is inverted, and it returns to the main line with a specific delay proportional to L_A. The delayed inverted signal is combined with the incident wave at the output of SRD and forms a sharp pulse. The shape and duration of the resulted signal is related to L_A, which determines the propa-

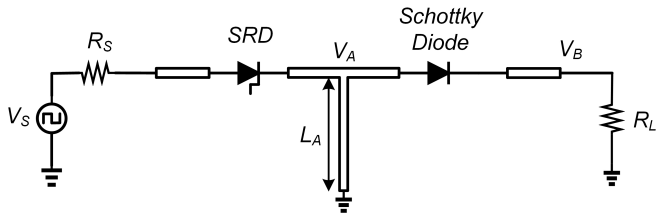

Figure 2.15: Schematic of Gaussian pulse generator. Reprinted with permission from [1].

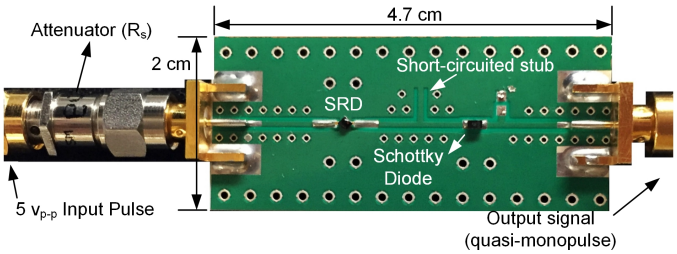

Figure 2.16: Photograph of pulse generator circuit. Reprinted with permission from [1].

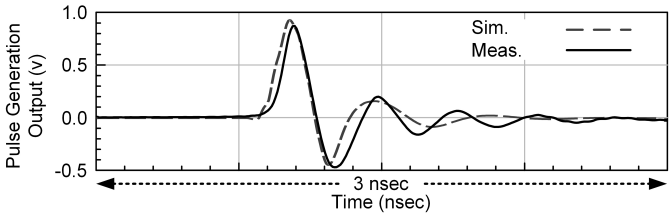

Figure 2.17: Simulated and measured output of pulse generator in TD. Reprinted with permission from [1].

gation delay of the signal through the stub. To reduce ringing, a series Schottky diode acting as a half-wave rectifier is used.

The pulse generator is realized using microstrip lines on Rogers 4350B substrate with $\epsilon_r = 3.66$, $\tan\delta = 0.0031$, and thickness of 0.338 mm. The SRD used is MMD835-H20 from Aeroflex and has a nominal lifetime of 20 ns and transition time of 50 psec. The Schottky diode is CDBU0130L from Micrometrics Inc with forward voltage equal to 0.35 V. The photograph of the fabricated circuit is shown in Fig. 2.16.

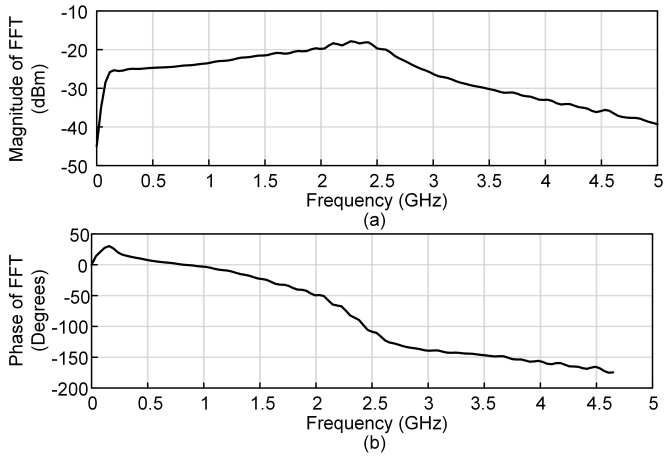

Figure 2.18: Measured output pulse in FD, (a) Magnitude, (b) Phase. Reprinted with permission from [1].

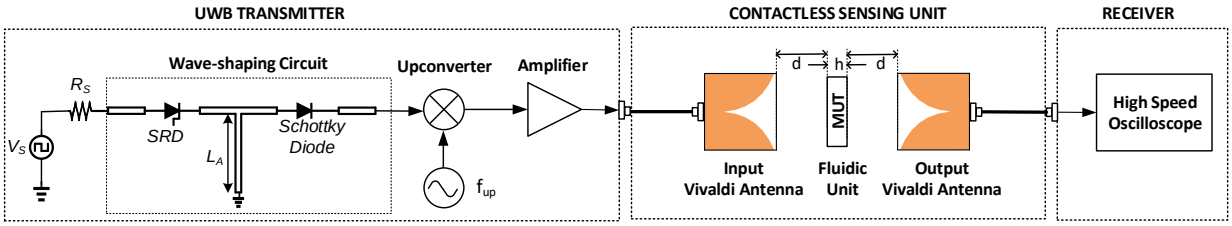

Figure 2.19: Contactless TD dielectric spectroscopy system. Reprinted with permission from [1].

The measured waveform and simulation results from ADS using SRD model introduced in [30], are shown in Fig. 2.17. This waveform can be called quasi-monocycle waveform; although a larger length of short-circuited stub can produce a Gaussian pulse, it was preferred to use this pulse for two reasons: (i) to achieve a shorter pulse duration and enhance the bandwidth compared with the Gaussian pulse; (ii) to have a larger magnitude at low frequencies, unlike the monocycle pulse. The FD representation of pulse is shown in Fig. 2.18. As can be seen, the 10-dB bandwidth of 3.5 GHz is obtained. Accordingly, this signal would be suitable to cover 7 GHz of UWB after up-conversion by a 6.5 GHz LO frequency.

2.1.2.3 System Design

The block diagram of the proposed contact-less UWB system for TD spectroscopy is shown in Fig. 2.19. This system is composed of a contact-less sensing unit, a UWB transmitter, and a high speed oscilloscope as a receiver. In the contact-less sensing unit, a removable fluidic cuvette carrying the MUT is located between two near-field coupled UWB Vivaldi antennas, as was discussed in section II. The transmitter includes a waveform generator, as presented in section III, a mixer and a local oscillator for up-conversion, and a UWB amplifier. The waveform generator produces a 3.5 GHz baseband quasi-monocycle signal. With a UWB up-converter, this baseband signal is up-converted by f_{up} = 6.5 GHz. As a result, a bandpass signal from 3 GHz to 10 GHz is generated. The UWB amplifier amplifies the signal and partially compensates for the mixer loss and sensing unit attenuation. Consequently, the sensing unit is excited by only a single UWB signal using a purely TD method. Ultimately, the output signal after sensor is measured and recorded by a high speed oscilloscope in TD. The phase and magnitude of the measured signal in FD are calculated with FFT method. On one hand, the mixer, amplifier and sensor alter the phase and magnitude of the signal as well, but on the other hand, in testing different MUTs in the system, all of these components except MUT show common effects on the signal in each test. To eliminate the common effects of other components, the system output signal with air as the MUT is captured as the reference output. Afterwards, the phase and magnitude of the reference output are subtracted from the phase and magnitude of the output when testing other MUTs. The calculated phase difference and magnitude difference are called $\Delta\phi$ and ΔMag respectively, and they only contain MUT information. The proposed spectroscopy system is designed to achieve the maximum SNR at the receiver input. The link design equation can be written as

$$\begin{aligned} SNR_{min} = P_{in,BB} - L_{mixer} + G_{amp.} \\ - L_{sensor,max} - P_{noise}, \end{aligned} \tag{2.2}$$

where SNR_{min} is the minimum SNR related to the test of MUT with the highest attenuation,

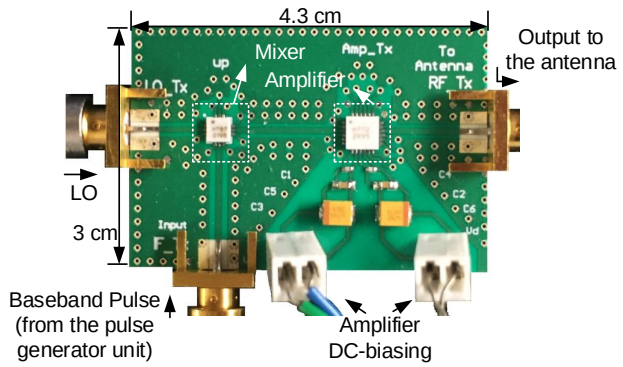

Figure 2.20: Photograph of fabricated UWB up-converter and amplifier. Reprinted with permission from [1].

$P_{in,BB}$ is the power of the baseband signal at the output of pulse generator which has the minimum of -31 dBm, L_{mixer} is conversion loss of mixer, $G_{amp.}$ is gain of amplifier, $L_{sensor,max}$ is the maximum loss of the sensing unit which is 26 dB for the MUT with the highest loss studied in this work (dmso), P_{noise} is the total noise power at the input of the receiver (oscilloscope) equal to -75 dBm for 7 GHz bandwidth (-174 + 10 $log(7 \times 10^9)$ = -75 dBm). Considering the available commercial off-the-shelf components for the amplifier and the mixer, the link budget is designed for L_{mixer} = 9 dB and $G_{amp.}$ = 16 dB. As a result, according to equation 2.2, the SNR_{min} is 25 dB. HMC787ALCB mixer and HMC772LC4 amplifier both from Analog Devices are utilized in the transmitter.

The up-converter and amplifier are fabricated in a separate board on Rogers 4350B substrate with ϵ_r = 3.66, $\tan\delta$ = 0.0031, and a thickness of 0.338 mm. The prototype of the whole transmitter is shown in Fig. 2.20. The measured output of transmitter excited by the baseband pulse generator is shown in Fig. 2.21. The signal phase and magnitude information from 3 GHz to 10 GHz is used in MUT characterization. Although the 10-dB bandwidth extends from 3.32 GHz to 9.26 GHz, the link design considerations allows for accurate measurement from 3- 3.32 GHz and 9.26- 10 GHz in the receiver, where the amplitude drops by a maximum of 10 dB.

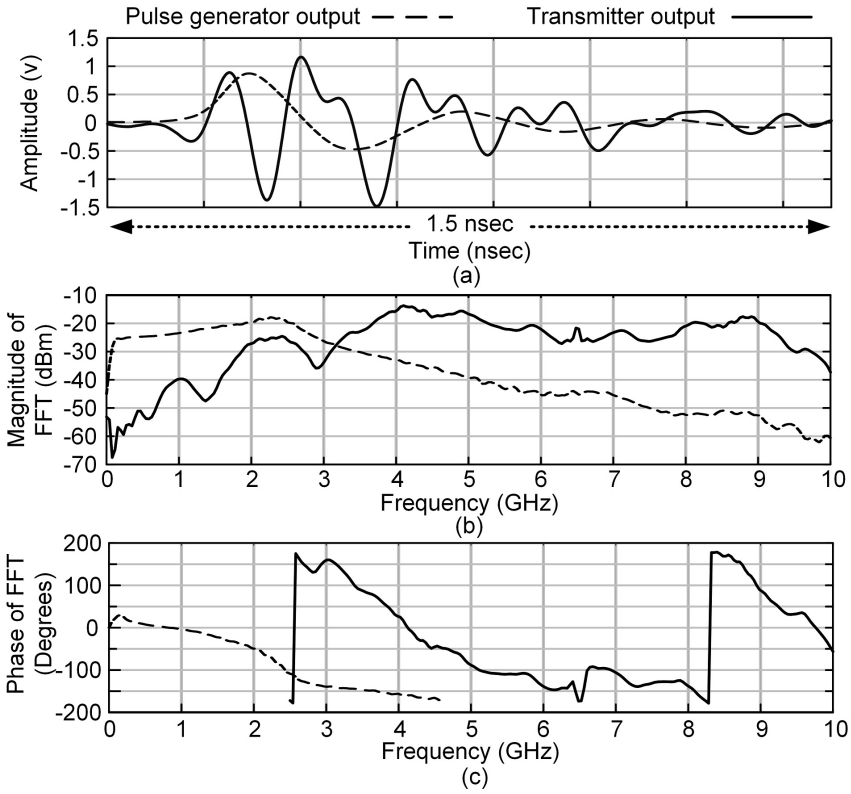

Figure 2.21: Measurement results of pulse generator and transmitter outputs at both baseband and RF, (a) TD signal, (b) Magnitude of FFT of the output signal, (c) Phase of FFT of the output signal. Reprinted with permission from [1].

2.1.2.4 System Implementation and Experimental Results

The fabricated setup is shown in Fig. 2.22. The time-domain data is captured for each MUT using DSA91304A infiniium oscilloscope as the receiver as shown in Fig. 2.23, and finally the fast Fourier transform of the measured data is extracted in MATLAB (Fig. 2.24). A calibration procedure is used to achieve a behavioral model of the system using seven calibration MUTs. The general form of curve-fitting equations for ϵ'–$\Delta\phi$ and ϵ''–ΔMag are given by (2.3) and (2.4), respectively:

$$\begin{aligned}\epsilon' = {} & P_{p1}(\Delta\phi)^4 + P_{p2}(\Delta\phi)^3 + P_{p3}(\Delta\phi)^2 \\ & + P_{p4}(\Delta\phi) + P_{p5},\end{aligned} \tag{2.3}$$

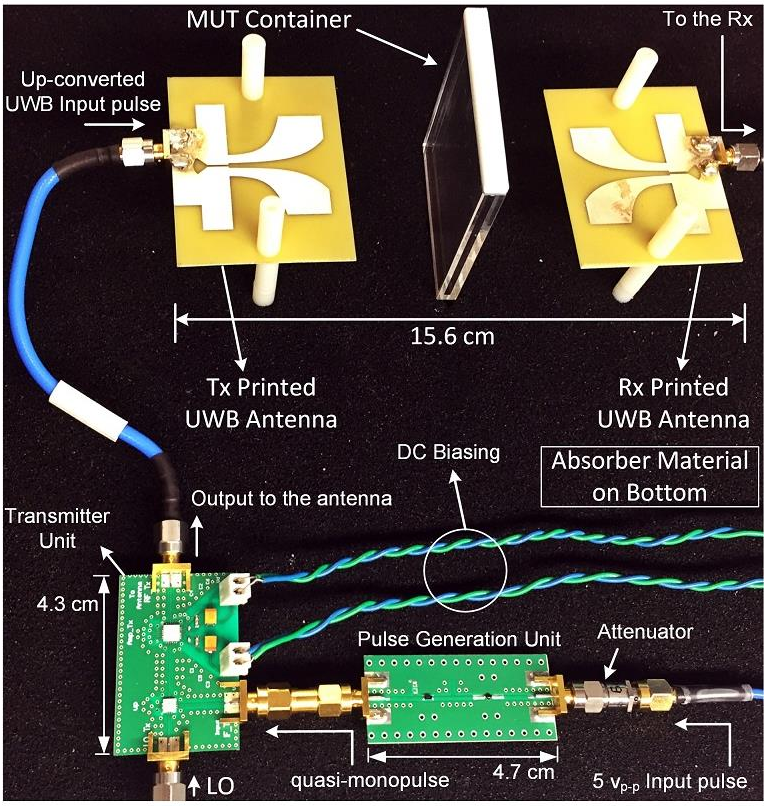

Figure 2.22: Fabricated setup of the proposed contactless UWB spectroscopy system. Reprinted with permission from [1].

$$\begin{aligned}\epsilon'' = {} & P_{m1}(\Delta Mag)^5 + P_{m2}(\Delta Mag)^4 + P_{m3}(\Delta Mag)^3 \\ & + P_{m4}(\Delta Mag)^2 + P_{m5}(\Delta Mag) + P_{m6}.\end{aligned} \tag{2.4}$$

The curve-fitting coefficients in each polynomial are shown versus frequency in Fig. 2.25. As can be seen, the polynomial coefficients are functions of frequency. From there, the ϵ' and ϵ'' characterization of three unknown MUTs are carried out as shown in Fig. 2.26. The system shows the worst-case mean-squared error (MSE) of 1.92% for ϵ' and 3.84% for ϵ'' characterization. Furthermore, binary mixture detection based on ϵ' accomplished with the MSE of 2.74% as shown

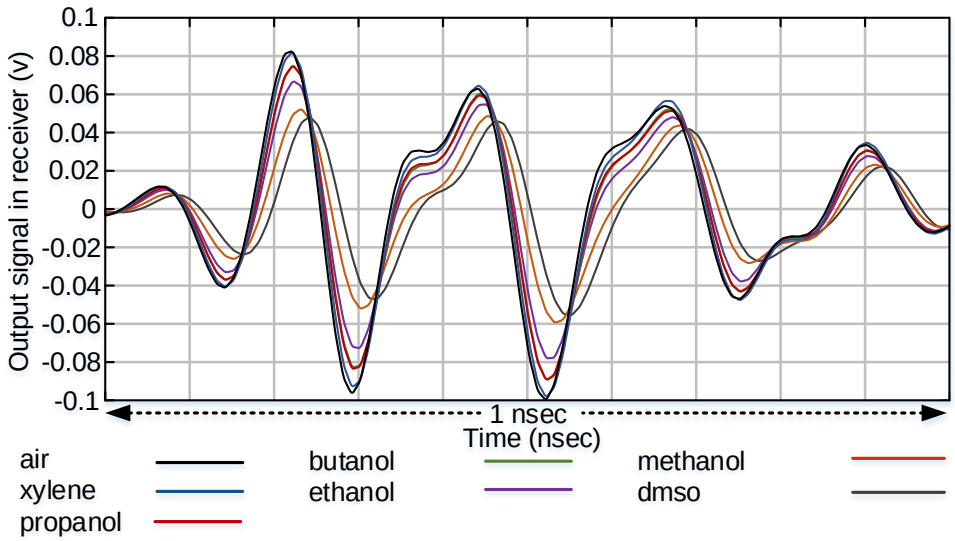

Figure 2.23: Measurement output signal in time-domain for different calibration MUTs. Reprinted with permission from [1].

in Fig. 2.27.

2.1.2.5 Discussion

Table 2.1 compares the proposed contact-less TD dielectric spectroscopy system with the previously reported works in literature. As can be seen, although the operation frequency of the proposed setup is lower than [15, 17, 18], the setup and MUT sizes are significantly smaller. This allows the proposed method to be utilized for low-volume liquid sensing applications, while all other works have been tested with bulky solid materials. Moreover, [16] provides a tunable UWB sensor with significantly bulky and large antennas for ground penetrating (sub-surface) radar applications. This work utilizes a combination of FD and TD to cover different bands in the UWB range. However, the proposed system in this work provides complete UWB coverage in one measurement trial.

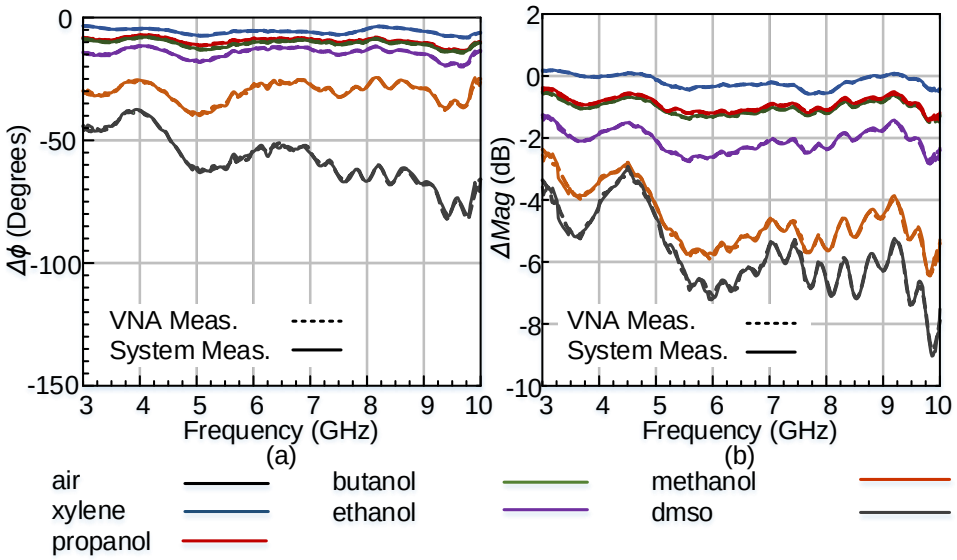

Figure 2.24: Measurement results of the proposed system and VNA, (a) $\Delta\phi$ and (b) ΔMag. Reprinted with permission from [1].

2.1.2.6 Conclusion

A compact contact-less UWB microwave system for TD liquid material characterization is proposed in this paper. First, an in-depth study of the near-field contact-less sensing of liquid MUTs is discussed. The MUT, in a custom-designed cuvette, is placed in between two Vivaldi antennas that are coupled to each other in their Fresnel region. The design and implementation of the pulse generator unit is presented afterwards. Then, the transmitter unit including a direct up-conversion architecture is proposed to provide an excitation pulse of 3- 10 GHz 10-dB bandwidth to pass through the sensing unit. The pulse is ultimately received using DSA91304A infiniium oscilloscope, and the effect of each MUT is captured by extracting the FFT of the received pulses for each MUT in MATLAB. From the results, a calibration procedure is evaluated to achieve a behavioral model of the system according to seven known calibration MUTs. Thereafter, three unknown MUTs are characterized successfully with the worst-case MSE of 1.92% in ϵ' and 3.84% in ϵ'' over the entire UWB range. Finally, the binary mixtures of ethanol and methanol are detected

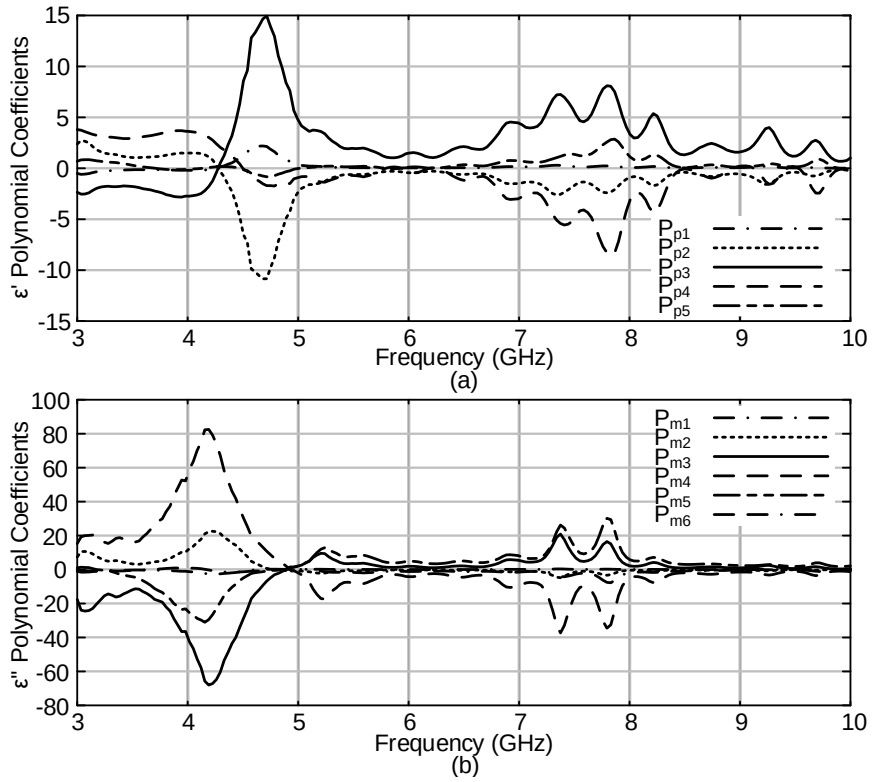

Figure 2.25: Coefficients at curve-fitting of (a) ϵ'–$\Delta\phi$ with 4th order polynomial and (b) ϵ''–ΔMag with 5th order polynomial versus frequency. Reprinted with permission from [1].

according to ϵ' with the total MSE of 2.47%.

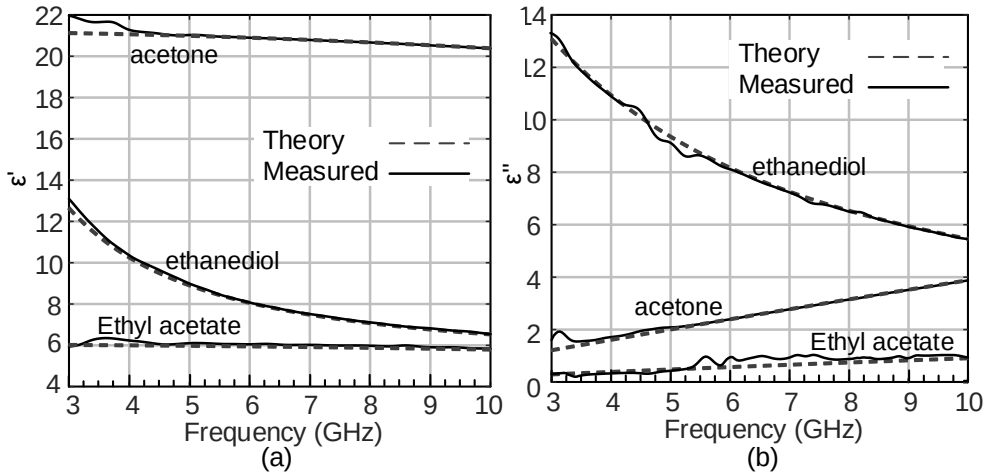

Figure 2.26: Comparison of measured and theoretical ϵ' and ϵ'' for three unknown MUTs. Reprinted with permission from [1].

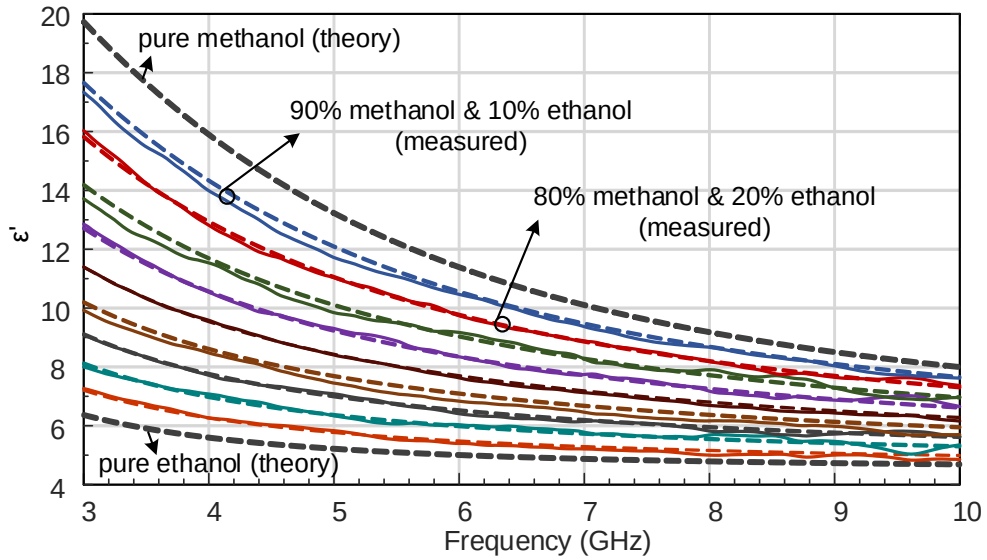

Figure 2.27: Measurement and theoretical ϵ' of ethanol and methanol mixtures in UWB. The mixing ratio K=0,10,...,90,100% is increased from top to bottom. Reprinted with permission from [1].

2.2 Time-Domain Dielectric Spectroscopy Using Contact-Based UWB System

Time-Domain dielectric spectroscopy is a fast, simultaneous, and highly accurate measurement technique for unique detection and characterization of MUTs over broad frequency ranges. Therefore, it has been widely employed to identify MUTs in medical, biological, and agricultural applications.

Existing contact-based TDS systems in microwave range typically use bulky open-ended coaxial probes as their sensors. In these systems, a large volume of MUT is required to provide fairly accurate measurements. Errors may arise because of significant density variations and creation of air bubbles at the end of probes. Moreover, due to the propagation of higher order modes and radiation effects at high frequencies, there are approximations associated with the electrical model of the probe. To the best of the author's knowledge, there has not been any miniaturized contact-based TDS system using small volume of MUTs compared with reported miniaturized frequency-domain spectroscopy systems.

The implementation of a contact-based dielectric spectroscopy system and its extended version are presented in this section.

2.2.1 Contacted-Based system for phase measurements

In this section, a miniaturized time-domain dielectric spectroscopy system in 3- 10 GHz range is presented. The proposed system consists of a UWB transmitter, a sensor, and a high speed oscilloscope as receiver. In the UWB transmitter, a wave-shaping circuit with an SRD and a short-circuited stub generates the baseband UWB signal, a mixer and an amplifier upconvert and amplify the baseband UWB signal and apply it to the sensor in 3- 10 GHz range. The sensor is constructed using a periodic structure of 8 downsized cells while the MUT is inside a container located on top of the sensor.

2.2.1.1 System Design and Implementation

In this section, the design and implementation of contact-based sensor and a brief theory of UWB pulse generation are presented.

2.2.1.1.1 Contact-Based Sensor

The proposed miniaturized sensor is shown in Fig. 2.28 (a). In this sensor, the MUT is inside a container placed on top of a periodic structure consisting of 8 cells. When the sensor is exposed to the MUT, the electric field inside MUT will change with respect to the complex permittivity of the MUT, $\epsilon^* = \epsilon' - j\epsilon''$, and it will cause the change in phase and magnitude of the signal passing through the sensor. Since the phase and magnitude of the signals are measurable quantities, the complex permittivity of MUTs can be inferred from the phase and magnitude measurements at the sensor output. As shown in Fig. 2.28 (b) and 2.28 (c), each cell is composed of an open circuited microstrip line between two meander inductors. Each cell causes the same amount of phase shift on the incoming signal, hence the entire structure will generate a total phase shift 8 times larger than the phase shift from a single cell increasing the sensitivity. The equivalent circuit of the cell is shown in Fig. 2.28 (d), where L is the inductance of meander line, C_s is the fringing capacitance between meander lines, and C_f is the fringing capacitance at the end of open stub. By adding the MUT on top of the entire cell (meander inductors and microstrip line), the effective $Z_{sh} = Z_{sh0} + \Delta Z_{sh}(\epsilon', \epsilon'')$ and also $C_s = C_{s0} + \Delta C_s(\epsilon', \epsilon'')$ will change resulting in phase and magnitude variation of the unit cell and as a result the entire sensor. Covering the entire cell with MUT results in significant phase variation, as will be shown later. The liquid container has a bottom wall avoiding direct contact of MUT with the sensor. This results in wider bandwidth for sensor (the values of L and Z_{sh} can be properly adjusted) and also preventing the sensor metallization from degradation[31].

The sensor is optimized using Sonnet EM simulator for MUTs air, butanol, ethanol, methanol, dmso, and water from 3 to 10 GHz. Fig. 2.29 (a) shows that the sensor exhibits matching better than -9 dB for all of the MUTs in UWB frequency range. According to Fig. 2.29(b), the phase difference between MUT and air ($\Delta\phi$) for different MUTs is at least 13 degrees at the frequency of 3 GHz. The 13 degrees phase shift results from the cascade of 8 cells. The smaller number of cells will not generate enough $\Delta\phi$ for accurate measurement especially at lower frequencies while the

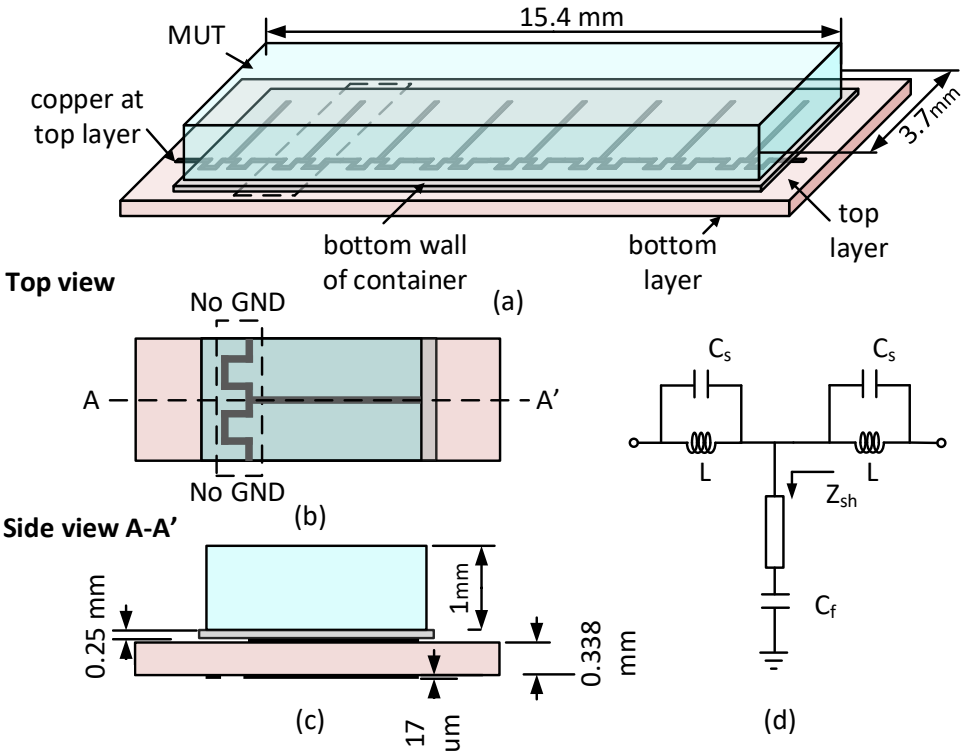

Figure 2.28: The miniaturized sensor with a total area of 3.7 $\times$ 15.4 mm^2 (a) 3-D view of the entire sensor consisting of 8 cells, (b) Top view of a single cell, (c) A-A' cross-sectional side view of a single cell, (d) simplified equivalent circuit. The drawings are not to scale. Reprinted with permission from [4].

larger number of cells will increase the area of sensor. The magnitude difference (ΔMag) between each MUT and air is not significant for this sensor ($\Delta Mag < 0.9$ dB). As can be seen from 2.29(b), the monotonic behavior of $\Delta\phi$ follows the increase of ϵ' of applied MUTs [32]. Therefore, $\Delta\phi$ is a strong function of ϵ'.

2.2.1.1.2 UWB Pulse Generator

Step Recovery Diode (SRD) has been widely used in pico-second pulse generators. There are two important time durations in the reverse biased operation of the SRD: charge depletion time τ_R and transition time τ_t. During the forward biased state, the SRD stores charge due to the minority carriers and its impedance is small. When the SRD excitation switches from forward to reverse

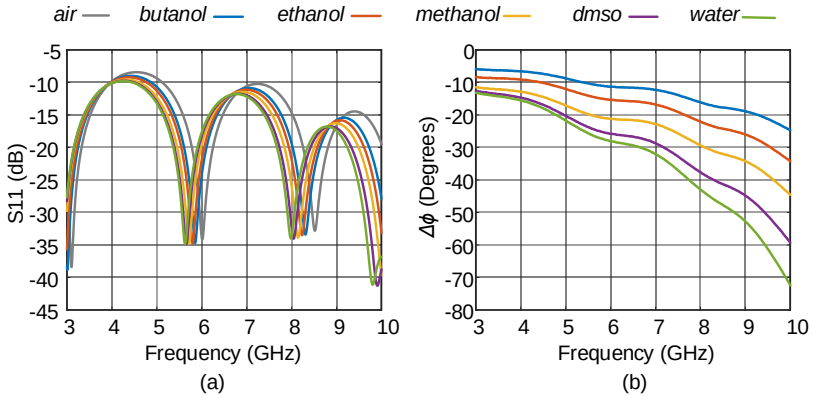

Figure 2.29: Simulation results: (a) S11 for six MUTs, and (b) $\Delta\phi$.Reprinted with permission from [4].

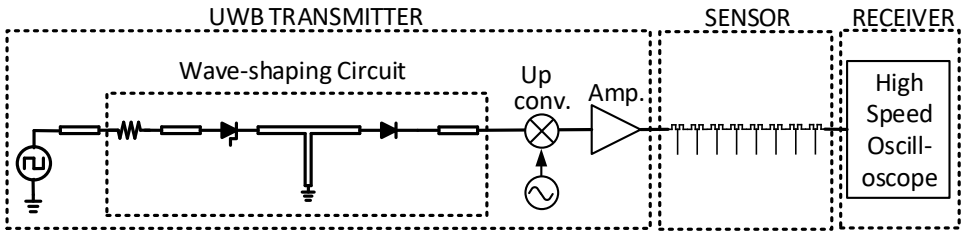

Figure 2.30: The proposed TD miniaturized spectroscopy system diagram.Reprinted with permission from [4].

biased, it does not turn off immediately. Instead, it releases its charge during τ_R. τ_R equals to the minority carrier lifetime. After the depletion of the minority carriers, the SRD stops the reverse current conduction and its impedance will abruptly increase in the very short transition time of τ_t. This short transition is employed in pulse generation circuits.

2.2.1.2 Spectroscopy System Architecture

Fig. 2.30 shows the block diagram of the proposed contact-based miniaturized UWB system for TD spectroscopy. This system is composed of a UWB transmitter, a sensor, and a high speed oscilloscope receiver. As discussed in Section 2.2.1.1.1, the sensor consists of 8 sensing cells with the MUT above this structure. The transmitter consists of a pulse generator (Section 2.2.1.1.2),

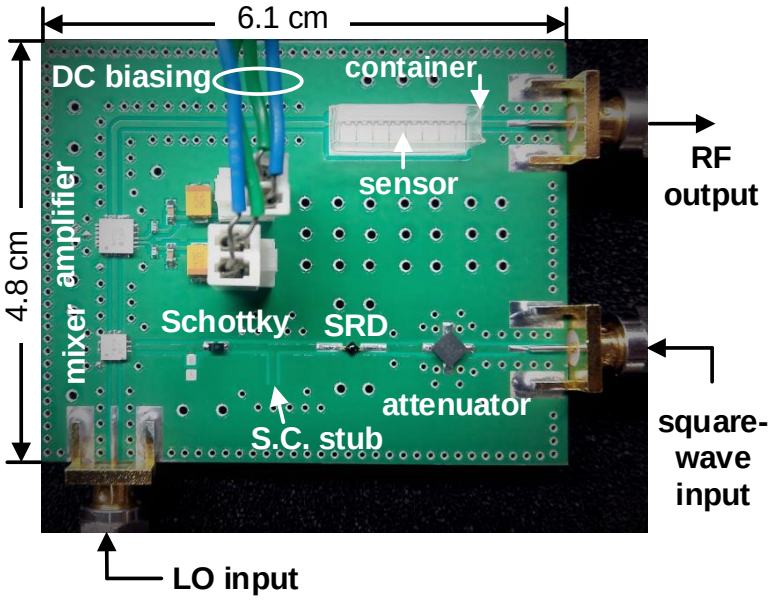

Figure 2.31: Photograph of the fabricated UWB spectroscopy system. Reprinted with permission from [4].

an upconverter containing a passive UWB mixer and a local oscillator (LO), and a UWB amplifier. The 3.5 GHz baseband pulse generated from the wave-shaping circuit is upconverted by 6.5 GHz LO to achieve a 3-10 GHz passband signal suitable for UWB frequency range. Although the signal is attenuated by the passive mixer, it is amplified with the amplifier and then passed through the sensor. Finally, the output of the sensor is captured by high speed oscilloscope. The phase information of the captured signal in frequency-domain is calculated by the FFT operation in MATLAB.

2.2.1.3 Fabrication and Measurements

The fabricated contact-based UWB spectroscopy system is shown in Fig. 2.31. RO4003B with ϵ' = 3.66 and $tan\delta$ = 0.0031 and the thickness of 0.338 mm is used as the substrate. The area of the miniaturized sensor is 3.7 $\times$ 15.4 = 51.8 mm^2, and the container is custom-made with vaccume forming process using polyethylene teraphalate (PET) with ϵ' = 2.5 and the thickness of 0.25 mm. The pulse generator consists of MMD835-H20 SRD (τ_R = 20 ns and τ_t = 50 ps), the microstrip

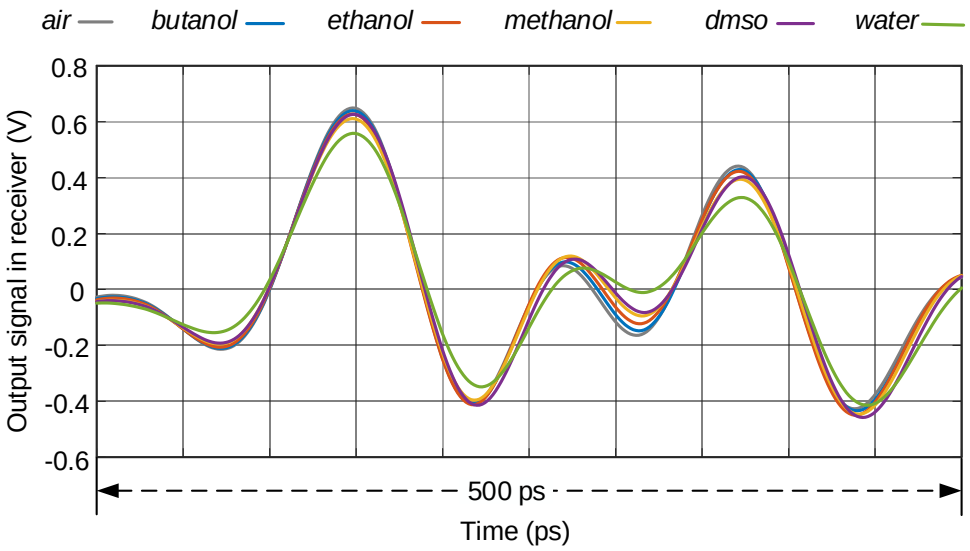

Figure 2.32: Measured output of the spectroscopy system in time-domain. Reprinted with permission from [4].

short circuited stub with $L_A = 4.5\ mm$, CDBU0130L Schottky diode, and GAT-6+ 6 dB attenuator. HMC787A mixer upconverts the baseband pulse using an external LO provided by E8267D PSG Vector Signal Generator, and it is amplified by HMC772LC4 amplifier. The input of the system is a 5 Vp-p square-wave with the frequency of 1 MHz and 5 ns rise time generated by 33250A function generator and the output of the system is captured by DSA91304A infiniium oscilloscope.

The output of the system in TD is shown in Fig. 2.32. The sequential delay with the order of air, butanol, ethanol, methanol, dmso and water is observed from Fig. 2.32. The FFT of the TD results are calculated in MATLAB and Fig. 2.33 shows $\Delta\phi$ in FD which is in the same order as simulation results in Fig. 2.33 (b). Fig. 2.34 shows the successful detection of acetone with 1.94% error as an unknown MUT. Its ϵ' is calculated with the polynomials describing the ϵ'-$\Delta\phi$ behavior of the system [1].

2.2.1.4 Conclusion

A miniaturized contact-based UWB spectroscopy system was proposed in this section. A small sensor exposed to an MUT is excited with a single UWB pulse in time domain. Then, the behavior

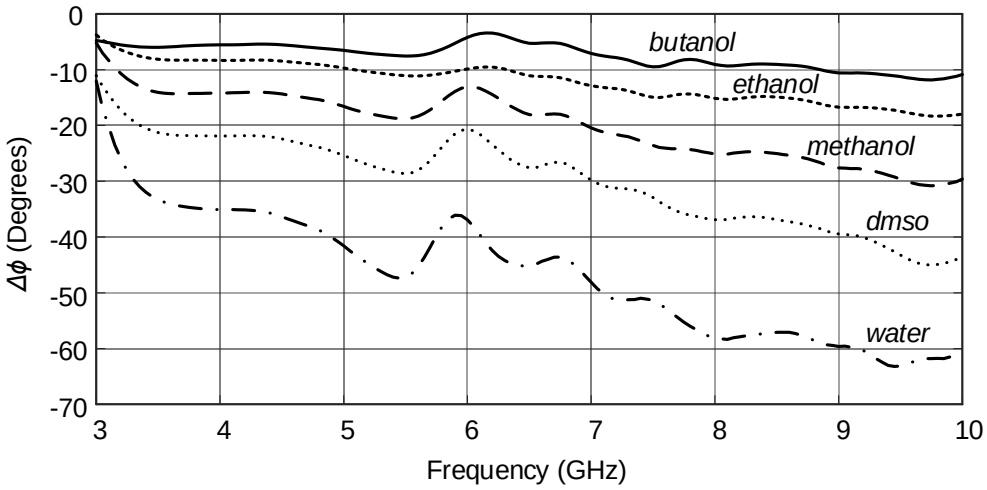

Figure 2.33: Phase differences in frequency-domain calculated from measured time-domain information. Reprinted with permission from [4].

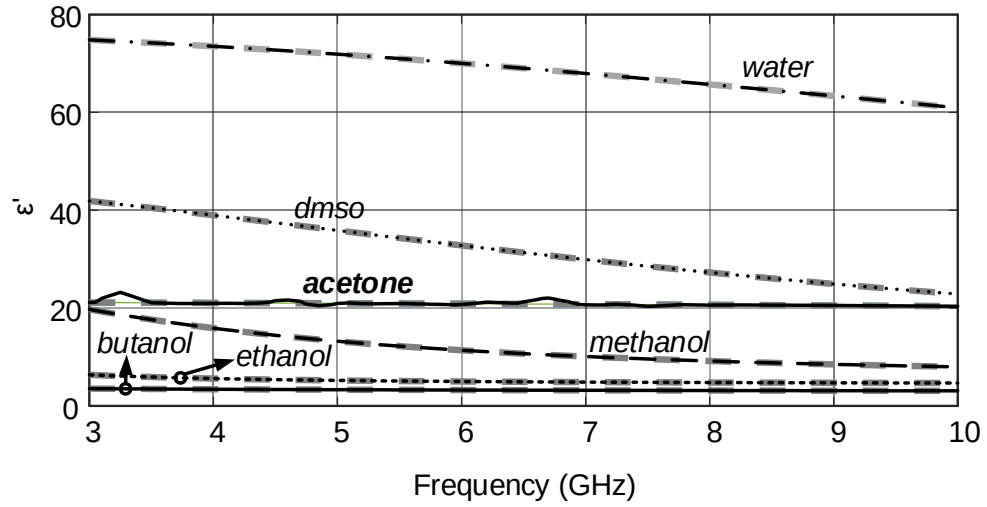

Figure 2.34: Calibration results: butanol, ethanol, methanol, dmso, and water are reference MUTs and acetone is an unknown MUT successfuly detected with polynomial behavioral model of the system. Reprinted with permission from [4].

of the system is modeled from the phase response of the system for five different reference MUTs. The ϵ' property of an unknown MUT was detected with an error less than 1.94%.

2.2.2 Contacted-Based system for phase and magnitude measurements

This section presents a miniaturized contact-based system for dielectric spectroscopy using time-domain technique in UWB frequency range. The system consists of a miniaturized UWB transmitter, a planar sensor having direct contact with a liquid MUT, and a high speed oscilloscope receiver.

In the transmitter, a baseband pulse with 3.5GHz bandwidth is generated from a square-wave input signal by employing a step recovery diode and a short-circuited stub. Then, the baseband pulse is upconverted by a UWB mixer with 6.5GHz LO frequency, creating a 3-to-10GHz passband pulse. After being amplified, the passband pulse excites the miniaturized sensor including two stages of microstrip open-circuited stub between meander inductors. This sensor has a small area, requires only 0.3μL of liquid MUT for accurate sensing, and responds to both ϵ' and ϵ'' properties. The sensor output is captured by the oscilloscope in TD and then converted to FD by the FFT operation.

The sensor and system design and implementation are presented in next subsections.

2.2.2.1 Contact-Based Sensor Design

2.2.2.1.1 Sensor Design Considerations Response of an MUT to an external electric field depends on the relative permittivity of the MUT [33]. Therefore, when an MUT is placed on top of a microstrip transmission line, the electric field over the signal trace will be affected by the MUT [34], which is measured as a variation in phase and magnitude of the voltage signal. Fig. 2.35(a) shows the layout of a microstrip open stub on RO4350B substrate with ϵ'=3.66, $tan\delta$=0.0031 and the thickness of 0.338mm, exposed to an MUT, which can be modeled as a microstrip line loaded by fringing capacitance C_f and resistance R_f (Fig. 2.35 (b)). C_f and R_f vary by changing the MUT. With different MUTs, such as air, ethanol, methanol, and water (distilled water with 0.0002S/m bulk conductivity), the impedance Z_{sh} seen at the beginning of the stub changes as plotted in Fig. 2.36 simulated in Sonnet and accurately modeled by the equivalent circuit. C_f and R_f are determined by equalizing Z_{sh} in Fig.2.35 (a) and Fig. 2.35 (b). Despite the sensor presented

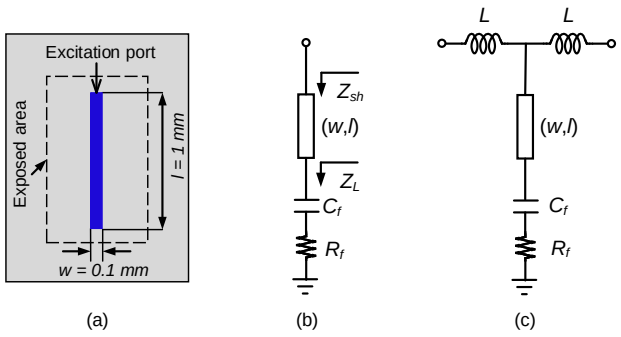

Figure 2.35: Microstrip open stub exposed to MUT (a) Layout, (b) Equivalent circuit model, (c) Sensing cell made of the microstrip shunt stub with two series inductors. Reprinted with permission from [5].

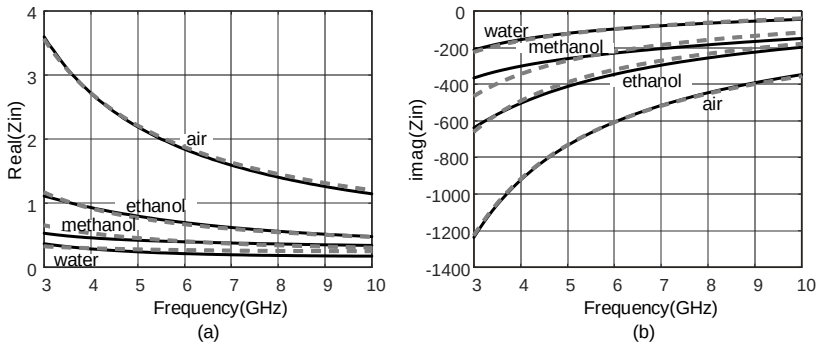

Figure 2.36: Impedance (Z_{sh}) of shunt stub (a) $Real[Z_{sh}]$, (b) $Imag[Z_{sh}]$. $Z_L = R_f + 1/j\omega C_f$, while $R_{f,air} = 41\Omega$, $C_{f,air}$=3fF, $R_{f,ethanol} = 0.75\Omega$, $C_{f,ethanol}$=40fF, $R_{f,methanol} = 0.4\Omega$, $C_{f,methanol}$=72fF, $R_{f,water} = 0.3\Omega$, $C_{f,water}$=188fF. (Sonnet: solid lines, Circuit model: dashed lines) Reprinted with permission from [5].

in [4], here the shunt stub is in direct contact with the MUT, hence, it senses variations in both ϵ' and ϵ'' of the MUT.

To detect the phase and magnitude variations of the open stub impedance (Z_{sh}) as phase and magnitude variations of a transmitted signal, and develop a wide band sensing structure, the microstrip stub is located between two series inductors L as shown in Fig. 2.35(c). The combination of shunt stub and inductors is considered as a sensing cell with two ports. The value of inductor in cell should be designed to provide enough phase and magnitude sensitivity for detecting different

MUTs and to meet matching condition. Having Z_{sh}, the Z-parameters of the single cell will be:

$$Z_{11} = Z_{22} = j\omega L + Z_{sh}, \tag{2.5}$$

$$Z_{12} = Z_{21} = Z_{sh}. \tag{2.6}$$

From these Z-parameters, the S-parameters, and then T-parameters of the single cell are calculated [35]. Because cascading multiple cells increases S_{21} phase variations, sensors with two and three cells are created by multiplication of the T-matrix. Then, T-parameters are converted back to S-parameters to study the effect of L on the behavior of two- and three-stage sensors. The sensitivity of the sensors are measured based on $\Delta\phi = \phi_{MUT} - \phi_{air}$ and $\Delta Mag = Mag_{MUT} - Mag_{air}$ parameters, where ϕ and Mag are phase and magnitude (in dB) of S_{21}, respectively, and subscripts indicate the name of MUT used in testing. To investigate the sensitivity of the sensor, minimum $\Delta\phi$ and $|\Delta Mag|$ values versus L over the frequency range of 3-10GHz are evaluated as shown in Fig. 2.37(a), (b). According to Fig. 2.37(a), larger value of L enhances phase sensitivity, but in terms of magnitude sensitivity, values of L larger than 1.4nH, will degrade $min|\Delta Mag|$ for water. This is due to the creation of nulls in S_{11} response in the frequency band of interest, which maximizes the transmission coefficient, S_{21}, showing small magnitude variations for different MUTs. Similar phenomenon happens for ethanol and methanol, but at frequencies larger than 10GHz. Another conclusion from Fig. 2.37 is that, increasing the number of stages from two to three will improve phase sensitivity, but it will further limit the range of L. Consequently, the value of L is decided to be in the range of 0.8nH to 1nH, and two cells are chosen which also suggests smaller space for sensor and lower volume of MUT. With two cells, $\Delta\phi_{ethanol} = 2.4°$, $\Delta\phi_{methanol} = 6.2°$, $\Delta\phi_{water} = 13°$, and $\Delta Mag_{ethanol} = 0.2dB$, $\Delta Mag_{methanol} = 0.5dB$, $\Delta Mag_{water} = 0.9dB$ are the minimum values to be measured. For a sensor with only one cell, the minimum $\Delta\phi$ and ΔMag values change in smaller ranges requiring a receiver with higher sensitivity for their detection.

Fig. 2.38 shows the designed inductor in Sonnet, its equivalent circuit model, and the effect

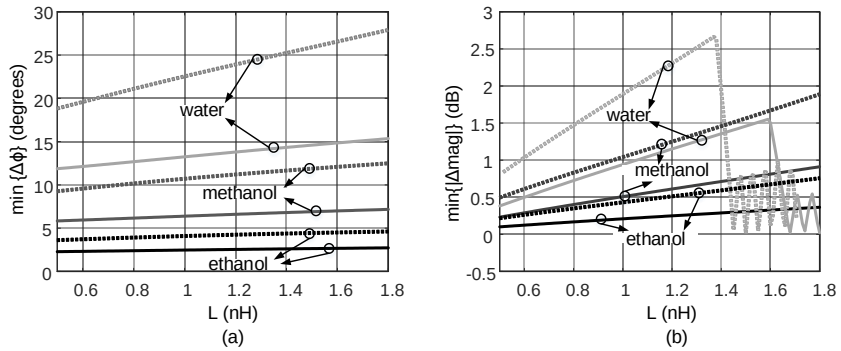

Figure 2.37: Effect of the inductance L value on minimum of (a) $\Delta\phi$, (b) ΔMag over UWB frequency range, considering 2 and 3 stages. (2 stages: solid lines, 3 stages: dotted lines) Reprinted with permission from [5].

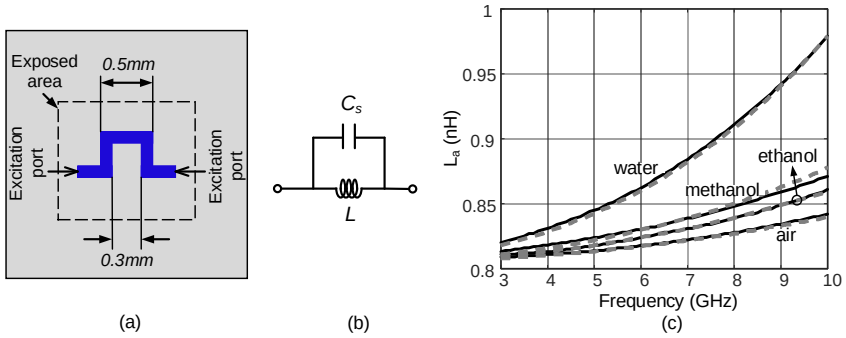

Figure 2.38: Design of inductor (a) Layout in Sonnet, (b) Equivalent circuit, (c) Simulated L_a compared with the equivalent circuit model. L=0.805nH, $C_{s,air}$=13fF, $C_{s,ethanol}$=20fF, $C_{s,methanol}$=26fF, $C_{s,water}$=57fF. (Sonnet: solid lines, Circuit model: dashed lines) Reprinted with permission from [5].

of MUT on the value of inductor. The resultant inductance L_a can be considered as a parallel combination of constant L and C_s while the value of C_s changes with MUT. L_a is a frequency dependent inductance which is related to L and C_s according to the following equation:

$$\begin{aligned} j\omega L_a &= (j\omega L)||(\frac{1}{j\omega C_s}), \\ L_a &= \frac{L}{1-\omega^2 L C_s}. \end{aligned} \tag{2.7}$$

which proves L_a increases with the frequency as shown in Fig. 2.38(c).

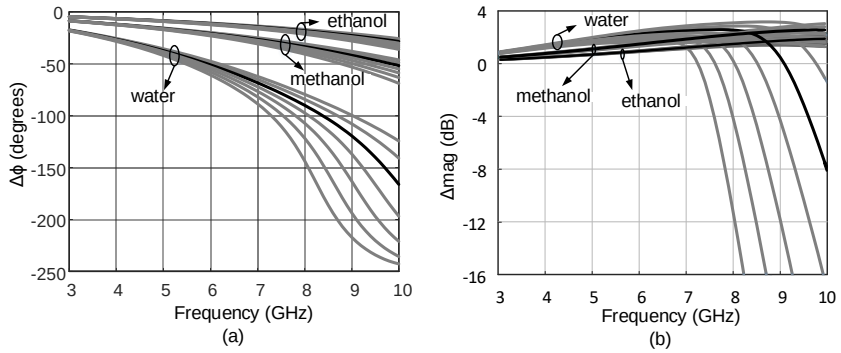

Figure 2.39: Effect of transmission line length l value on (a) $\Delta\phi$, (b) ΔMag, for different MUTs. l changes from 0.5mm to 1.7mm from top to bottom for each MUT (l=0.5,0.7,0.9,1.1,1.3,1.5,1.7mm). Black lines indicate case l=0.9mm. Reprinted with permission from [5].

The length of shunt stub, l, also affects the properties of the cell. Using L_a values designed in Sonnet and the R_f and C_f values found in Fig. 2.35 for each MUT , the effect of different lengths of shunt stub on sensitivity can be studied. Assuming width of transmission line w to be minimum 0.1mm on RO4350B substrate, the characteristic impedance Z_0 of transmission line will be 117Ω at 10GHz. With Z_L=R_f+$1/(j\omega C_f)$, Z_{sh} can be calculated as a function of l [35]:

$$Z_{sh} = Z_0 \frac{Z_L + jZ_0 tan(\beta l)}{Z_0 + jZ_L tan(\beta l)}, \tag{2.8}$$

where β =2π/λ is the phase constant, while $\lambda = \lambda_0 / \sqrt{\epsilon_{eff}}$ and ϵ_{eff} is calculated to be 2.461 at 10GHz. For a two-stage sensor, $\Delta\phi$ and ΔMag for different values of l=0.5,0.7,0.9,1.1,1.3,1.5,1.7mm are plotted in Fig. 2.39. Although larger value of l increases $\Delta\phi$, but large l limits the bandwidth and transmission of signal. As the result, a relatively small l=0.9mm is selected to achieve acceptable sensitivity. The final layout of the sensor with its complete electrical model are presented in Fig. 2.40.

$\Delta\phi$ and ΔMag are functions of both ϵ' and ϵ'', simultaneously. $\Delta\phi$ and ΔMag for two constant values of ϵ'=10 and 50 and two constant values of $tan\delta$=0.1 and 0.5 are plotted in Fig. 2.41. It can be seen from Fig. 2.41(a), that $\Delta\phi$ has a small deviation by sweeping $tan\delta$, and it is

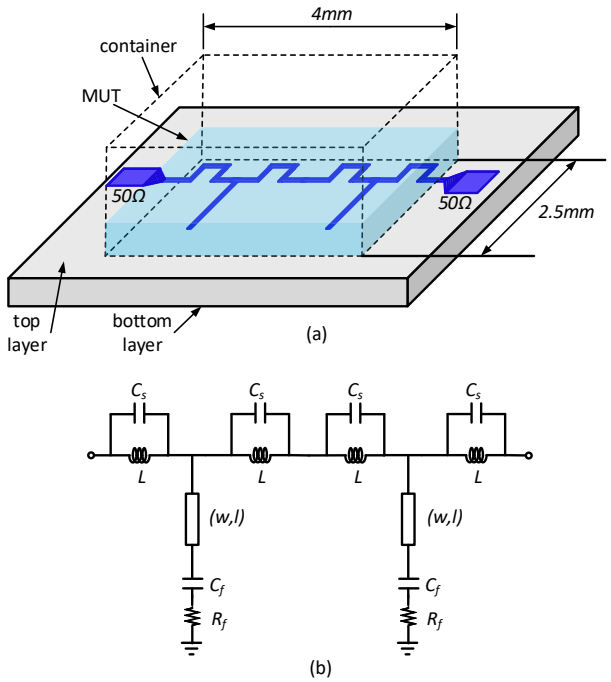

Figure 2.40: (a) 3D Layout of sensor with two stages, (b) Equivalent circuit model. Reprinted with permission from [5].

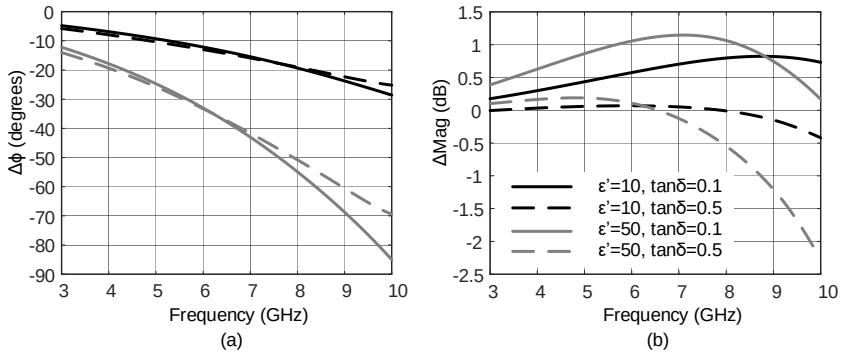

Figure 2.41: Effect of constant ϵ' and constant ϵ'' MUTs on (a) $\Delta\phi$, (b) ΔMag. Reprinted with permission from [5].

mainly a function of ϵ' at low frequencies. However, at high frequencies, the effect of $tan\delta$ on $\Delta\phi$ increases. As shown in Fig. 2.41(b), ΔMag largely varies by changing each one of ϵ' and ϵ''. Such dependencies are considered in calibration of ϵ' and ϵ''. The theoretical values of ϵ' and ϵ'' versus

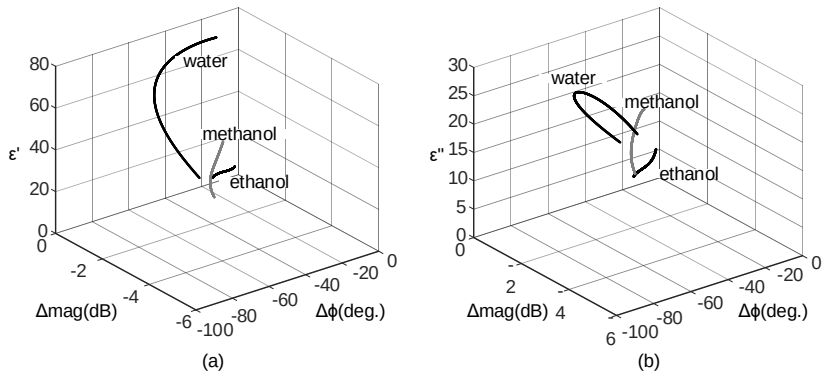

Figure 2.42: 3D response of the sensor (a) ϵ', (b) ϵ''. Reprinted with permission from [5].

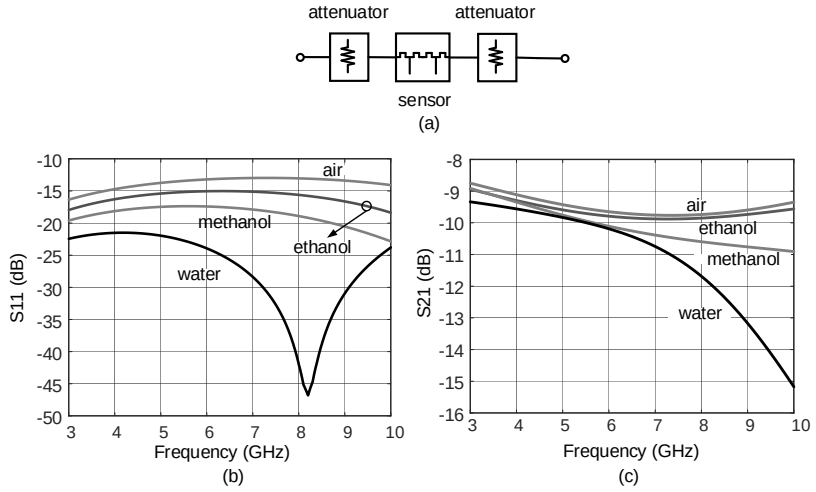

Figure 2.43: Impedance matching of the sensor to 50 Ω by adding attenuators (a) Schematic of the sensor with two attenuators, (b) $S11$, (c) $S21$ simulated. Reprinted with permission from [5].

simulated $\Delta\phi$ and ΔMag are shown in Fig. 2.42 for three different MUTs. The frequency variable has been excluded from Fig. 2.42, while all values change from 3-10GHz.

Although the sensor is sensitive to both ϵ' and ϵ'' of MUTs, the matching condition is not satisfied over 3-10GHz. To improve $S11$, constant attenuators are added to the input and output of sensing structure as shown in Fig. 2.43(a). According to Fig. 2.43(b), after adding two 4-dB attenuators at the input and output of the sensor, $S11$ for different MUTs is always less than -13 dB. Fig. 2.43(c) shows simulated S_{21} which cannot be larger than -8dB because of attenuators.

2.2.2.1.2 MUT Volume Effect on the Sensor Performance

The sensor is simulated for different MUT thicknesses, h_{MUT}, and the simulation results are presented in Fig. 2.44. Phase(S21) for ethanol, methanol, and water are shown for h_{MUT} = 0.03, 0.05, 0.1, 0.25, 0.50, 0.75, 1 mm. On the one hand, according to Fig. 2.44(a) and (b), by increasing h_{MUT} from 0.03mm to 0.5mm, the absolute value of phase(S21) will also increase. But, by further increasing h_{MUT} ($\geq$0.5mm), change in phase(S21) is negligible. That is because all electric fields are inside the MUT and further increase of MUT thickness does not affect the electromagnetic energy anymore and the sensor is saturated. On the other hand, according to Fig. 2.44(c) for water, if $h_{MUT}\geq$0.5mm, phase(S21) changes and more importantly, at higher frequencies the behavior of phase is not monotonic. The values of dB(S21) and dB(S11) for the case of water are also shown in Fig. 2.45. Because of the resonance appearing in dB(S21) response (Fig. 2.45(a)) for h_{MUT}=0.75mm and 1.00mm at 9.68GHz and 9.16GHz, respectively, dB(S11) of these cases reaches to its maximum at resonant frequencies (Fig. 2.45 (b)) and it violates the matching condition dB(S11)$<$-10dB. The violation of matching condition and creation of reflection waves result in destruction of phase response behavior at high frequencies in Fig. 2.44(c). Such behavior affects the accurate extraction of two quantities ϵ' and ϵ'' during calibration procedure. From the discussion above, h_{MUT} is chosen to be 0.2mm in all design steps and simulations. With h_{MUT}=0.2mm, the phase and magnitude responses are monotonic with respect to ϵ' and ϵ'' of the MUTs. In addition, the total volume of MUT is 4mm$\times$2.5mm$\times$0.2mm=2mm^3=2μL which is less than the case where h_{MUT} is 0.5mm (4mm$\times$2.5mm$\times$0.5mm=5mm^3=5μL).

By carrying the right volume of MUT (0.03mm$\leq h_{MUT}\leq$0.25mm) with a micropipette and using identical volumes for all of the MUTs, the sensor can successfully detect liquids with permittivities from 1 to 80. However, there might be still some error in phase measurement due to small variation of liquid height in the container. For a fixed liquid volume, it is better to use a microfluidic channel with inlet, outlet, and extremely thin top and bottom walls for more accurate control of liquid volume instead of an open container with a separate cap used in this work [36].

The sensor has been initially designed for MUTs with $1\leq\epsilon'\leq\epsilon'_{water}$. The simulation results of

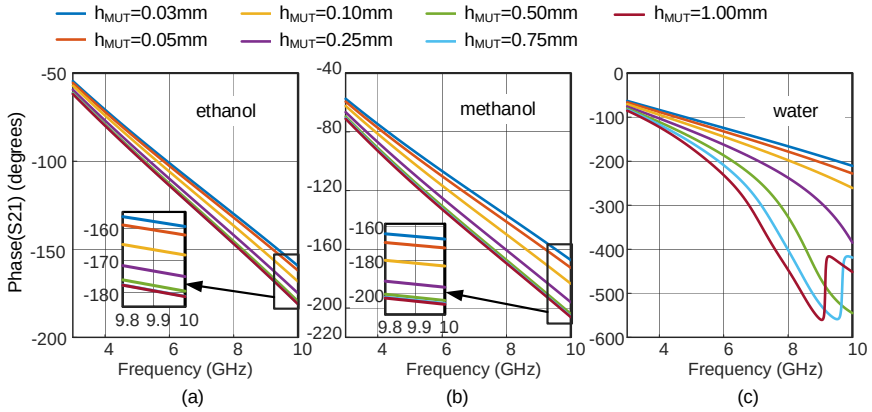

Figure 2.44: Sensor simulation results of Phase(S21) for different MUT thicknesses h_{MUT}, (a) ethanol, (b) methanol, (c) water. Reprinted with permission from [5].

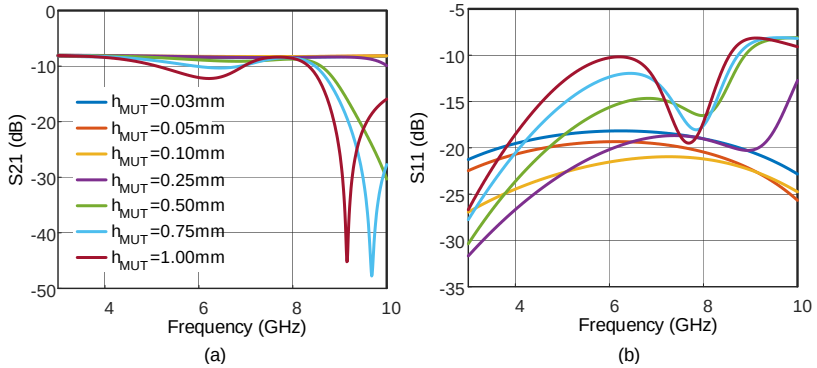

Figure 2.45: Sensor simulation results for different thicknesses of water, (a) S21(dB), (b) S11(dB). Reprinted with permission from [5].

the sensor for larger values of ϵ'=80,100,120,180,200 with three different values of $tan\delta$=0.1,0.5,0.9 are given in Fig. 2.46. According to Fig. 2.46, for larger values of ϵ' ($\epsilon' \geq 100$), the $\Delta\phi$ response does not remain monotonic at higher frequencies. In other words, a larger ϵ', does not necessarily provide a larger $\Delta\phi$. Such non-monotonic behavior causes the same phase response for different MUTs at some frequencies, and it makes the extraction of two quantities ϵ' and ϵ'' during calibration inaccurate. Therefore, the dynamic range of the system is limited to $\epsilon' \leq 100$. In addition, if $tan\delta$ is small, $tan\delta \sim 0.1$, and $\epsilon' \geq 100$, the magnitude sensitivity of sensor will be small at lower frequencies, and attenuation will be large ($\geq$40dB) at higher frequencies.

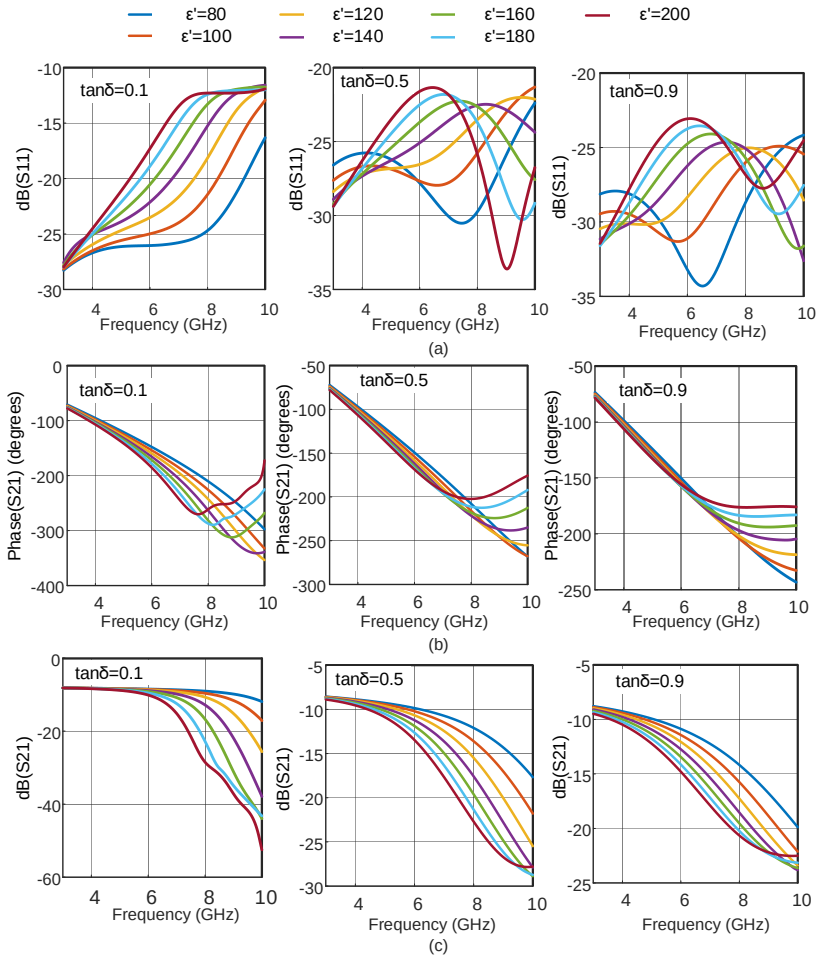

Figure 2.46: Simulation results of the proposed sensor for MUTs with large values of ϵ'=80,100,120,180,200 and three different values of $tan\delta$=0.1,0.5,0.9. (a) S11(dB), (b) Phase(S21), (c) S21(dB). Reprinted with permission from [5].

2.2.2.1.3 MUT Container Design

The MUT container surrounding the sensor is made of Polypropylene (PP) with ϵ'=2.2, a small dielectric constant to have negligible effect on the sensor excitation. PP exhibits many beneficial properties such as versatility, easy processing, resistance to corrosion, and low cost. PP has an excellent chemical resistance and most liquids don't react readily with it [37]. All of these make PP a good choice for containers of liquids. The simulations show that as long as $\epsilon'_{container} \leq 2.5$, the sensor excitation signal experiences less than 1 degree phase shift and less than only 0.003dB loss because of the presence of container on top of the excitation transmission line.

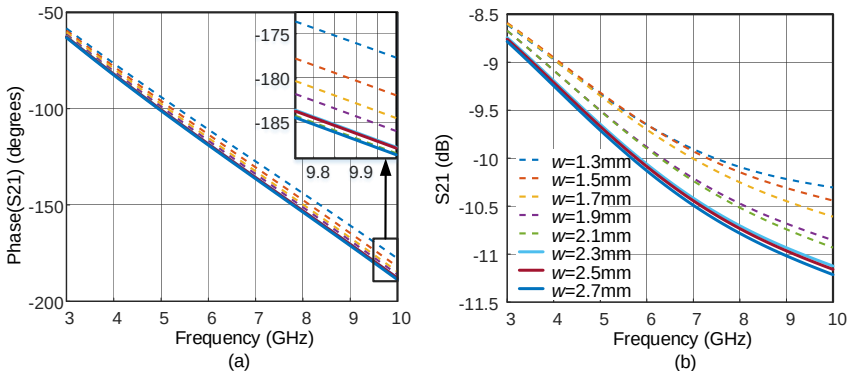

Figure 2.47: Effect of the width of container/MUT, w, on (a) phase and (b) magnitude of S21 for methanol. Reprinted with permission from [5].

The inner dimensions of PP container are 2.5mm$\times$4mm to cover the area of printed sensor, its height is 4mm to have enough room for adjusting different heights of MUT, and the thickness of walls is as low as 0.8mm mainly limited by the fabrication constraints. The width, w, of the container/MUT is 1.2mm larger than the width of the printed sensor (1.3mm) to ensure that the MUT is exposed to the electric fields in the sides of the container. To study the effect of w, the sensor was loaded with a typical MUT, methanol, and simulated for different values of w. The magnitude and phase of S21 are presented in Fig. 2.47. According to the simulation results in Fig. 2.47, the changes in phase of S21 is negligible for w $\geq$2.5mm, and the changes in magnitude of S21 is negligible for w $\geq$2.3mm. Therefore, w is considered to be 2.5mm. The length, l, of the container/MUT (4mm) is designed to be in the same length of the printed sensor (4mm). Since the sensor is connected to the transmission lines for excitation, longer container/MUT will affect the response of the transmission lines and excitation. In addition, it will increase the volume of MUT which is not desirable. The effect of l on response of the sensor is also studied while the sensor is loaded with methanol. The simulation results in Fig.2.48 show that both phase and magnitude of S21 slightly change by increasing l. Repeating the analysis with other MUTs results in similar choice of dimensions for container.

Instead of using current PP container, a cubic sample of solid with the same size of the container can be placed on top of sensor for sensing, as long as the permittivity of solid MUT is within the

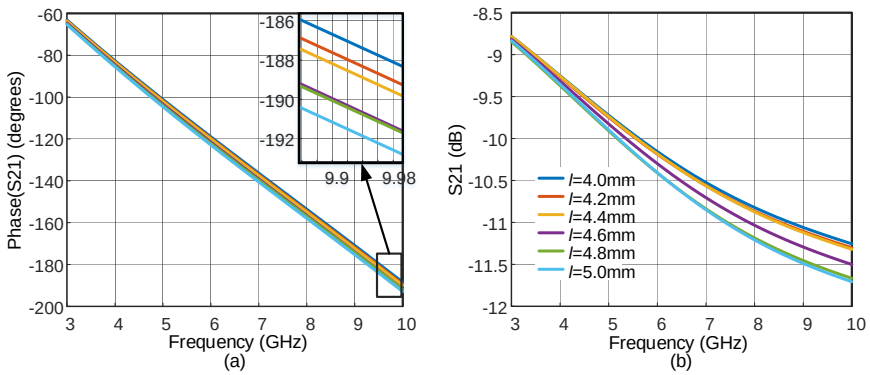

Figure 2.48: Effect of the length of container/MUT, l, on (a) phase and (b) magnitude of S21 for methanol. Reprinted with permission from [5].

dynamic range of the sensor (ϵ' <80). As an example, in [38], a modification of sample for accurate measurement of both liquids and solids by using contactless method in UWB range is presented. For liquid chemical sensing, a hollow plastic tube was used as the container, and for solids thickness sensing, dielectric slabs were employed. In both liquid and solid cases, the same quantity was measured (phase shift due to the presence of each MUT).

2.2.2.2 System Design

The miniaturized planar sensor is suitable to identify MUTs in 3-10GHz frequency range. In other words, the complex permittivity of an MUT can be calculated from $\Delta\phi$ and ΔMag responses of the sensor exposed to that MUT. However, obtaining $\Delta\phi$ and ΔMag information from a TD measurement requires excitation of the sensor by a short duration pulse which has 7GHz bandwidth. In addition, a high-speed receiver is necessary to capture the voltage response of the sensor in TD. The excitation pulse, as the input signal of the sensor, is generated through a UWB transmitter which consists of a baseband (BB) pulse generator, a UWB upconverter, and a UWB amplifier. Furthermore, a high-speed oscilloscope is used to acquire output of the sensor. Fig. 2.49 shows the overall block diagram of the proposed UWB TDS system.

The baseband pulse is generated by using an SRD as explain in 2.1.2.2. The output voltage of baseband pulse generator is upconverted by a UWB mixer which has an LO input at 6.5GHz. Consequently, a passband signal from 3-to-10GHz is generated at the output of the mixer. Then,

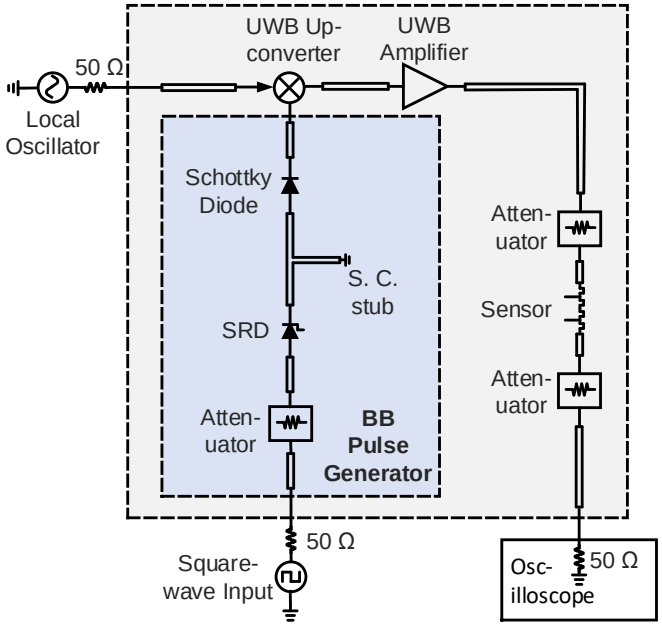

Figure 2.49: Block diagram of the proposed miniaturized UWB TDS system. Reprinted with permission from [5].

that signal is amplified by a UWB amplifier. Beside providing enough gain to establish a closed link, the amplifier blocks small reflections returning to the mixer. To avoid effect of reflections from sensor on the operation of amplifier itself, the matching between transmitter and sensor is designed to be better than -13dB for different. Consequently, the output of transmitter is approximately independent of the MUT.

The sensor output voltage varies with the MUT and acquired by oscilloscope. According to the sampling theorem, to capture the output voltage of sensor, an oscilloscope with sampling rate of 20GSps is required. In addition, the voltage level across 50Ω load of oscilloscope should be large enough to be distinguished from noise. To achieve an acceptable signal to noise ratio (SNR), the output voltage of sensor is 1024 times averaged by oscilloscope.

2.2.2.3 System Implementation and Measurements

Fig. 2.50 shows the photograph of the fabricated miniaturized UWB contact-based TDS system. The system fabricated using high frequency and low loss RO4350B substrate with ϵ'=3.66,

$tan\delta$=0.0031 and the thickness of 0.338mm. The total area of the fabricated board is 4.8cm$\times$6.1cm=29.28cm^2. The input of system is a 5Vpp square-wave signal with 1MHz repetition frequency and 5ns rise time generated by Agilent 33250A function generator for proper excitation of the pulse generator.

The baseband pulse generator consists of an MD835-H20 SRD with 50ps transient time, a 4.5mm microstrip short-circuited stub, a CDBU0130L Schottky diode, and a GAT-6+ attenuator. The output signal of baseband pulse generator is applied to an HMC787A mixer for upconversion, while the 6.5GHz LO frequency of mixer is generated by Agilent E8267D PSG Vector Signal Generator with the amplitude of +18dBm. The output signal of the mixer is amplified by an HMC772LC4 amplifier before exciting the sensor. The container was fabricated by Computer Numerical Control (CNC) machine. In addition, a 7mm$\times$5.5mm cap was fabricated using PP to cover the container. The container is fixed and glued with silicone rubber around the total sensing area. A 0.2-2μL micropipette with a 0.1-10μL pipette tip is used to insert 0.3μL MUT inside the container. Because a very small volume of liquid MUT is used for sensing, one should ensure that the MUT is distributed evenly at the bottom area of the container (2.5mm$\times$4mm). Therefore, the liquid MUT is dropped carefully on the whole bottom area inside the container. In case the first drop of MUT does not cover the total area (especially for water because of attraction between water molecules) the next drop is located to the uncovered area. Moreover, the creation of air bubble is manually avoided with the aid of pipette tip pushing the liquid toward the air bubble to fill or eliminate it. The output of the system is captured by Agilent DSA91304A Infiniium Oscilloscope. The micropipette is also used to remove liquid from the container and empty it. Then, the container is dried by a compressed gas duster.

2.2.2.4 Calibration and Unknown MUT Characterization

Considering ϵ' and ϵ'' of MUT simultaneously affect both phase and magnitude of output signal in FD, the behavior of the system is described by testing 12 reference MUTs. By polynomial curve-

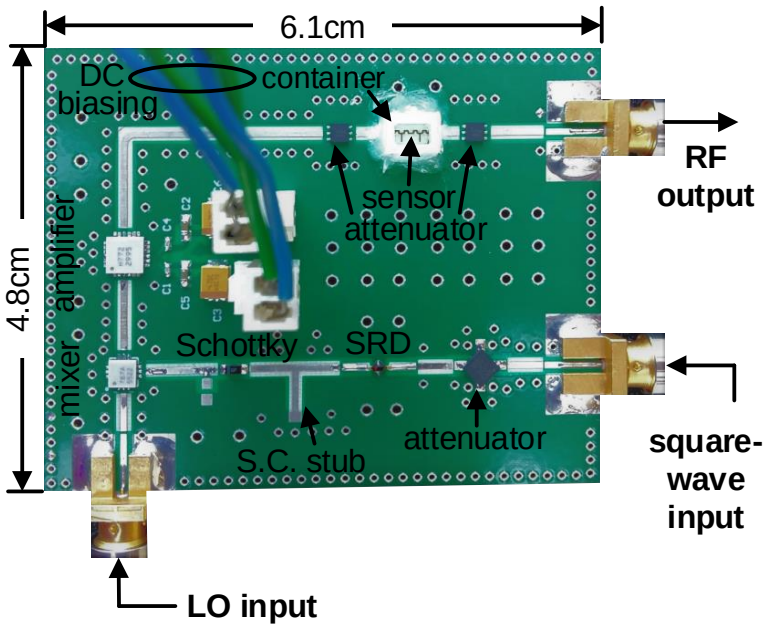

Figure 2.50: Fabricated miniaturized contact-based UWB TDS system. Reprinted with permission from [5].

fitting, ϵ' and ϵ'' are estimated according to the following equations

$$\begin{aligned}\epsilon' = p_{00} + p_{10} * \Delta\phi + p_{01} * \Delta Mag + \\ p_{20} * (\Delta\phi)^2 + p_{11} * \Delta\phi * \Delta Mag + \\ p_{30} * (\Delta\phi)^3 + p_{21} * (\Delta\phi)^2 * \Delta Mag,\end{aligned} \tag{2.9}$$

$$\begin{aligned}\epsilon'' = q_{00} + q_{10} * \Delta Mag + q_{01} * \Delta\phi + \\ q_{20} * (\Delta\phi)^2 + q_{11} * \Delta\phi * \Delta Mag + \\ q_{02} * (\Delta Mag)^2.\end{aligned} \tag{2.10}$$

In (2.9), ϵ' depends on $\Delta\phi$ with the third order, while it depends on ΔMag with the first order relationship, reflecting the fact that ϵ' is mainly affected by $\Delta\phi$. The coefficients are shown in Fig.

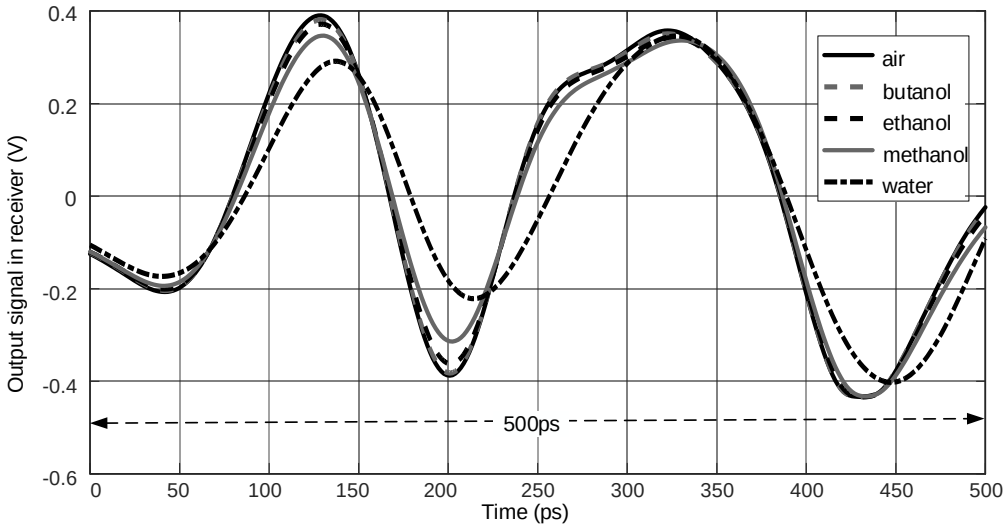

Figure 2.51: Measured output voltage of the system in TD for different reference MUTs. Reprinted with permission from [5].

2.53.

From the behavioral model of the system, three unknown MUTs are characterized with errors less than $0.1|\epsilon^*|$ in both ϵ' and ϵ'' from 3.28-10GHz (Fig. 2.54).

Table 2.2 compares the proposed system in this work with the commercially available product Keysight N1501A dielectric performance probe kit [39] which operates from 500MHz to 50GHz. In N1501A product, the measurements are made by immersing the probe into MUTs. The N1501A is based on FD measurement technique by using a network or impedance analyzer. Because of measurement in TD, the proposed system generates RF/microwave signal with a very cheap function generator (33250A) and a customized RF pulse generator circuitry, while the N1501A still dependents on expensive network or impedance analyzer for RF/microwave signal generation. The bandwidth of the proposed system could be enhanced by using combined FD-TD technique as shown in [40] and redesigning the mixers and the sensor for higher frequency operation. To reduce overall cost of the system, replacing a fast analog-to-digital (ADC) board with oscilloscope is necessary. Advantages of the proposed system appear in terms of sensor miniaturization and MUT size. While this system only needs a 0.3μL volume of liquid for sensing, the N1501A demands at least 15.7μL sample volume to confine the total electric field generated at probe. In terms of

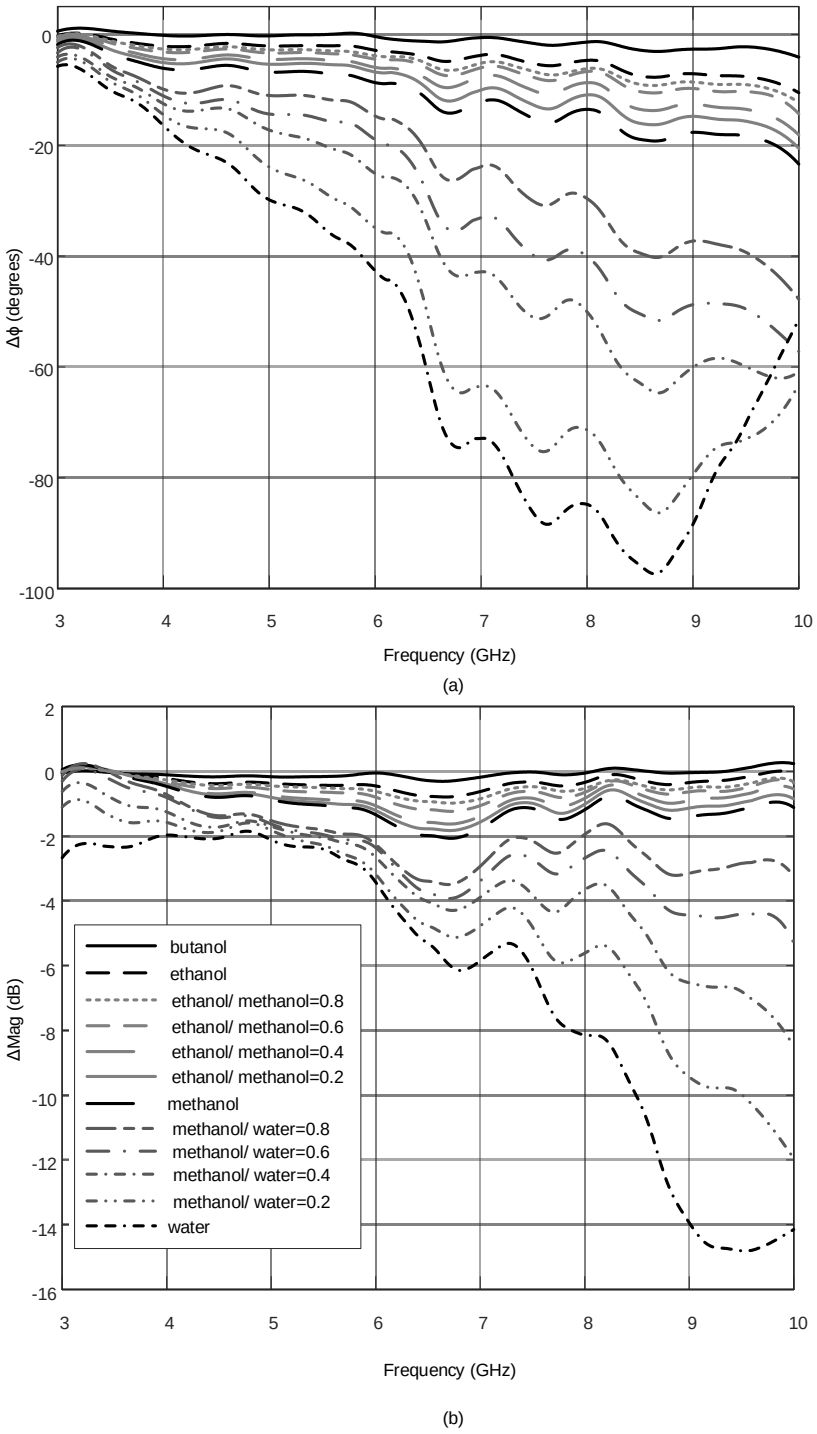

Figure 2.52: Calculated (a) $\Delta\phi$ and (b) ΔMag in FD using FFT of TD output voltage. Reprinted with permission from [5].

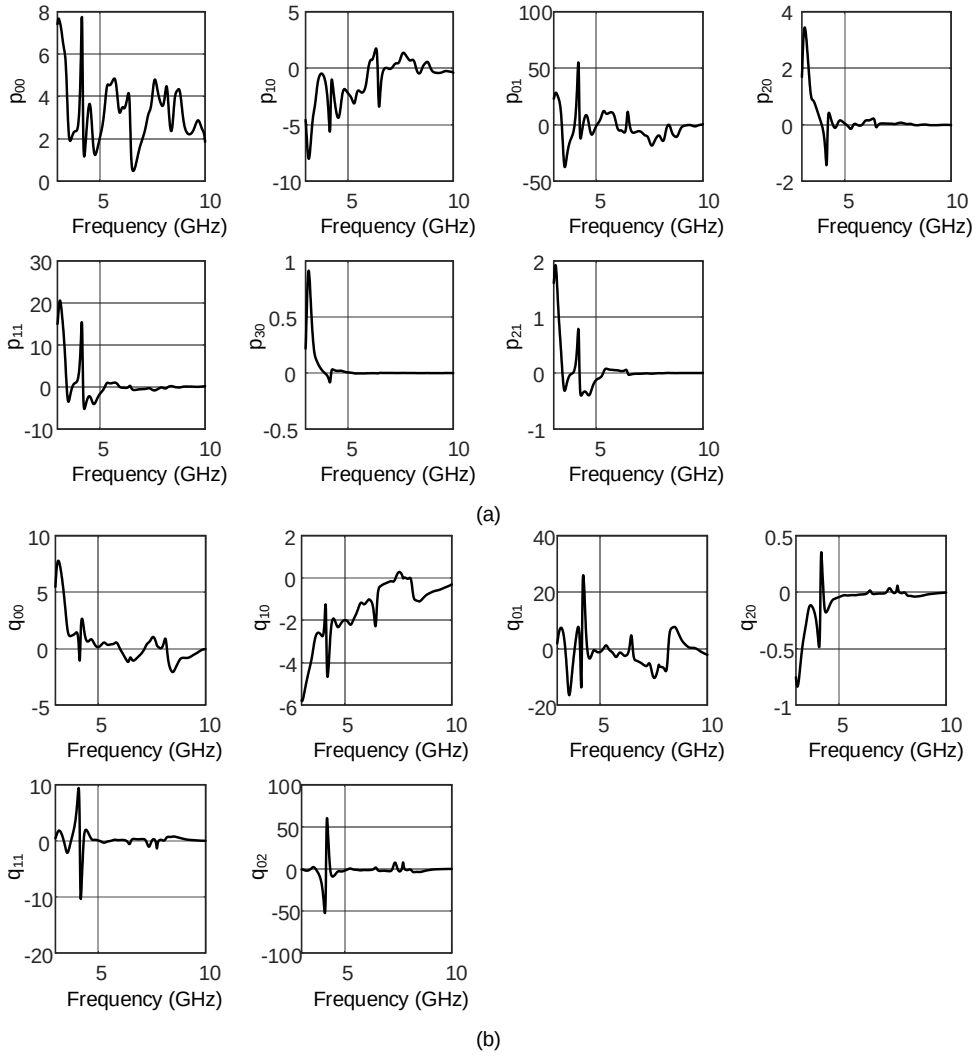

Figure 2.53: Curve-fitting coefficients for (a) ϵ', and (b) ϵ''. Reprinted with permission from [5].

accuracy, maximum error is $0.05|\epsilon^*|$ in ϵ' and $0.1|\epsilon^*|$ in ϵ'' in N1501A measurements as shown in Fig. 2.55; however, maximum error is $0.1|\epsilon^*|$ in ϵ' and also $0.1|\epsilon^*|$ in ϵ'' in the proposed system within the UWB range. In terms of dynamic range, N1501A is capable of measuring MUTs with $\epsilon'<100$ and $tan\delta>0.05$; but, according to the measurements in the proposed system, the maximum measured ϵ' is for water which is less than 80, and the minimum $tan\delta$ belongs to butanol which is larger than 0.22. However, the simulations show that the system can detect MUTs with $tan\delta$ larger than 0.02.

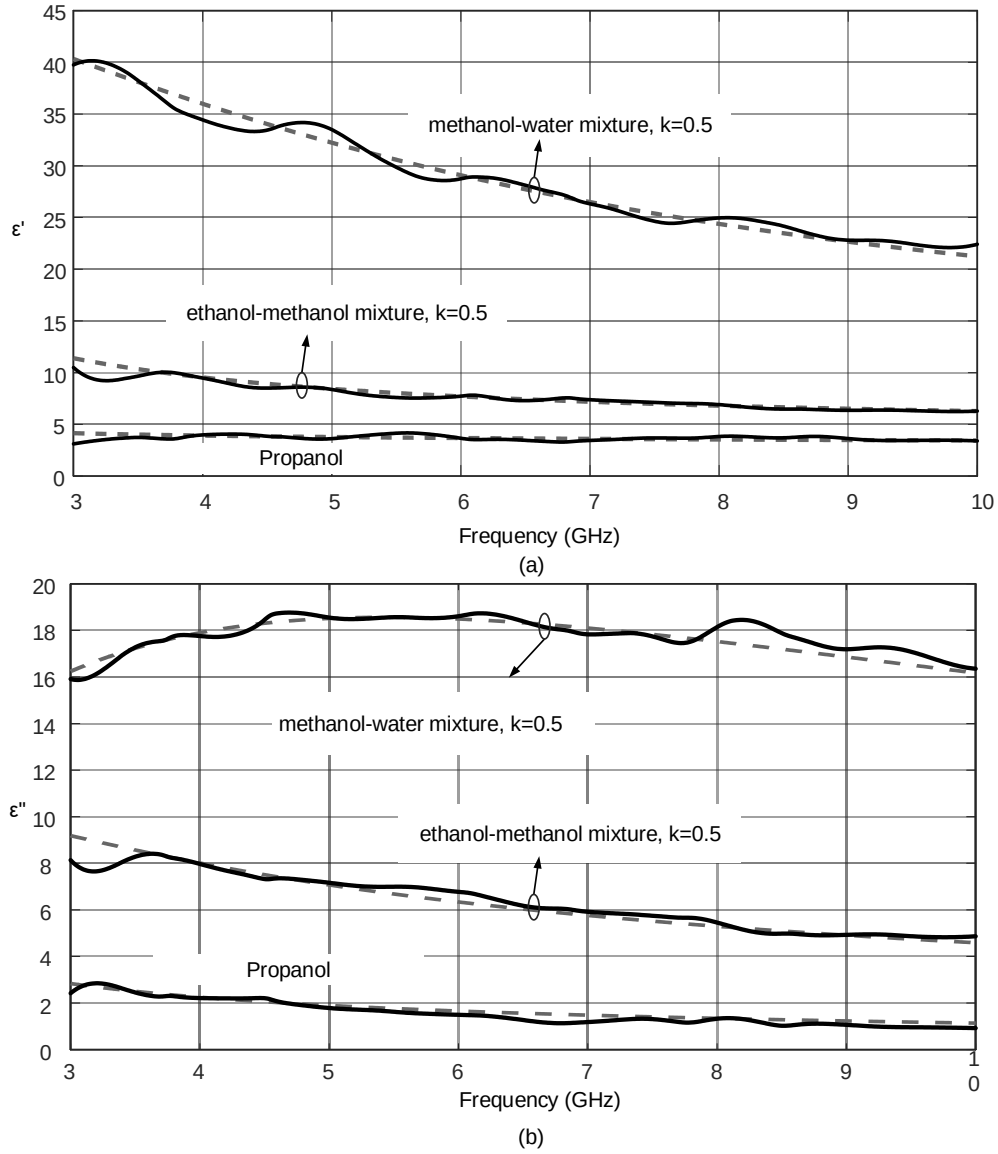

Figure 2.54: Characterization of unknown MUTs (a) ϵ', and (b) ϵ''. Reprinted with permission from [5].

2.2.2.5 Conclusion

The design, fabrication, and testing of a UWB spectroscopy system in TD has been presented. The design procedure of a miniaturized sensor has been discussed in detail, based on maximizing the sensitivity and achieving the broadband matching condition. The input signal of sensor

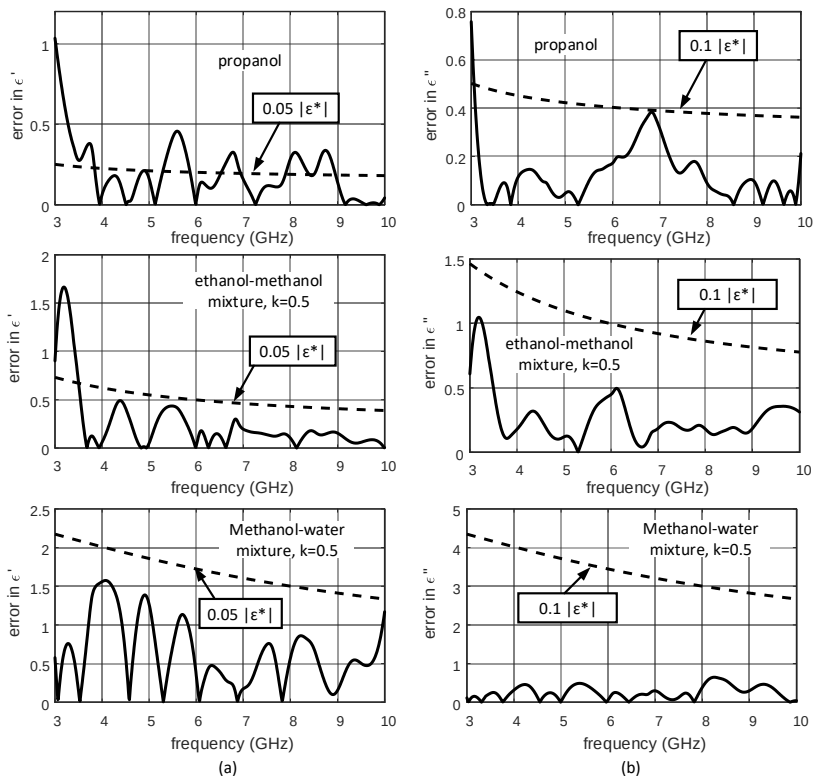

Figure 2.55: Accuracy in the proposed system compared with the Keysight N1501A dielectric probe kit: (a) maximum error in ϵ' and (b) error in ϵ''. Reprinted with permission from [5].

is generated through a UWB transmitter employing an SRD, a short-circuited stub, a mixer, and an amplifier, and the output signal of sensor is captured by an oscilloscope in TD. The phase and magnitude of output signal for reference MUTs are related to ϵ' and ϵ'' of the MUTs, using polynomial relationships which take into account the effect of ϵ' and ϵ'' on both phase and magnitude. With these polynomials, the ϵ' and ϵ'' of three unknown MUTs have been successfully determined with the maximum error of each one less than $0.1|\epsilon^*|$ from 3.28-10GHz.

2.3 Dual-Comb Dielectric Spectroscopy

2.3.1 Dual-Comb Dielectric Spectroscopy for Magnitude Measurement

2.3.1.1 Introduction

Time-domain dielectric spectroscopy (TDS) is a broadband technique based on measuring the MUT with a single short-duration pulse excitation which extends over the desired frequency range. Traditional TDS systems utilize bulky and expensive time-domain reflectometry equipment [41]. Miniaturized TDS systems have been recently reported [1], [4], [5]. [1] suggests a miniaturized contactless TDS technique by using two UWB Vivaldi antennas located in the near-field range with the MUT in between. A pulse-shaping circuit consists of an SRD and a short-circuited stub along with an upconverter and an amplifier generate the desired UWB excitation pulse. [4] and [5] provide miniaturized contact-based UWB techniques by using UWB planar sensors with the MUT located on the top, while they employ a similar pulse generation method as in [1]. In spite of the fact that these works propose significant miniaturization in the sensing structure and the pulse generation, they would still need a bulky and expensive high-speed oscilloscope to capture the output UWB pulse.

Dual-comb spectroscopy (DCS) technique emerged in numerous spectroscopy systems in the optical region [42] is an appealing technique that can potentially be used in the microwave broadband dielectric spectroscopy systems. DCS requires two frequency combs to be combined in the microwave range and then be downconverted to low frequency range by a second order nonlinearity detector. This eliminates the need for a high-speed oscilloscope, while it still takes the advantages of TDS by only taking a single measurement. This paper proposes a miniaturized UWB DCS system in time domain for detection of liquid MUTs.

2.3.1.2 System Design

The block diagram of the proposed UWB DCS system is shown in Fig. 2.56. This system basically consists of two comb generators, a sensor, a power combiner, a high-pass filter (HPF),

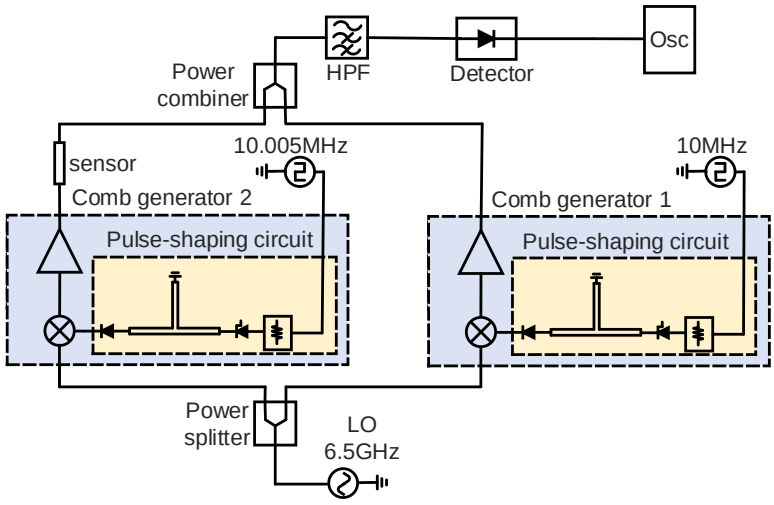

Figure 2.56: Block diagram of the proposed UWB dual-comb spectroscopy system. Reprinted with permission from [6].

a power detector, and a low-frequency oscilloscope. The comb generators output two pulse trains with slightly different pulse repetition frequencies (PRF) f_r and $f_r + \Delta f_r$, where f_r=10MHz and Δf_r=5KHz. One of the pulse trains passes through the sensor and then is combined with the other pulse train. Fig. 2.36(a) and (c) show the combined microwave signal in frequency and time domains, respectively. With Δf_r=5KHz, the samples in frequency domain (FD) have (3GHz/10MHz)$\times\Delta f_r$ = 150$\times\Delta f_r$ = 1.5MHz separation at 3GHz and (10GHz/10MHz)$\times\Delta f_r$ = 1000$\times\Delta f_r$ = 5MHz separation at 10GHz. While in TD, time-shift between the samples increases with the steps of 50ps. The combination experiences second order nonlinearity by a power detector which means that the two pulse trains are convolved in the FD. This results in the downconversion of the entire UWB information into a frequency range less than 5MHz in baseband (BB). Fig. 2.57(b) and (d) show the BB signal in FD and TD, respectively. Consequently, the BB signal can be captured by an oscilloscope with a much smaller sampling rate compared to the microwave signal (10MSps compared to 20GSps). The frequency spacing between samples in BB signal is fixed value equal to Δf_r=5KHz. The HPF is to suppress the out of band signal at frequencies less than 3GHz generated from the tail of the pulse. In described DCS system, the UWB 3-10GHz spectrum

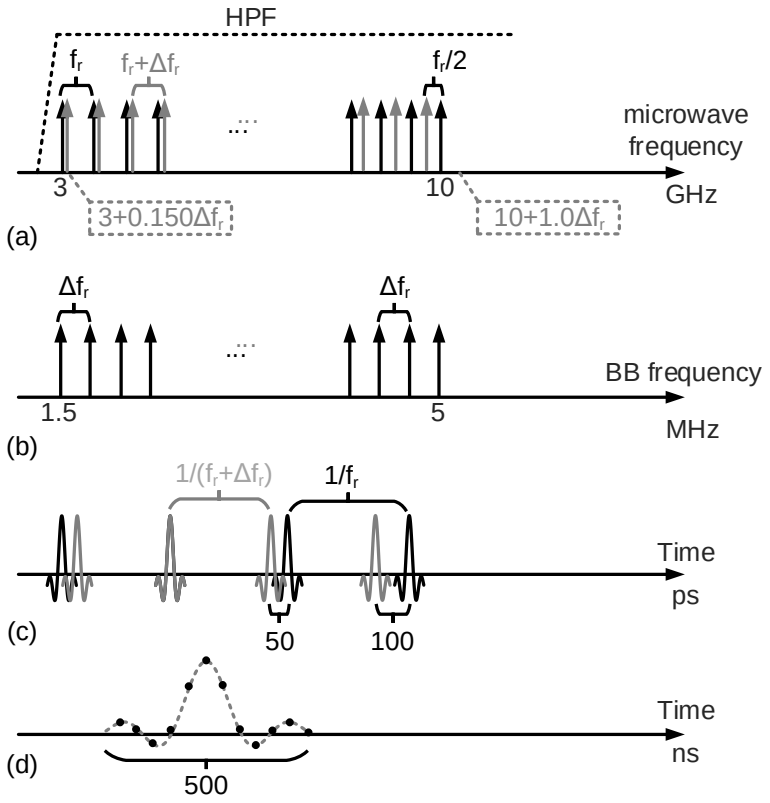

Figure 2.57: (a) Combination of two microwave frequency combs with different PRFs, (b) BB signal as the result of convolution through the second-order nonlinearity, (c) combination of microwave pulse trains with different periods in TD (Part (c) is the TD equivalent of (a)), (d) down-converted BB signal in TD (Part (d) is the TD equivalent of (b)). Reprinted with permission from [6].

with Δv=7GHz bandwidth is mapped to BB 1.5-5MHz spectrum with 3.5MHz bandwidth. The ratio of the UWB bandwidth to the BB bandwidth is called compression factor m=2000 which is equal to $f_r/\Delta f_r$. The selection of f_r=10MHz and Δf_r=5KHz is reasonable because the one-to-one mapping from microwave to BB is only maintained if the microwave bandwidth satisfies the following condition [42]

$$\Delta v \leq \frac{m f_r}{2} = \frac{{f_r}^2}{2\Delta f_r}. \tag{2.11}$$

Each of the UWB comb generators employ a square-wave generator with the desired PRF,

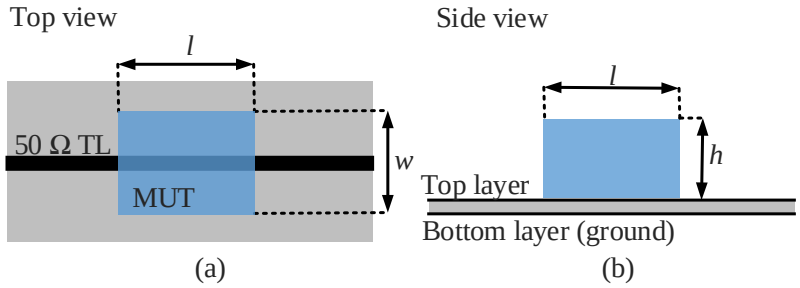

Figure 2.58: 50 Ω microstrip transmission line (TL) loaded by MUT, (a) Top view, (b) Side view. Reprinted with permission from [6].

a pulse-shaping circuit, an upconverter, and an amplifier. The pulse-shaping circuit essentially includes an SRD and a short-circuited stub to convert each period of the square-wave to a short duration pulse extended from DC to 3.5GHz, while an attenuator and a schottky diode are used to improve the input matching and reduce ringing, respectively [1]. The output of the pulse-shaping circuit is upconverted by 6.5GHz with the UWB mixer and amplified by the UWB amplifier. Since the input square-wave is periodic, the output signal of the UWB comb generator is sampled by the input PRF within 3-10GHz. Therefore, the number of comb lines is 700.

2.3.1.3 Sensor Design

A micostrip transmission line electrical parameters such as characteristic impedance, phase velocity, and losses change when it is covered by an MUT [34]. In this work, a 50Ω microstrip line is loaded with several MUTs including air, ethanol, and methanol, thereby the MUTs are detected according to the transmission responses of the loaded microstrip line. The covered area of the microstrip line affects the matching condition and the sensitivity in detection of different MUTs. The goal here is to design a sensor that satisfies the matching condition S_{11}<-10dB over UWB band, generates large magnitudes differences ΔMag compared to the unloaded case, and uses a minimum amount of MUT. Fig. 2.58 shows a 50Ω microstrip line on 0.338mm RO4350B substrate loaded by a rectangular MUT. The width, w=10mm, and the height, h=5mm, of the MUT are decided large enough to hold the total fringing field around the signal trace. The length,

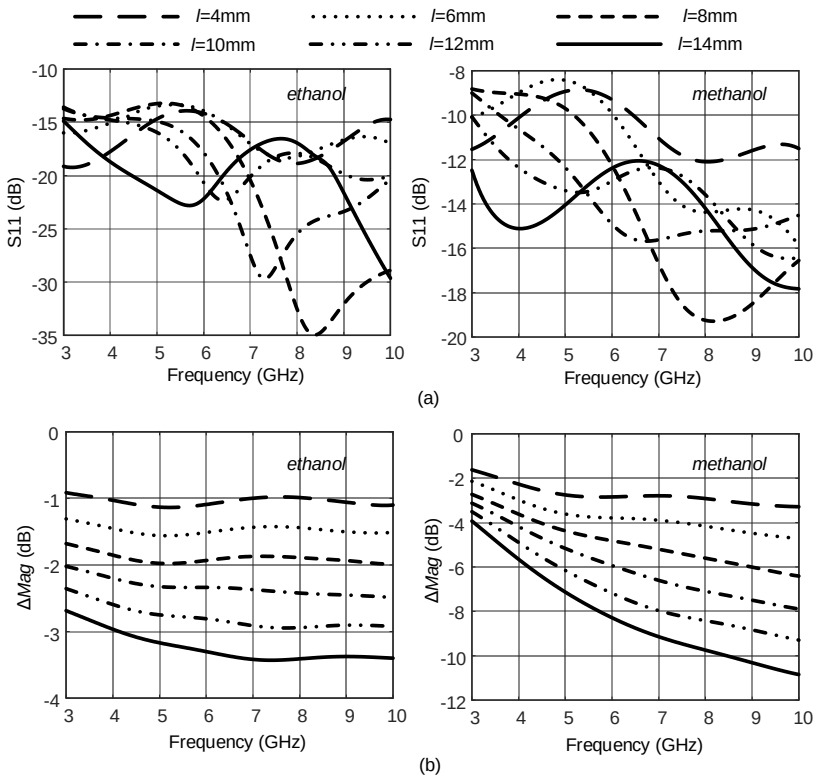

Figure 2.59: Simulation results of the sensor loaded by ethanol (left) and methanol (right) for different values of l, (a) S11 and (b) ΔMag. Reprinted with permission from [6].

l, of the MUT significantly affects the reflection and transmission responses of the sensor. The HFSS simulation results of S_{11} and ΔMag for l=4,6,8,10,12,14mm and different MUTs are shown in Fig. 2.59. According to this figure, the sensor satisfies matching condition for l=12mm and l=14mm. Choosing l=14mm for the length of MUT, the sensor generates minimum ΔMag=-2.7dB for ethanol at 3GHz.

2.3.1.4 System Implementation and Measurements

The photograph of fabricated microstrip sensor is shown in Fig. 2.60(a). The substrate is RO4350 with 0.338mm thickness, ϵ'=3.66 and tanδ=0.0031 and the trace width is 0.7mm. The polypropylene container made by CNC machining. The simulation and measurement results for the S_{21} of loaded line are shown in Fig. 2.60(b) while the measured $S_{11}<$-10dB.

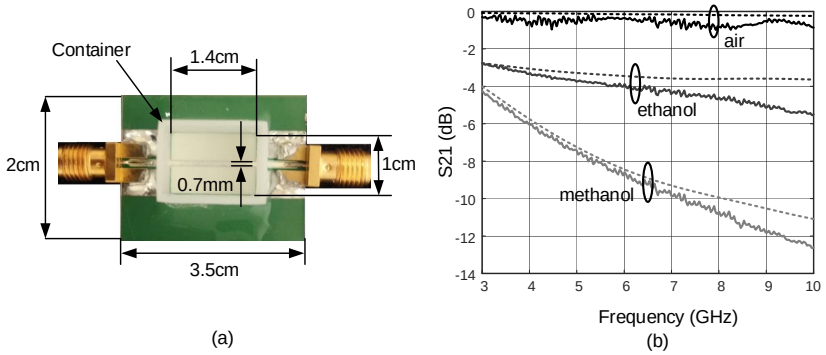

Figure 2.60: (a) Photograph of fabricated microstrip sensor, (b) S21 simulation (dotted lines) and measurement (solid lines) results for different MUTs. Reprinted with permission from [6].

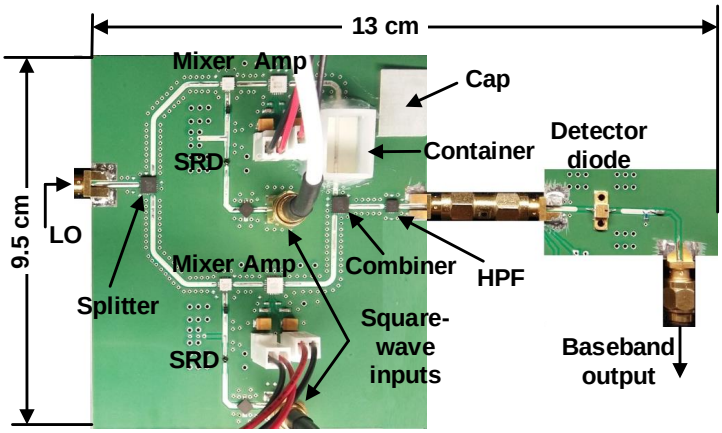

Figure 2.61: Photograph of fabricated UWB DCS system. Reprinted with permission from [6].

Fig. 2.61 shows the photograph of UWB DCS system. Each pulse-shaping circuit includes an MD835-H20 SRD, a 4.5mm short-circuited stub, a CDBU0130L Schottky diode, and a GAT-6+ attenuator, and the square-wave input voltages are generated by DG4162 function generator. HMC787A mixers and HMC772LC4 amplifiers are used for upconversion and amplification, respectively, while the 6.5GHz LO frequencies are generated by an E8267D PSG Vector Signal Generator and an EP2C+ power splitter. The frequency combs are combined by EP2C+, filtered by

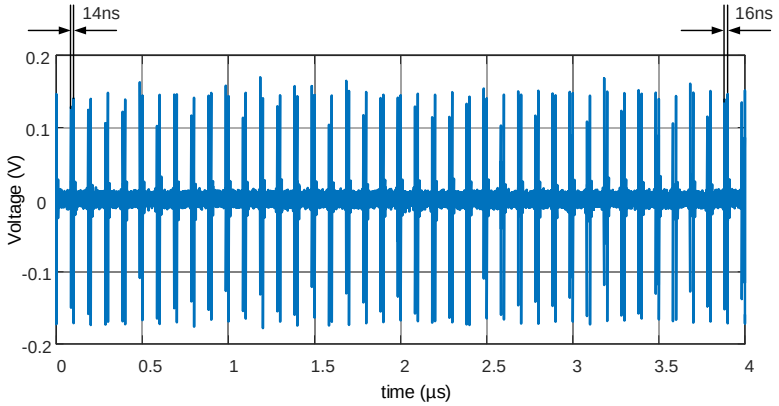

Figure 2.62: Voltage captured at the output of HPF showing the combination of two frequency combs. Reprinted with permission from [6].

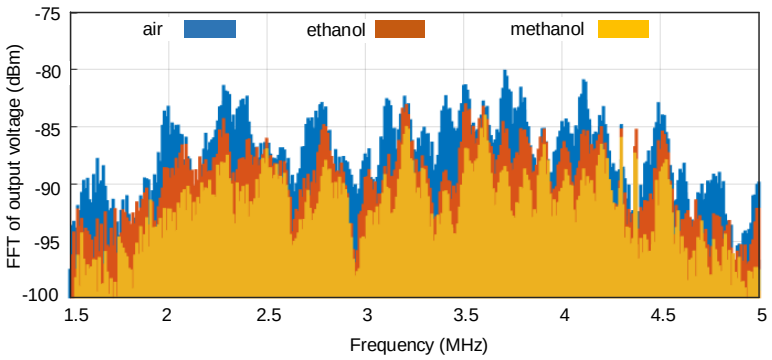

Figure 2.63: Output of the system in FD. Attenuation of ethanol is larger than air, and attenuation of methanol is larger than ethanol. Reprinted with permission from [6].

XHF-23+ HPF, and experience nonlinearity by diode detector DT2012Z1. Finally, an DSA91304A oscilloscope captures the output voltage.

Fig. 2.62 shows a window of the combined frequency combs in TD captured after the HPF. As can be seen from this figure, the time delay between frequency combs increases from 14ns on the left to 16ns on the right because of the difference in comb PRFs. Fig. 2.63 shows output of the system in BB for different MUTs. According to this figure, the FFT magnitude for methanol

is smaller than ethanol, and for ethanol is smaller than air as predicted by the simulations and sensor measurements. The 1.5-5MHz signal in Fig.2.63 contains MUT information in 3-10GHz frequency range.

2.3.1.5 Conclusion

A miniaturized UWB dual comb spectroscopy system has been presented. In this system, the effect of liquid chemicals on voltage magnitude in the microwave range is mapped to the baseband. Therefore, this is an effective method to distinguish among MUTs in a wide frequency range.

2.3.2 Dual-Comb Dielectric Spectroscopy for Phase and Magnitude Measurements

2.3.2.1 Introduction

Dual-comb spectroscopy is a novel TDS tool that enables fast, miniaturized, self-sustained, and low-cost with high precision solution for broadband spectroscopy. In DCS, a broadband comb interrogates an MUT and then mixed with a second comb with slightly different repetition rate. The mixing result is a low-frequency comb that contains broadband information of the MUT. Mapping of the broadband information to the low-frequency region, greatly reduces the receiver complexity because the low-frequency information can be sampled with a basic ADC card. Therefore, it is possible to implement a UWB/microwave system based on DCS technique as a standalone system independent of the laboratory facility. Since the emerge of DCS [43], a large number of proof-of-concept experiments in optical domain have been presented in literature [44, 45, 46, 47]. As a proof of principle, the first demonstration of a miniaturized DCS system for dielectric spectroscopy in microwave UWB frequency range was presented by the authors in [6]. In [6], two free-running frequency combs are combined and then the combination experiences second-order nonlinearity by a microwave diode detector to map the UWB information of an MUT to a baseband (BB) frequency in 1.5–5 MHz. Despite the successful detection of MUTs according to the magnitude response of the system in [6], a complete characterization of MUTs requires evaluation of both magnitude and phase responses. This work, demonstrates a phase-sensitive microwave UWB DCS system that has mutually coherent combs through phase-locking all the signal generators involved in the system. Therefore, phase measurement and averaging of the output data become feasible. By having both magnitude and phase results, complete characterization of ethanol-methanol mixtures achieved and their ϵ' and ϵ'' are reported. With the frequency planning suggested in this system, the real broadband information of an MUT is mapped in 0.3–1 MHz. In addition, a mixer is used for heterodyning combs instead of using a combiner and a diode detector proposed in [6]. Mixer output is a power quantity while the diode detector output is a voltage quantity and the mixer can provide higher level of detectable signal at BB.

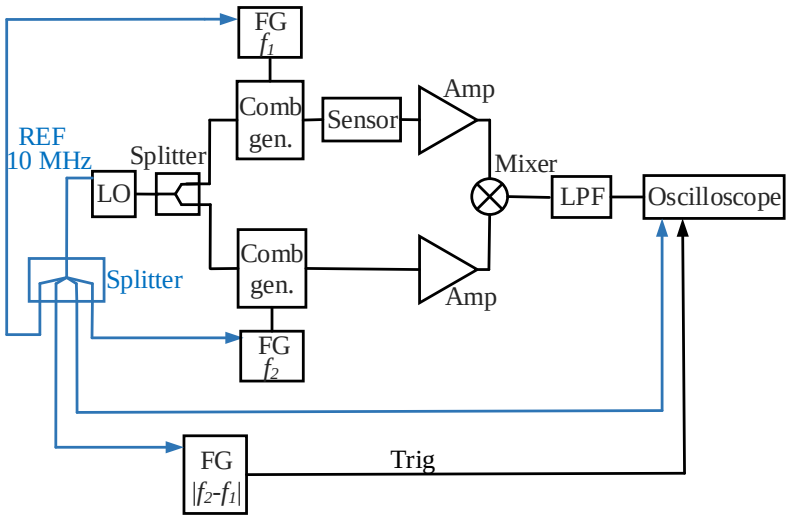

Figure 2.64: Block diagram of the proposed UWB dual-comb spectroscopy system along with the phase-locking network. Reprinted with permission from [7].

2.3.2.2 System Design

Dual-comb spectroscopy relies on heterodyning two broadband UWB frequency combs with slightly different repetition rates, to map the entire UWB frequency properties of MUTs into the BB domain. DCS is a well-known spectroscopy technique and its principles already described in the literature [48, 42]. The building block and system operation of the DCS using microwave components are described here. The architecture of the proposed UWB DCS system is shown in Fig. 2.64. This system basically consists of two comb generators, a sensor, a mixer, a low-pass filer (LPF), and a low-frequency oscilloscope. The comb generators output two frequency combs with slightly different pulse repetition frequencies f_r and $f_r + \Delta f_r$. One of the combs is sent through the sensor, inherits the microwave intrinsic properties of the MUT, and then mixed with the second comb by a UWB mixer. The mixer output is a full translation of the MUT microwave properties into the BB. This way, both amplitude and phase information of the microwave signal are simultaneously mapped into the BB, low-pass filtered and then captured by the low-frequency

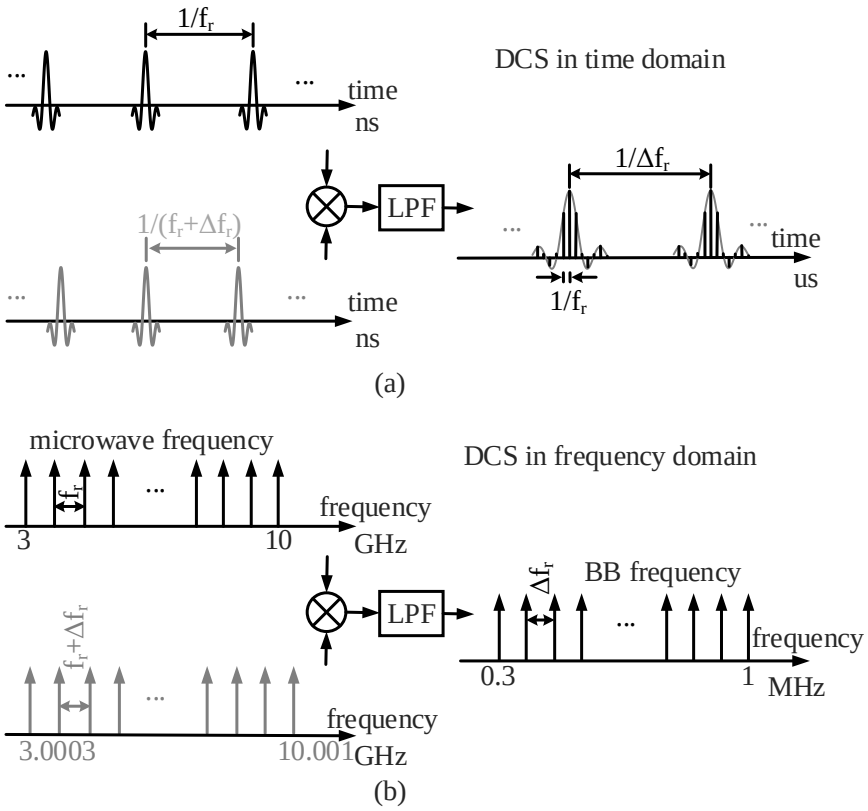

Figure 2.65: Principle of UWB dual-comb spectroscopy in time and frequency domains. The frequency comb that carries the UWB transmission properties of an MUT is mixed with the second comb and then low-pass filtered. (a) The output in time-domain is a periodic signal with the period of $1/\Delta f_r$ = 1 ms sampled by f_r rate. (b) The output in frequency-domain is a BB comb with a tooth spacing equal to Δf_r = 1 kHz. Reprinted with permission from [7].

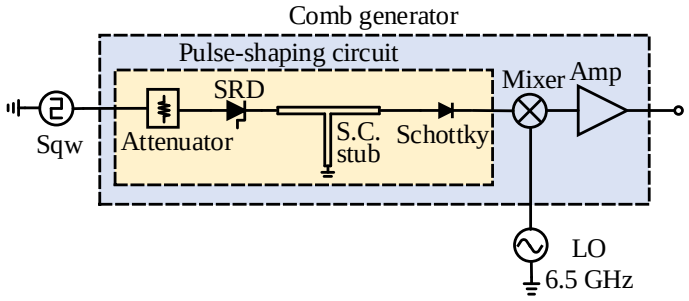

Figure 2.66: Block diagram of the comb generator. Reprinted with permission from [7].

oscilloscope. The DCS scheme shown in Fig. 2.64 is phase-sensitive, hence, all signal sources and the oscilloscope are phase-locked by a common REF signal supplied from the local-oscillator (LO). If the two sources are not phase-locked, the oscilloscope will only be able to trigger on one of the waveforms while the other waveform will appear to walk. The output of DCS system results from the interaction of multiple sources operating at different frequencies and the TD method of measurement depends on averaging the output signal to increase the signal-to-noise ratio (SNR). In this regard, it is necessary to freeze the output waveform on oscilloscope through synchronizing all clock sources involved in the system.

Fig. 2.65(a) and (b) represent the conceptual operation of the DCS system in TD and frequency domain (FD), respectively. The PRFs of the combs are selected to be 10 MHz and 10.001 MHz that result in f_r = 10 MHz and Δf_r = 1 kHz. The TD representation of DCS, reveals multiplication of two microwave combs by the mixer. In FD, the mixer output contains convolution of the combs which translates the entire 3–10 GHz microwave comb into a 0.3–1 MHz BB comb with the frequency spacing between its teeth equal to Δf_r = 1 kHz. The mixer output signal is a comb expanded in time, sampled every $1/f_r$ = 10 μs and repeated with the period of $1/\Delta f_r$ = 1 ms. For this reason, the oscilloscope in Fig. 2.64 is externally triggered by a separate source with the period of 1 ms. The mixer output is low-pass filtered at 80 MHz to avoid aliasing signals above the Nyquist frequency that can be generated from the mixer's leakage and harmonics. The LPF output can be sampled by 160 MHz or a higher sampling rate. In the described DCS system, the UWB 3–10 GHz spectrum with Δv = 7 GHz bandwidth is mapped to the BB 0.3–1 MHz spectrum with 0.7 MHz bandwidth. The ratio of the UWB bandwidth to the BB bandwidth is called compression factor m = 10000 which is equal to $f_r/\Delta f_r$. The selection of f_r = 10 MHz and Δf_r = 1 kHz is reasonable because the one-to-one mapping from microwave to BB is only maintained if the microwave bandwidth satisfies the following condition [42]

$$\Delta v \leq \frac{m f_r}{2} = \frac{{f_r}^2}{2\Delta f_r}. \tag{2.12}$$

Based on this constraint, for a given comb repetition rate and microwave bandwidth, the minimum required time to acquire a spectrum equals $\frac{1}{\Delta f_r}$ = 1 ms.

In the DCS system, each UWB comb generator block employs a square-wave (sqw) generator with the PRF equal to f_r (or $f_r + \Delta f_r$), a pulse-shaping circuit, an upconverter, and an amplifier (Fig. 2.66). The pulse-shaping circuit includes an SRD and a short-circuited stub to convert each period of the square-wave input to a short duration pulse extended from DC to 3.5 GHz [1]. During the forward-biased state, the SRD stores electric charge, and when it is switched to the reverse-biased state, it releases that charge in a short duration equal to the minority carrier lifetime, τ_R. The rise-time of the input sqw must be less than τ_R in order to obtain the maximum achievable amplitude . After τ_R, the diode abruptly turns off. This instant transition time, τ_t, that appears at the output of SRD, is converted to a short-duration pulse after combining with its reflected and delayed version from the short-circuited stub. The resultant combination has a short-duration pulse with a rise-time and a fall-time determined by the SRD and a duration adjusted by the length of the short-circuited stub. For completion of a transition in reverse-biased state, $\tau_R + \tau_t$ must be smaller than the half-period of the input square-wave, $1/(2f_r)$, as given below

$$\tau_R + \tau_t < 1/(2f_r). \tag{2.13}$$

Equation (2.13) is another criteria for choosing f_r in the DCS system. In the pulse-shaping circuit, an attenuator and a Schottky diode are used to improve the input matching and reduce ringing, respectively [1]. The output of the pulse-shaping circuit is upconverted by 6.5 GHz with a UWB mixer and amplified by a UWB amplifier. Since the input sqw is periodic in TD, the output voltage of the UWB comb generator in FD corresponds to a frequency comb of evenly spaced teeth with the frequency of the nth tooth given by f_r+$n\Delta f_r$. Therefore, the number of comb lines is 700 in 3–10 GHz frequency range.

The microstrip transmission line electrical parameters such as characteristic impedance, phase velocity, and losses change when it is covered by an MUT. In this work, a 50Ω microstrip line is

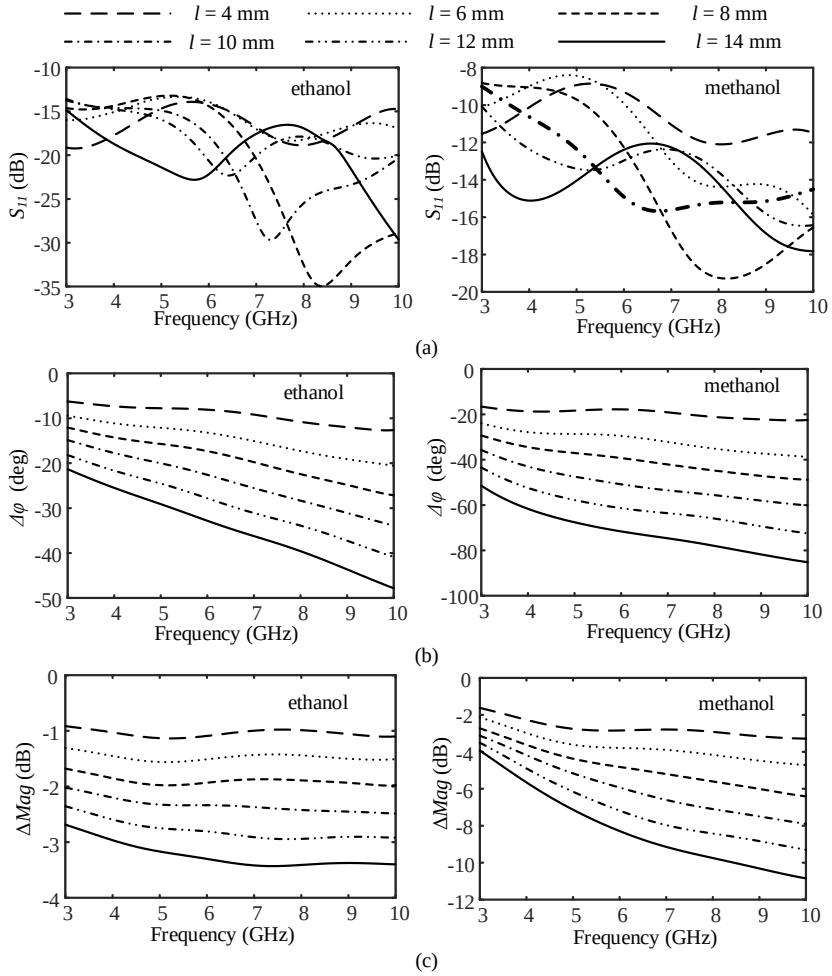

Figure 2.67: Simulation results of the sensor loaded by ethanol (left) and methanol (right) for different values of l, (a) S11 (b) ΔMag, and (c) $\Delta\phi$. Reprinted with permission from [7].

employed as a sensor for detecting intrinsic properties of different MUTs while directly loading the line. Thereby the MUT properties are launched on the transmission responses of the loaded microstrip line. The covered area of the microstrip line affects the matching condition and the magnitude and phase sensitivity in detection of different MUTs. The goal here is to design a sensor which (i) satisfies matching condition for reflection coefficient S_{11}<-10 dB over the UWB band, (ii) generates a large phase difference $\Delta\phi$ and magnitude difference ΔMag compared to the unloaded line ($\Delta\phi$ = phase$(S_{21})_{MUT}$-phase$(S_{21})_{air}$ and ΔMag = dB$(S_{21})_{MUT}$-dB$(S_{21})_{air}$), and (iii) uses a minimum amount of MUT. Fig. 2.58 shows a 50 Ω microstrip line on 0.338 mm

RO4350B substrate loaded by a liquid MUT which is surrounded by a rectangular shape container. The width, w = 10 mm, and the height, h = 5 mm, of the MUT are decided small to consume minimum amount of MUT, but large enough to hold total fringing field around the signal trace. The length, l, of the MUT significantly affects the reflection and transmission responses of the sensor. The full-wave simulation results of S_{11}, $\Delta\phi$, and ΔMag for l = 4, 6 ,8 ,10 ,12 ,14 mm and different MUTs, ethanol and methanol, are shown in Fig. 2.67. According to this figure, the sensor satisfies matching condition for l = 12 mm and l = 14 mm. Choosing l = 14 mm for the length of MUT, the sensor requires 0.7 mL of liquid MUT and it generates minimum $\Delta\phi$ = -22 degrees and ΔMag = -2.7 dB for ethanol at 3 GHz. According to Fig. 2.67(b) and (c), the sensitivity of the sensor improves in both magnitude and phase by increasing l.

The fabricated sensor along with the measurement results are shown in Fig. 2.68. Fig. 2.68(a) shows the transmission line and the sesning area surrounded by a polypropylene (PP) ($\epsilon_r = 2.2$) container. Because of the small dielectic contant of PP and its thin 0.8 mm wall thickness, its effect on the transmission response of the microstrip line is considered negligible. In all tests, the container is filled with MUT and saturated. The value of S_{11}, for all MUTs, is always less than -9.6 dB over 3–10 GHz as shown in Fig. 2.68(b). According to 2.68(c) and (d), $\Delta\phi$ values for ethanol ranges from -22.7 to -51.6 degrees and ΔMag from -2.5 dB to -4.6 dB. $\Delta\phi$ values for methanol ranges from -51.8 to -89.1 degrees and ΔMag from -3.9 dB to -11.7 dB.

2.3.2.3 System Implementation and Measurements

The photograph of fabricated DCS system is shown in Fig. 2.69. The system fabricated on the high-frequency and low-loss RO4350B substrate with ϵ' = 3.66, tanδ = 0.0031, and thickness = 0.0338 mm. The comb generators, sensor, amplifiers, mixer, and LPF can be seen in this figure. The input sources of the system consist of two square-wave signals (sqw1 and sqw2 in Fig 2.69) generated from a two-channel DG4162 arbitrary waveform generator, a 6.5 GHz signal generated from an E8267D PSG vector signal generator, and DC voltages for biasing the amplifiers. The output of the system is captured by a DSA91304A oscilloscope. Because the output PRF is 1 kHz, the oscilloscope is externally triggered by a 1 kHz sqw signal produced by a 33250A

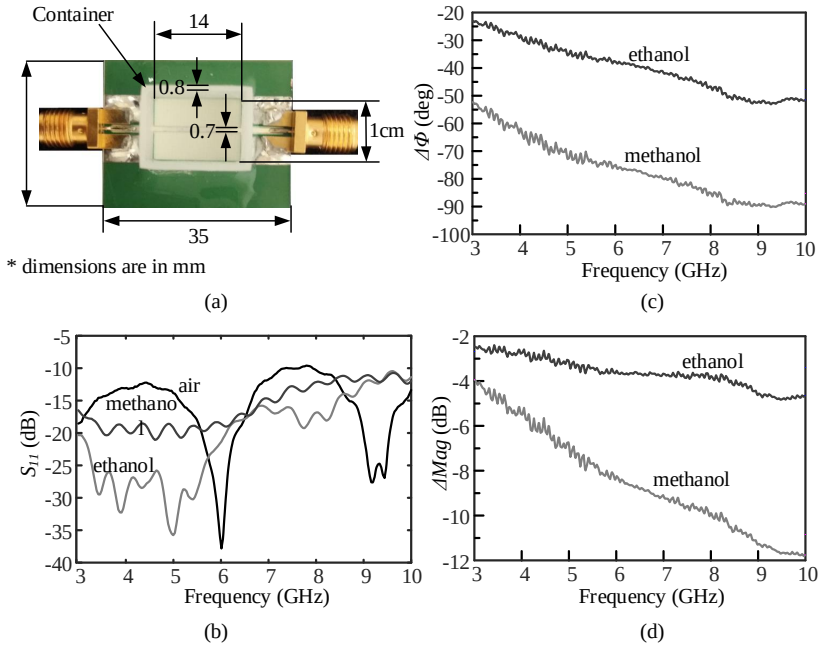

Figure 2.68: (a) Photograph of the fabricated microstrip sensor. (b) S_{11} measured for air, ethanol, and methanol, (c) ΔMag measured for ethanol and methanol, (d) $\Delta\phi$ measured for ethanol and methanol. Reprinted with permission from [7].

function/arbitrary waveform generator. All sources and the oscilloscope must be synchronized by a reference clock and to do so the 10 MHz OUT port of the E8267D LO, as the reference clock, is equally divided to four signals by a ZN8PD-113-S+ splitter, and these signals are connected to the 10 MHz IN port of the sources and the oscilloscope. The LO REF signal and the trigger signal are shown in Fig. 2.70(a) and (b), respectively. The sqw inputs, with 10 MHz and 10.001 MHz PRFs are shown in Fig. 2.70(c) and (d), respectively. The input sqws are phase aligned and then applied to the comb generators. Each source generates a voltage twice the amplitudes shown in Fig. 2.70, but because the input impedance of the DSA91304A oscilloscope is 50 Ω, half of the voltages appear in the oscilloscope input port. The higher amplitude of sqw1 compared with sqw2 is for generation of a larger Comb1 and can be regarded as a compensation for the insertion loss of the sensor in that path.

The BB pulse-shaping circuit consists of an MD835-H20 SRD with the typical values of

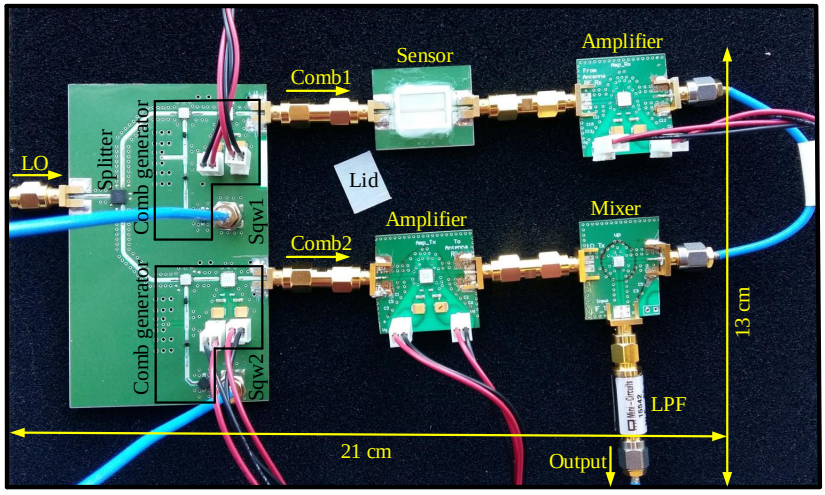

Figure 2.69: Photograph of the fabricated UWB dual-comb spectroscopy system. Reprinted with permission from [7].

τ_R = 20 ns and τ_t = 50 ps, a 4.5 mm length microstrip short-circuited stub, a CDBU0130L Schottky diode, and a GAT-6+ attenuator. The 20 ns minority carrier lifetime of the SRD is higher than the input sqw rise-time (5 ns) and less than the half-period of the input sqw (50 ns); consequently, a successful transition time is created at every input period with f_r = 10 MHz. The BB pulse-shaping circuit output is applied to an HMC787A mixer and then an HMC772LC4 amplifier for upconverstion and amplification, respectively. The 6.5 GHz LO signal of the mixer is equally divided by an EP2C+ power splitter, and then applied to the mixer LO port of each comb generator for upconversion.

Fig. 2.71(a) and (b) show TD signals from the comb generator outputs captured by the oscilloscope. The PRFs of TD signals in Fig. 2.71(a) and (b) are 10 MHz and 10.001 MHz, respectively. Therefore, the envelopes of Comb1 and Comb2 in FD are sampled by 10 MHz and 10.001 MHz, respectively. The equivalent FD Combs calculated by taking Fast Fourier Transform (FFT) of the measured TD signals are shown in Fig. 2.72(a) and (b). The -10-dB bandwidth of both combs are 7 GHz extended in the 3–10 GHz UWB frequency range. The noise level in Fig. 2.72(a) and (b) is around -90 dBm without averaging. Comb1 is passed through the sensor, amplified by an

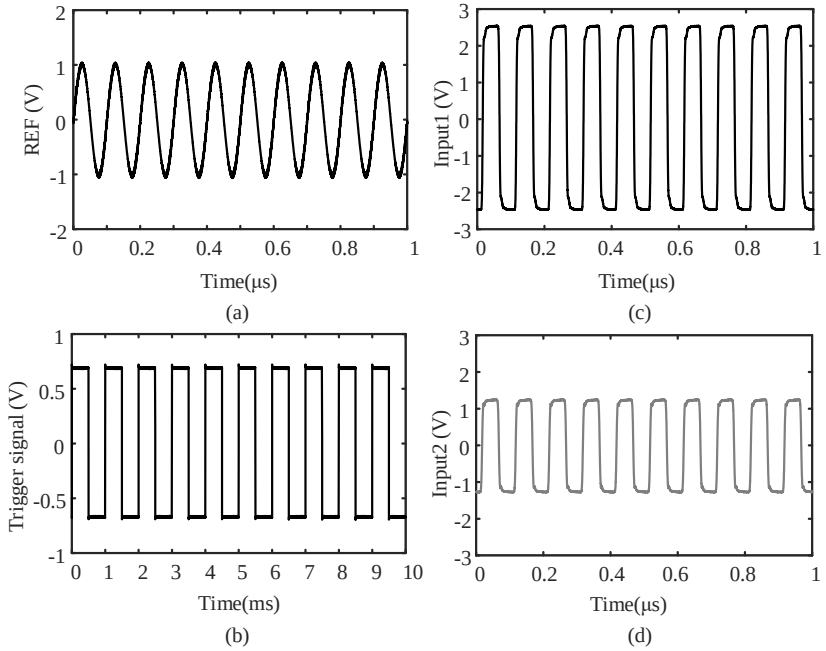

Figure 2.70: (a) REF signal from the 10 MHz OUT port of the LO that is connected to the 10 MHz IN ports of the function generators and the oscilloscope, (b) 1 kHz signal that is connected to the AUX TRIG port of the oscilloscope, (c) 10 MHz square-wave (sqw1) signal as the input of the comb generator 1, (d) 10.001 MHz square-wave (sqw2) signal as the input of the comb generator 2. Reprinted with permission from [7].

HMC772LC4 amplifier, and applied to the RF port of an HMC787A mixer. Comb2 is applied to the LO port of the mixer after amplification by another HMC772LC4 amplifier. The mixer output is low-pass filtered by an 80 MHz VLF-80+ LPF and then captured by 1 GSps sampling rate. The LPF cutoff frequency in this system can be any value larger than 1 MHz to keep the 0.3–1 MHz output signal. The smaller cutoff frequency reduces the required sampling rate and the noise power. The system output in TD is shown in Fig. 2.71(c) and its equivalent in FD calculated by taking FFT from the measured TD signal is shown in Fig. 2.72(c) for 0.3–1 MHz. The expanded versions of Fig. 2.71(c) and 2.72(c) are shown in Fig. 2.71(d) and 2.72(d), respectively. Because the length of TD information in Fig. 2.71(c) is 10 ms, its equivalent FD signal after taking FFT will have frequency resolution of 100 Hz. To show the equivalent FD with a higher resolution, the TD data is repeated for 40 ms before taking FFT. Thus, the frequency resolution in Fig. 2.72(d) is

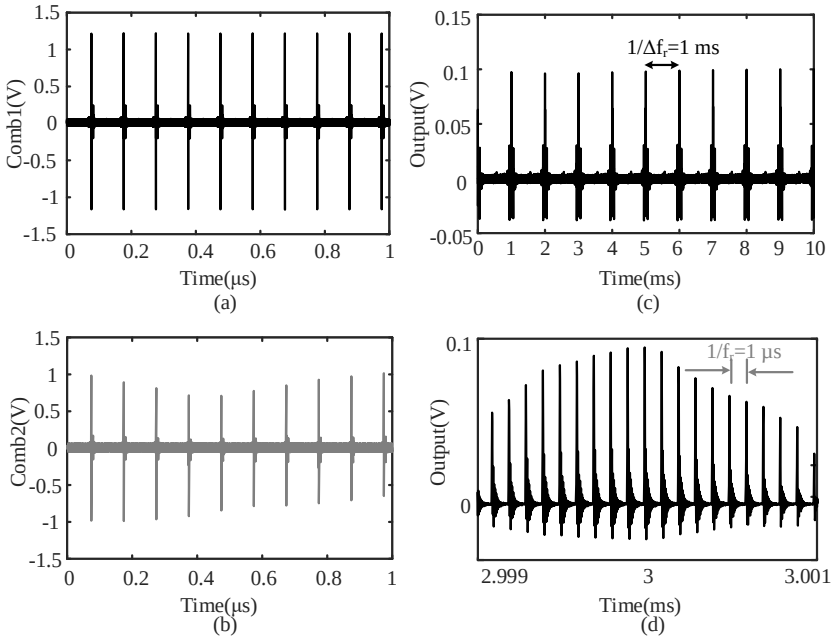

Figure 2.71: System measurement results in time domain. (a) Comb1 with PRF = f_r = 10 MHz, (b) Comb2 with PRF = $f_r + \Delta f_r$ = 10.001 MHz, (c) Output of the system with PRF = Δf_r = 1 kHz, and (d) Expanded version of the system output. Each tooth of the output signal is a pulse spread in time and sampled by a comb with the rate of f_r = 10 MSps. Reprinted with permission from [7].

25 Hz and the noise level is less than -120 dBm. Fig. 2.71(c) is the result of 4096 times averaging the system output. The system response does not vary during the measurement because when the system output is captured multiple times, the results merges to the same responses with negligible differences, and this proves the fact that the system is coherent.

The points that have been mapped from microwave frequencies happen every 1 kHz in the output signal in BB because the output PRF is 1 kHz (period = 1 ms) as presented in Fig. 2.71(c). Fig. 2.71(c) also shows that the system output is sampled every 0.1 μs as expected. The output signal within 0.3–1 MHz frequency range which contains all 3–10 GHz properties of the MUT can be seen in Fig. 2.72(c).

One of the main issues to be considered is SNR at receiver. The reason for using the amplifiers in Fig. 2.69 is to make sure that the SNR is higher than 20 dB. The local oscillator port of the mixer must be high enough for successful mixing of the two combs. The mixer works for 2.8-7.1 Vpp

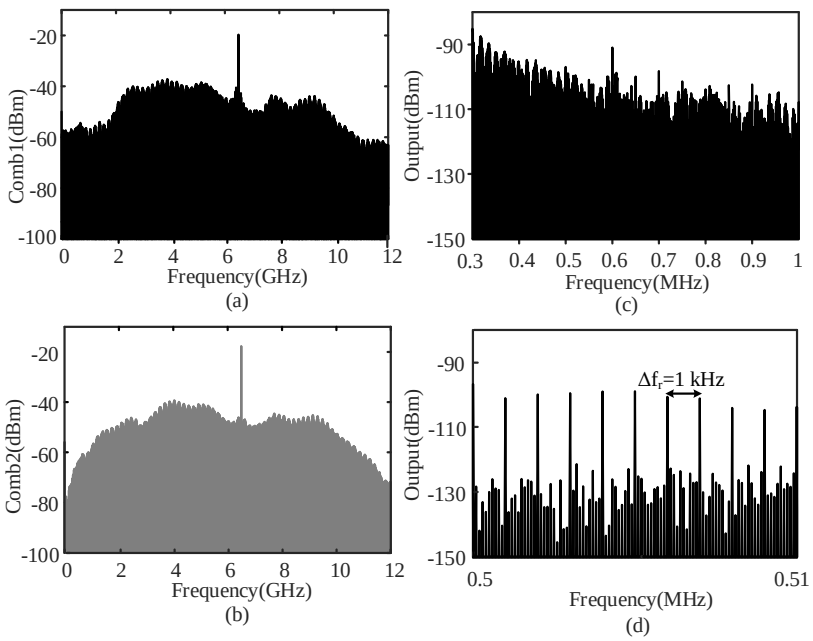

Figure 2.72: System results in frequency-domain calculated from measured time-domain data. (a) Comb1, (b) Comb2, (c) Output of the system, and (d) Expanded version of the system output. The output signal is a frequency comb with tooth spacing equal to Δf_r = 1 kHz. Reprinted with permission from [7].

LO drive. The LO level coming from Comb2 is adjusted to be between 3-4 Vpp in the system. In addition, the amplifier after sensor needs to remain linear for all MUTs. However, non-linearity in detection could not be an issue, because the reading range of oscilloscope is small in the range of 100mVpp. The voltage levels are checked by accommodating multiple RP(reverse polarity)-SMA male to male adaptors in the system.

One period of Comb1 in a short duration in TD is shown in Fig. 2.73(a). This figure has been measured by the sampling rate of 40 GSps. The ripples that can be seen in 74-75 ns and 77-78 ns are repeated periodically with the frequency of 6.5 GHz. They result from the leakage of 6.5 GHz LO signal in the output of comb generator circuitry. These ripples show themselves as a spike at 6.5 GHz in spectrum shown in Fig. 2.72(a). Fig. 2.73(b) shows a single comb tooth as calculated by taking FFT from Comb1 while repeated for 1 ms. According to Fig. 2.73(b), the spectrum 1 kHz (= Δf_r) below or above a comb line is $\sim$53 dB smaller. Therefore, the individual comb

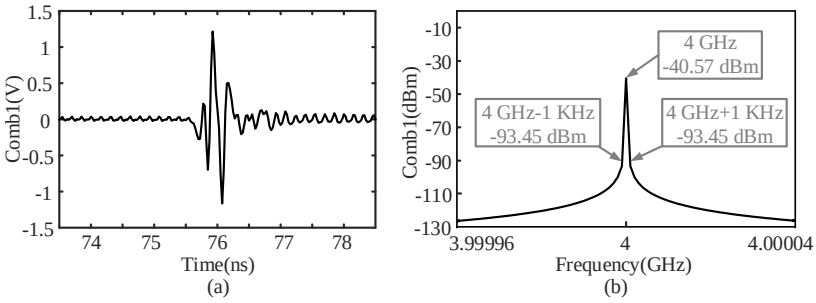

Figure 2.73: (a) One period of Comb1 in time-domain, (b) one tooth of Comb1 in frequency-domain calculated by taking FFT from Comb1. Reprinted with permission from [7].

teeth are spectrally resolved, and consequently each comb tooth pair provides a single independent spectral sample in the system output in BB. Since the fundamental resolution is set by the comb tooth linewidth, there is minimal cross talk between adjacent spectral elements. In free-running combs, the relative microwave line-width between the combs is greater than Δf_r. In that case, there can be varying degrees of overlap or blending with the corresponding RF comb which results in low frequency resolution [42].

Spectroscopy in TD relies on averaging the output signal to increase the SNR. One period of the DCS system output is 1 ms and averaging such signal can be a lengthy process. In this system, windowing in TD can result in smoothing in FD as will be discussed later. Therefore, the TD signal can be multiplied by a rectangular window. For that, instead of actual windowing, only a small part of the output signal is physically captured by the oscilloscope. In fact, the point where the maximum amplitude of the output occurs and 4 samples before and after that point are captured. The effective windowing procedure and TD output signal sample selection is a trade-off between (i) the system sensitivity and (ii) the averaging time and the system calibration accuracy. The less number of samples in TD (a shorter TD window) results in the smaller range for the change of ΔMag and $\Delta\phi$ values of different MUTs (less sensitivity). This can be seen in Fig. 2.74(a) where ΔMag and $\Delta\phi$ values are shown for ethanol and methanol with only 5 sampling numbers. Comparing Fig. 2.74(a) with the full-wave simulations (Fig. 2.67) and the VNA measurement (Fig. 2.68) results, the ΔMag and $\Delta\phi$ values change in a smaller range especially for $\Delta\phi$ which

is less than 3° in the worst case between ethanol and methanol while for the VNA it is 29.1°. Also the larger the number of samples in TD (the larger TD window) results in the longer averaging time, and also the ΔMag and $\Delta\phi$ spectrum will not appear monotonic while changing the MUTs (Fig. 2.74(c)). Such spectrum will increase the complexity of system calibration, where ϵ' and ϵ'' of MUTs must be described as functions of ΔMag and $\Delta\phi$, as will be discussed in Section 2.2.2.4. Therefore 9 samples in TD is chosen as a reasonable trade-off between sensitivity and averaging time and calibration accuracy. In this case, the difference in $\Delta\phi$ values between ethanol and methanol in the worst case is 12.2°. Fig. 2.74(b) shows ΔMag and $\Delta\phi$ for only 9 samples. The DCS system output in TD with 9 samples is shown in Fig. 2.75 averaged 4096 times. The FFT of Fig. 2.75 inside a 1 ms rectangular window is shown in Fig. 2.76. As can be seen, it results in a smooth magnitude (and phase) in FD compared with Fig. 2.72(c). Only one period of the windowed TD signal is used in taking FFT. Therefore, the FD result that is shown in Fig. 2.76 is not a sampled spectrum by comb lines.

As suggested, the output sample with the maximum amplitude and 4 samples before and after that in TD, can be used for measuring the magnitude response of the DCS system in FD. However, such duration may cause ambiguity in phase response in FD. Because different MUTs insert different delays on the incoming signal, recording the phase response of the MUTs requires the output signal always be captured at a unique time reference. Therefore, for the phase measurement, all outputs for different MUTs are captured at common start time and also common stop time as shown in Fig. 2.77(b). For this purpose, the air test start (2.08 μs) and stop (2.98 μs) times are considered as the reference. From Fig. 2.77, it can be seen that both amplitude and delay of the 9 samples change by different MUTs. This direction has been also observed in Fig. 2.74 about magnitude and phase in FD.

In experiment, the output signal is sampled at only discrete sampling positions in TD, and the zero point is not always located at such a position which can be one source of error in phase results. By applying complex Fourier transform, the delay δ relative to actual origin leads to the occurrence of imaginary part in spectrum by a phase $e^{j\omega\delta}$ [49]. Because the sampling rate is 1 GSps and the

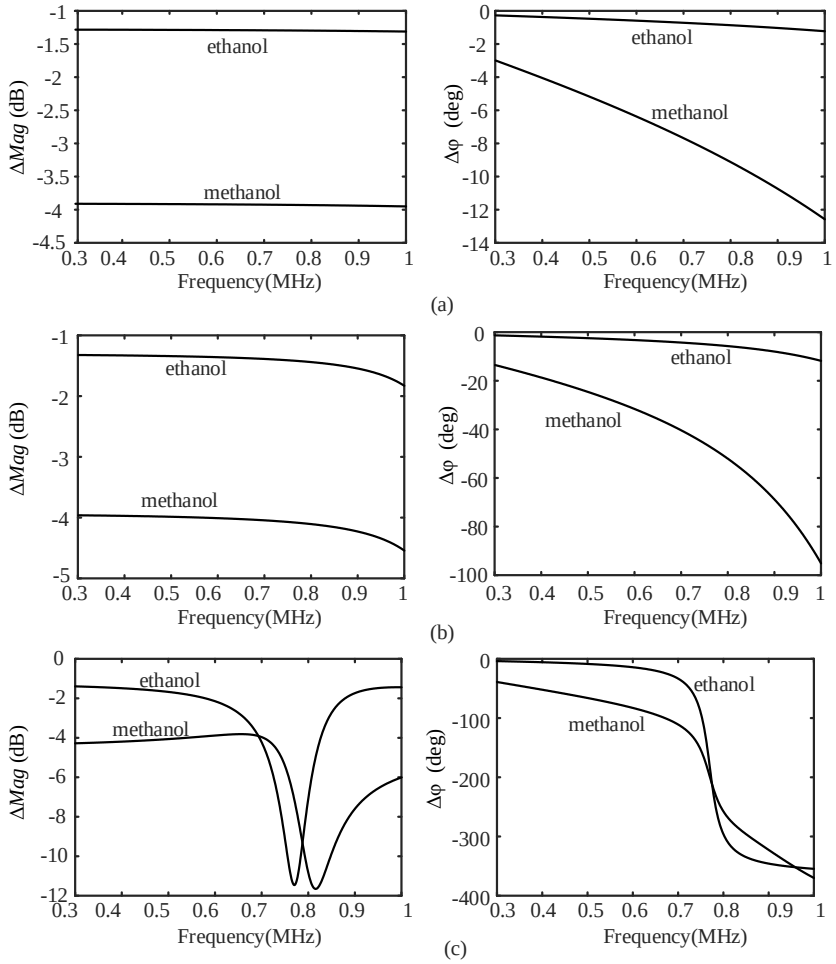

Figure 2.74: ΔMag and $\Delta\phi$ for ethanol and methanol while only (a) 5, (b) 9, and (c) 15 samples of the output signal are selected in time domain. Reprinted with permission from [7].

maximum BB frequency is 1 MHz, maximum error in phase would be $\phi = \omega\delta$ = 0.36 degrees. Due to its small value, such error has been ignored. Beside this, the parameter that is being used in material characterization is $\Delta\phi$ which is phase difference between MUT-test and air-test. Such difference also reduces the errors related to the phase. One method for real-time compensation of phase error has been presented in [50]. In this method, the data acquisition unit is automatically triggered by a beat note originated from two individual lines of the combs. Another method is to use a differential structure by employing two paths with identical sensors [51]. One sensor is empty representing air and the other one is filled by MUT. The value of $\Delta\phi$ is measured from the

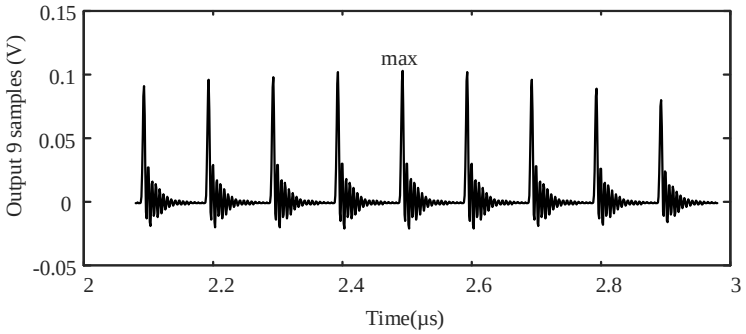

Figure 2.75: 9 samples of the DCS system output in time domain. Reprinted with permission from [7].

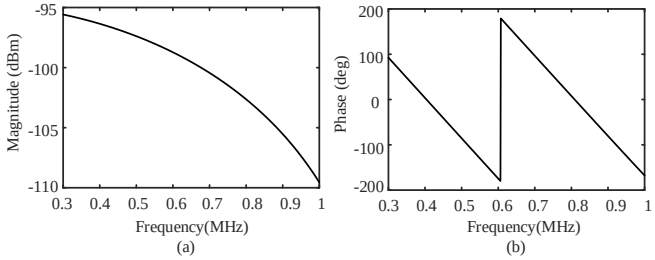

Figure 2.76: Frequency domain representation of 9 samples of DCS system output in a 1 ms window, (a) Magnitude and (b) Phase for MUT air. Reprinted with permission from [7].

phase differences in the outputs of the two sensors. Therefore, common errors between the two paths are cancelled through differentiation.

2.3.2.4 Calibration and Unknown MUT Characterization

The DCS system in this work has been primarily designed for characterization of liquid MUTs. Because of the difference in complex permittivity of different MUTs, the system magnitude and phase responses, ΔMag and $\Delta\phi$, vary by changing the MUTs. The aim of system calibration is to construct a relationship between the complex permittivity, ϵ^* = ϵ' - j ϵ'', and the measured ΔMag and $\Delta\phi$ of the MUTs. For this purpose, ΔMag and $\Delta\phi$ of 13 reference MUTs with known complex permittivities are measured and a polynomial equation is used to estimate the relationship between ϵ' and the measured $\Delta Mag - \Delta\phi$ pairs and another polynomial to estimate the relationship

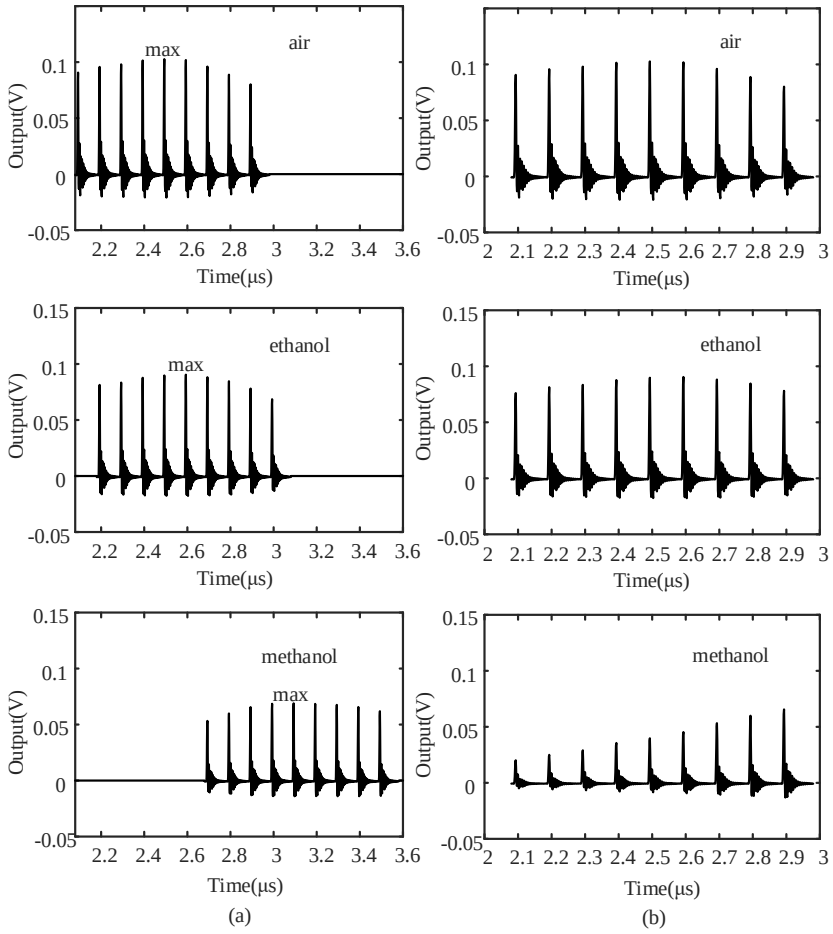

Figure 2.77: Selected samples for calculation of (a) ΔMag and (b) $\Delta\phi$. Reprinted with permission from [7].

between ϵ'' and the measured $\Delta Mag - \Delta\phi$ pairs, as follows:

$$\begin{aligned}\epsilon'(\Delta\phi, \Delta Mag) = p_{00} \ + \ p_{10} * \Delta\phi \ + \ p_{01} * \Delta Mag \ + \\ p_{20} * (\Delta\phi)^2 \ + \ p_{11} * \Delta\phi * \Delta Mag \ + \\ p_{30} * (\Delta\phi)^3 \ + \ p_{21} * (\Delta\phi)^2 * \Delta Mag,\end{aligned} \tag{2.14}$$

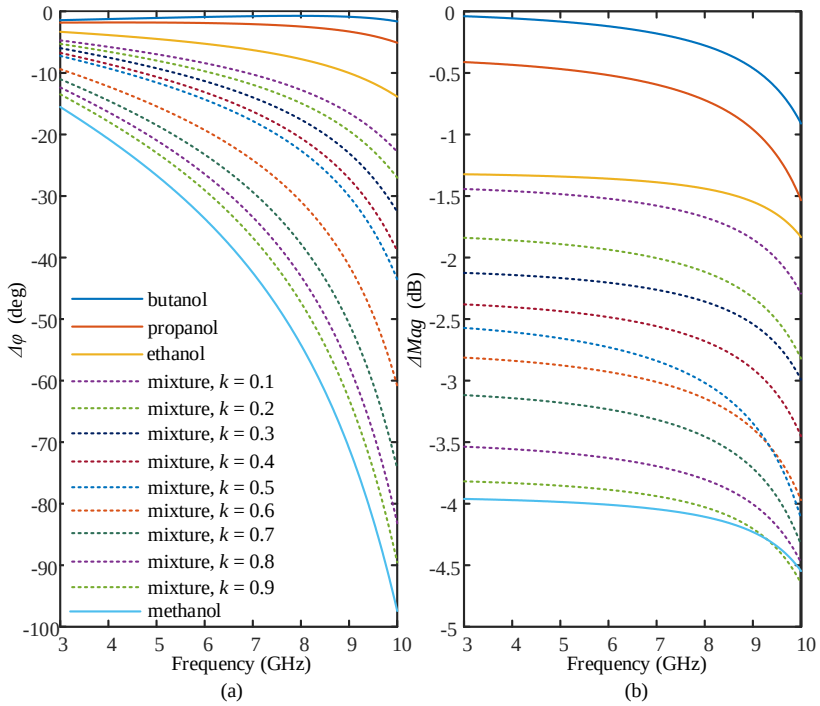

Figure 2.78: (a) $\Delta\phi$ and (b) ΔMag of the reference MUTs. Reprinted with permission from [7].

$$\begin{aligned}\epsilon''(\Delta\phi, \Delta Mag) = q_{00} \ + \ q_{10} * \Delta Mag \ + \ q_{01} * \Delta\phi \ + \\ q_{20} * (\Delta Mag)^2 \ + \ q_{11} * \Delta Mag * \Delta\phi \ + \\ q_{30} * (\Delta Mag)^3 \ + \ q_{21} * (\Delta Mag)^2 * \Delta\phi.\end{aligned} \tag{2.15}$$

Equation (2.14) suggests a third order dependency of ϵ' to $\Delta\phi$ and a first order dependency of ϵ' to ΔMag while (2.15) suggests a third order dependency of ϵ'' to ΔMag and a first order dependency of ϵ'' to $\Delta\phi$. As mentioned before, choosing a large number of samples from the output signal in TD could result in more complexity in calibration process. It means that the polynomials in (2.14) and (2.15) would have higher orders, thereby more number of reference MUTs were required to determine a large number of unknown calibration coefficients.

The measurement results of 13 different reference MUTs are shown in Fig. 2.78. The reference MUTs include butanol (C4H10O), propanol (C3H8O), ethanol (C2H6O), methanol (CH4O), and 9

mixtures of ethanol-methanol with mixing ratios $k = \frac{V_{methanol}}{V_{total}}$ = 0.1, 0.2, 0.3, 0.4, 0.5, 0.6, 0.7, 0.8, 0.9. The ΔMag and $\Delta\phi$ in Fig. 2.78 have been calculated by taking the fast Fourier transform (FFT) of the measured output signals after necessary windowing as discussed before. The curves in Fig. 2.78 are the average of 5 times measurements of reference MUTs. Fig. 2.79 shows the ϵ' and ϵ'' of reference MUTs derived from (2.14) and (2.15) through curve-fitting. As can be seen, such curve-fitting accurately approximates the theoretical values [52]. In average, the relative error between approximation and theory, $|\frac{\epsilon'_{theory}-\epsilon'_{calc}}{\epsilon'_{theory}}|$, is less than 0.013 in ϵ' and less than 0.039 in ϵ'' over the total frequency range. For the mixtures, the widely used Maxwell Garnett mixing rule [53] is employed as following:

$$\epsilon^*_{mixture} = \epsilon^*_e + 3k\epsilon^*_e \frac{\epsilon^*_m - \epsilon^*_e}{\epsilon^*_m + 2\epsilon^*_e - k(\epsilon^*_m - \epsilon^*_e)}. \tag{2.16}$$

where $\epsilon^*_{mixture}$, ϵ^*_e, and ϵ^*_m are the complex permittivities of mixture, ethanol, and methanol, respectively. The frequency dependent coefficients in (2.14) and (2.15) are shown in Fig. 2.80. The coefficient values are the outputs of curve-fitting type $poly31$ through fit function in MATLAB.

The behavior of system has been described by (2.14) and (2.15) up to this point. Providing that the system setup remains unchanged, the above-mentioned calibration procedure is only required once for the system and such system description is sufficient to characterize unknown MUTs with ϵ' and ϵ'' within ranges [1, 20] and [0, 14], respectively. In other words, by measuring ΔMag and $\Delta\phi$ of an unknown MUT and then substituting them into (2.14) and (2.15), ϵ' and ϵ'' of the unknown MUT can be calculated.

To demonstrate the ability of the system in characterizing unknown MUTs, the system output for 6 different ethanol-methanol mixtures with k = 0.05, 0.18, 0.45, 0.55, 0.77, and 0.95 are measured 5 times and their ΔMag and $\Delta\phi$ are calculated and plugged into (2.14) and (2.15). Fig. 2.81 shows the estimated ϵ' and ϵ'' with the standard deviation values. Although this set of mixtures are considered unknown for the system, the theoretical values of ϵ' and ϵ'' can still be calculated by (2.16). The values from theory are also plotted in Fig. 2.81 for the comparison. It appears that the

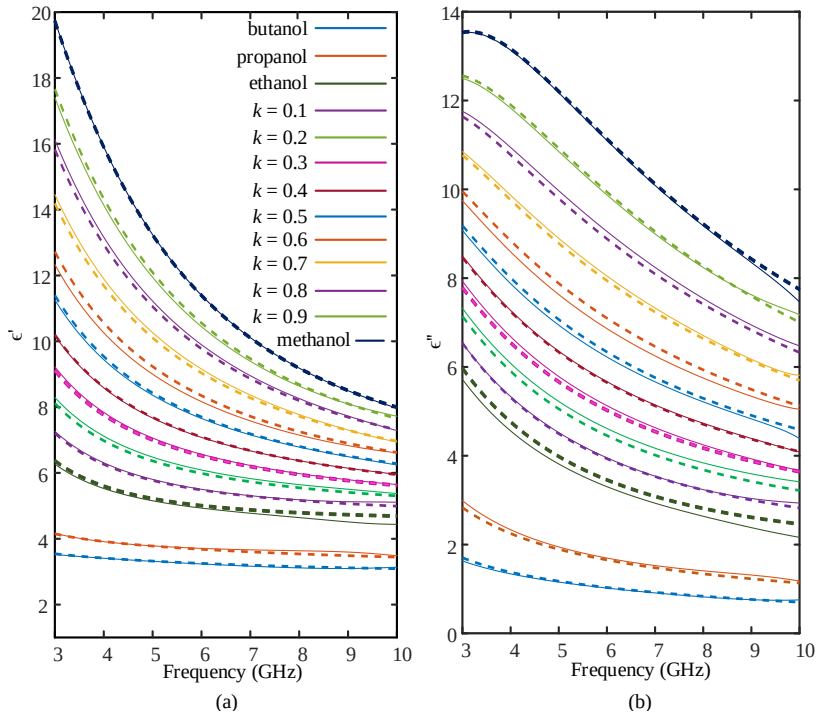

Figure 2.79: (a) ϵ' and (b) ϵ'' of the reference MUTs used to construct the behaivioral model of the DCS system. Solid lines: approximated by polynomials, dashed lines: theory. Reprinted with permission from [7].

estimated ϵ' and ϵ'' are in a good agreement with theory.

To quantify error in characterization of unknown MUTs, the calculated values from system measurements and the theoretical values are compared in Fig. 2.82. Fig. 2.82(a) shows $\epsilon'_{calc} - \epsilon'_{theory}$ values and Fig. 2.82(b) shows $\epsilon''_{calc} - \epsilon''_{theory}$ values for 5 times measurements of the unknown MUTs. The error for each unknown MUT is compared with $\pm|\epsilon^*_{theory}| = \pm\sqrt{(\epsilon'_{theory})^2 + (\epsilon''_{theory})^2}$ [39]. From Fig. 2.82(a) and (b), it can be concluded that error in estimating ϵ' is always less than $0.055|\epsilon^*|$ and error in estimating ϵ'' is also always less than $0.055|\epsilon^*|$.

Table 2.3 compares the proposed DCS system with two other state-of-the-art dielectric spectroscopy systems: the commercially available product Keysight N1501A dielectric performance probe kit [39] and the TDS system reported in [5]. In N1501A, the measurements are made by immersing a probe into MUTs to measure the reflection wave from the MUT while in the TDS and DCS systems the measurements are made by dropping MUTs on a sensing area and measuring

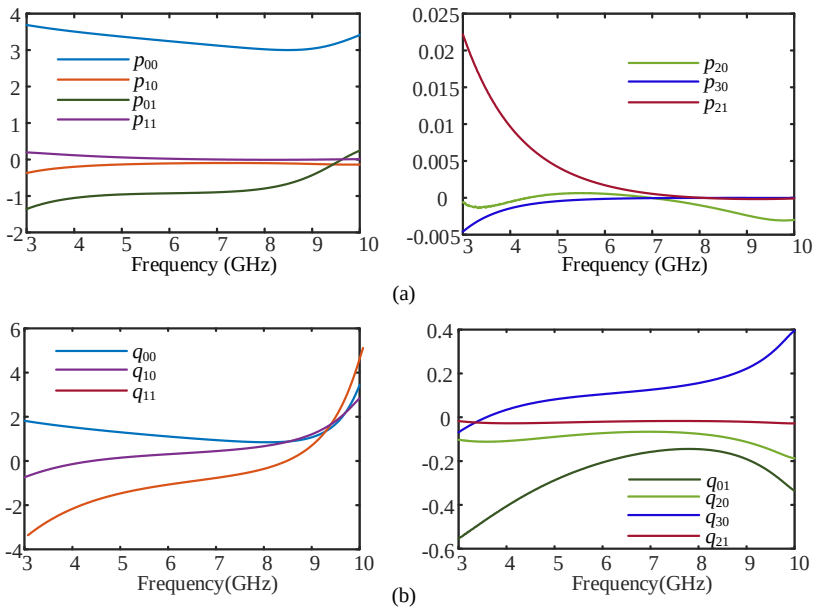

Figure 2.80: Coefficients for (a) ϵ' and (b) ϵ'' polynomials. Reprinted with permission from [7].

transmission wave from the MUT. The N1501A is based on FD measurement technique by using a network or impedance analyzer and the TDS system is based on TD measurement technique which requires using a high-frequency oscilloscope. However, the TD technique in the DCS system is based on mapping microwave properties into BB and it only requires an inexpensive low-frequency oscilloscope for measurements which greatly reduces the costs of the system. The N1501A also depends on network or impedance analyzer for generating RF energy but the TDS and DCS systems only need low frequency function generators, an RF signal generator for generating a single 6.5 GHz LO signal, and a customized pulse-shaping circuit. It is worth mentioning that the number of function generators and pulse-shaping circuits is twice in DCS compared to the TDS, and DCS also uses the phase-locking network with an extra function generator for triggering oscilloscope. Limited to the Keysight analyzer and the probe used, the frequency range of N1501A system extends from 500 MHz to 50 GHz. In order to reach such bandwidth by a DCS system, a combined frequency-time-domain technique [2] can be used which also demands designing the sensor, mix-

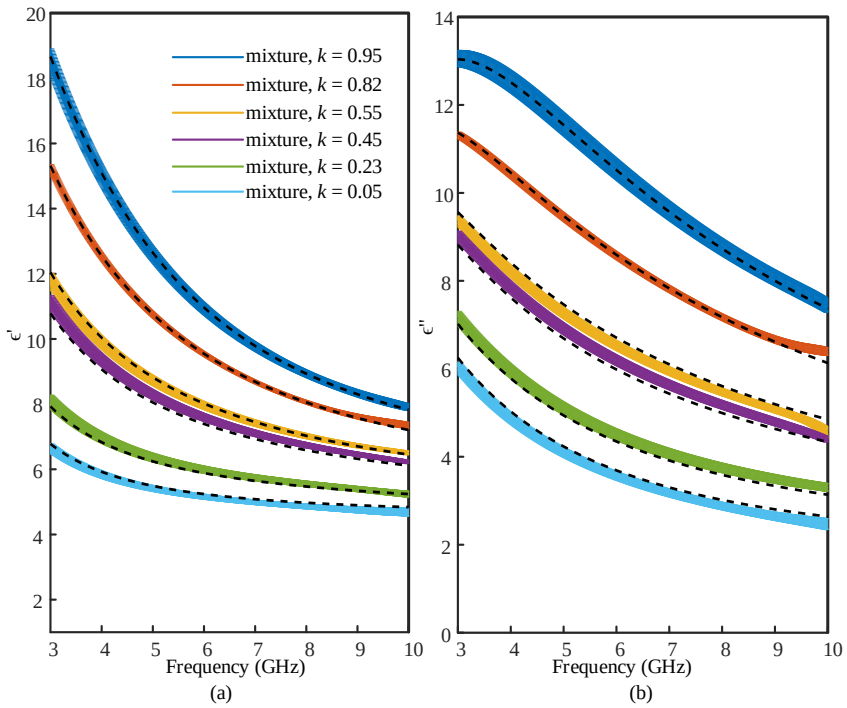

Figure 2.81: (a) ϵ' and (b) ϵ'' of unknown MUTs estimated by the behavioral model of the DCS system. Colored lines: estimated by polynomials, dashed lines: theory. Reprinted with permission from [7].

ers, and amplifiers for higher frequencies. Although the MUT size in the proposed system is larger than the other systems, using a miniaturized sensor as in [5] can decrease the MUT volume. Regarding the system accuracy, with comparable resolution and averaging time, maximum errors are $0.05|\epsilon^*|$, $0.1|\epsilon^*|$, and $0.055|\epsilon^*|$ in ϵ' and are $0.1|\epsilon^*|$, $0.1|\epsilon^*|$, and $0.055|\epsilon^*|$ in ϵ'' in N1501A, TDS, and DCS systems, respectively. In the proposed DCS system, the error in ϵ' is comparable with and in ϵ'' is less than the other two systems. In terms of the dynamic range, both N1501A and TDS systems outperform the DCS system. Because the focus of this work has been characterization of MUTs with permittivities in the range of ethanol-methanol permittivities, the dynamic range of the system is limited to the ϵ' of methanol (less than 20) and $\tan\delta$ of butanol (higher than 0.22). To improve the dynamic range, it will be necessary to design a sensor that meets matching condition and sensitivity in a higher dynamic range [5].

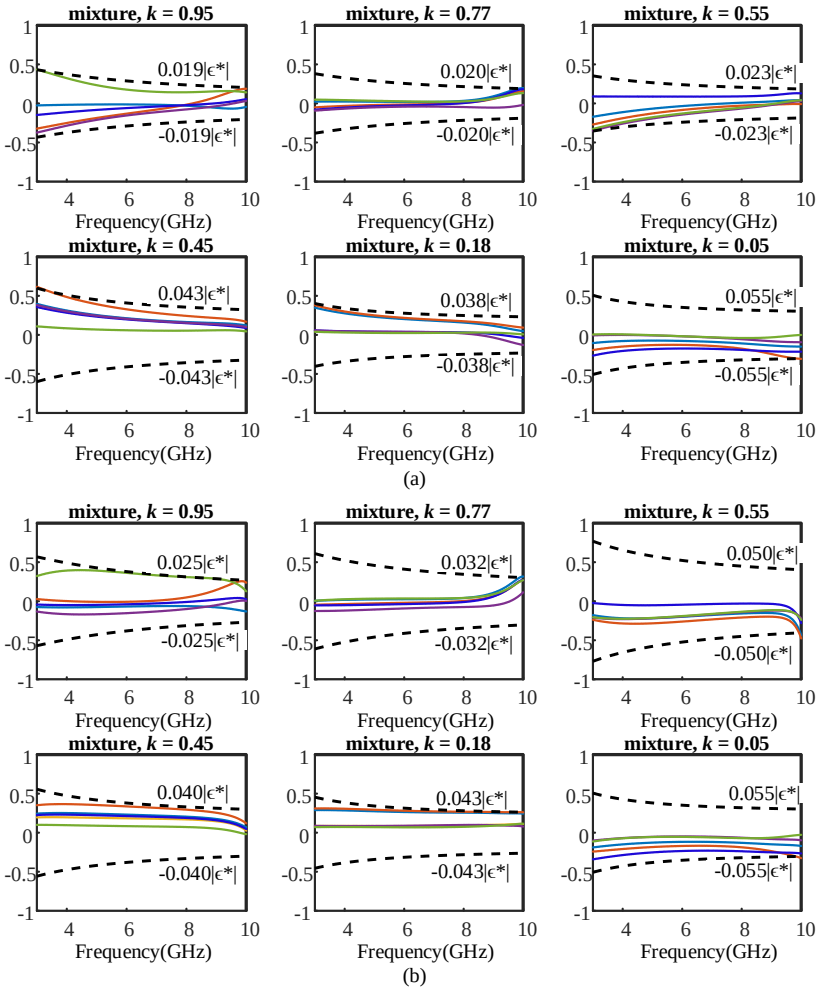

Figure 2.82: Error in calculating (a) ϵ' and (b) ϵ'' of unknown MUTs. Reprinted with permission from [7].

2.3.2.5 Conclusion

A miniaturized UWB microwave dual-comb spectroscopy system has been implemented in this paper. The conceptual operation of the DCS system along with the phase-locking network to enable phase measurements, has been discussed. Two UWB comb generators based on SRD and short-circuited stubs, a microstrip sensor, a mixer, an LPF, an oscilloscope, and necessary external sources built the DCS system. The behavior model of the system according to the measurement results of 13 reference MUTs has been constructed through calibration. Using the behavioral model, ϵ' and ϵ'' of 6 unknown MUTs have been estimated with errors of less then $0.055|\epsilon^*|$.

Table 2.1: Summary of system properties and comparison with related works. Adapted with permission from [1].

Ref.	Sensor Type	Freq. Range (GHz)	Setup Size	MUT size	Application & Detection Capability	Meas. Technique	Error
[15]	horn lens antennas (far-field)	14.5 - 17.5	33445 cm^2	316 cm^2	ϵ' and $\tan\delta$ of solids (material characterization)	FD	$\pm$ 0.35 and $\pm$ 2° in S11
[16]	quasi-TEM horn antennas (far-field)	0.5 - 6 (tunable in UWB range)	NR (significantly bulky antennas)	NA	ϵ' and thickness of solids (ground penetrating radar, and sub-surface sensing)	TD	1 inch thickness resolution
[17]	leaky lens antennas (far-field)	30 - 100	1200 cm^2	30 cm wide, height NR	ϵ' and ϵ'' of solids (material characterization)	TD	NR
[18]	Horn antennas (far-field)	26.5 - 40	900 cm^2	50×50×3 cm^3	ϵ', ϵ'', and thickness of solids (material characterization)	TD	error is reported as $\lvert\frac{\Delta\epsilon}{\epsilon}\rvert_{max}$ = 3.2%
This Work	Vivaldi antennas (radiative near-field)	3 - 10	62.4 cm^2	5.1×5.1×2 cm^3	ϵ' and ϵ'' of liquids (material characterization)	TD	1.92% for ϵ' and 3.84% for ϵ''

Table 2.2: Comparison of the proposed system with Keysight N1501A dielectric probe kit. Adapted with permission from [5].

Spectroscopy systems	Keysight N1501A dielectric probe kit	This work
Frequency range	500MHz-50GHz[1]	3.28GHz-10GHz
RF energy meas.	Network/impedance analyzer	Oscilloscope
Meas. technique	FD	TD
RF energy gen.	Network/impedance analyzer	33250A func. gen. + RF pulse gen.
Meas. procedure	Immersing probe inside MUT	Dropping MUT inside container
MUT type	Liquid, semi-liquid, flat solid	Liquid[2]
MUT size	At least 15.7μL[3]	0.3μL
Dynamic range	ϵ'<100, $tan\delta$>0.05	ϵ'<80, $tan\delta$>0.22[4]
Accuracy	ϵ':$\epsilon'\pm0.05\|\epsilon^*\|$, ϵ'':$\epsilon''\pm0.1\|\epsilon^*\|$	ϵ':$\epsilon'\pm0.1\|\epsilon^*\|$, ϵ'':$\epsilon''\pm0.1\|\epsilon^*\|$

[1] Limited to the Keysight analyzer and probe used.
[2] Requires adjusting MUT size to measure solids.
[3] Minimum h=5mm insertion and r=1mm around tip; thus, the minimum volume of MUT around tip is $V = \pi r^2 h$=15.7mm^3=15.7μL.
[4] $tan\delta$>0.02 based on simulations.

Table 2.3: Comparison of the proposed dual-comb spectroscopy system with Keysight N1501A dielectric performance probe and time-domain spectroscopy system. Adapted with permission from [7].

Spectroscopy systems	Keysight N1501A dielectric probe kit [39]	Time-domain spectroscopy [5]	Dual-comb spectroscopy (This work)
Frequency range	0.5–50 GHz	3–10 GHz	3–10 GHz
RF energy meas.	Network/impedance analyzer	High-frequency oscilloscope	Low-frequency oscilloscope
Measurement technique	Frequency domain	Time domain	Time domain
RF energy gen.	Network/impedance analyzer	33250A function gen., E8267D signal gen., pulse shaping circuit	DG4162 and 33250A function generators, E8267D signal gen., pulse shaping circuit
Measurement procedure	Immersing probe inside MUT	Dropping MUT inside container	Dropping MUT inside container
MUT type	Liquid, semi-liquid, flat surface solid	Liquid	Liquid
MUT size	At least 15.7 μL	0.3 μL	0.7 mL
Dynamic range	$\epsilon'<100$, $\tan\delta>0.05$	$\epsilon'<80$, $\tan\delta>0.22$	$\epsilon'<20$, $\tan\delta>0.22$
Accuracy	ϵ':$\epsilon'\pm0.05\|\epsilon^*\|$, ϵ'':$\epsilon''\pm0.1\|\epsilon^*\|$	ϵ':$\epsilon'\pm0.1\|\epsilon^*\|$, ϵ'':$\epsilon''\pm0.1\|\epsilon^*\|$	ϵ':$\epsilon'\pm0.055\|\epsilon^*\|$, ϵ'':$\epsilon''\pm0.055\|\epsilon^*\|$

3. CHIPLESS RFID *

3.1 Retransmission-Based Chipless RFID Tag

3.1.1 Introduction

A chipless radio frequency identification (RFID) tag has a particular RF response to an incident electromagnetic wave. Chipless RFID is a low-cost and highly reliable solution for identification, tracking and sensing applications [54].

In a retransmission-based chipless RFID tag, an incident electromagnetic wave is received by an RX antenna, travels through an encoding structure, and then transmitted through a TX antenna while RX and TX antennas are usually cross-polarized for higher isolation [55, 56, 57]. In [55], a 35-bit chipless RFID tag with a microstrip multiresonator circuit is introduced where 35 spirals next to the microstrip line generate 35 separate resonances from 3.3 GHz to 7 GHz. Authors in [56] present an 8-bit chipless RFID tag with 8 open-stub resonators connected to a microstrip transmission line operating from 2.08 GHz to 4.03 GHz. In [57], a first and a second order chipless RFID tag are proposed by connecting quarter-wavelength open-stubs to a microstrip line based on filter theory. Two examples of 5-bit tags operating from 2.5 GHz to 2.9 GHz are demonstrated in [57]. All aforementioned tags are passive, planar, printable, (potentially) high capacity and they use resonance frequency position as a single dimension of coding.

In this work, a high capacity 50.7-bit retransmission-based chipless RFID tag with miniaturized resonators is presented. 32 resonators each consisting of an interdigital capacitor (IDC) in parallel with a meander inductor build miniaturized LC resonators [58] placed next to a microstrip line. Beside 32 resonance positions designed from 3.4 GHz to 10 GHz, Q of each resonator is also coded in two separate states by adjusting the LC distance from the microstrip line. Therefore, each frequency position has three states: (i) no resonance, (ii) low Q, and (iii) high Q that generates 50.7 bits for the tag. To the best of author's knowledge, this work has the highest overall number of bits

* Reza Ebrahimi Ghiri and Kamran Entesari, "A 50.7-Bit Retransmission-Based Chipless RFID Tag With Miniaturized Resonators," 2021 IEEE Topical Conference on Wireless Sensors and Sensor Networks (WiSNeT).

and the largest area efficiency among all retransmission-based chipless RFID tags in literature.

3.1.2 Tag Design

The proposed miniaturized resonance unit for application in retransmissions-based chipless RFID tags is shown in Fig. 3.1(a). This resonance unit consists of an IDC in parallel with a meander line (Fig. 3.1(b)) printed next to a microstrip transmission line. The frequency response of the resonance unit on RO4350B substrate with thickness = 0.338 mm, ϵ_r = 3.66, and tanδ = 0.0031, while d = 0.15 mm, W_{line} = 0.76 mm, W = G = W_t = G_e = 0.15 mm, L = 0.5 mm, and D = 3.15 mm, is shown in Fig. 3.1(c). The minimum line widths and spacings are designed to be 0.15 mm to avoid extra cost on fabrication. According to Fig. 3.1(c), the transmission response, S_{21}, shows a resonance at 3.4 GHz and a second resonance at 10.5 GHz. The first resonance is the result of combination of capacitive and inductive properties of the LC circuit next to the microstrip line. The second resonance is the result of self-resonance of the IDC. Therefore, the frequency range from 3.4 GHz to 10.5 GHz can be used for designing multiple resonators while the resonator with D = 3.15 mm and 9 IDC fingers generates the lowest resonance frequency. The length D and the number of IDC fingers (N_f) are used as two parameters to adjust the position of resonance frequency. Fig. 3.2 shows the effect of D and N_f in the resonance location.

In addition to the resonance position, the Q of the resonators can also be added to the coding capability as the second dimension. The Q of resonance response varies by changing the distance (d) of resonator from the microstrip top trace as shown in Fig. 3.3 for d = 0.15, 0.3, and 0.45 mm for two different resonance positions. Consequently, three states can be considered for each frequency position: (i) low Q resonance, (ii) high Q resonance, and (iii) no resonance. As a result, each resonance position can convey $log_2 3$ = 1.585 bits.

A high capacity tag with 50.7 bits can be achieved by employing 32 resonators. Fig. 3.4 shows the simulated frequency response of 32 resonators with ADS momentum. In the simulations, all resonators operate either in high Q or in low Q modes. In the high Q mode, d = 0.15 mm and in the low Q mode d = 0.12 mm. With such selection of d, the difference in S_{21} amplitudes of low Q and high Q resonators is at least 2.5 dB at resonance frequency. In the first 11 resonators, N_f = 9 while

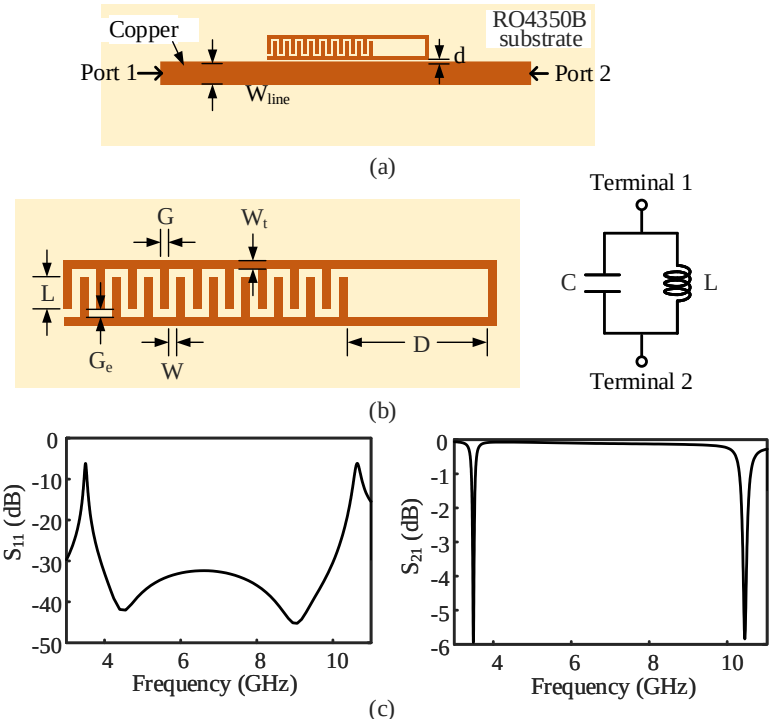

Figure 3.1: (a) The proposed resonance unit with an interdigital capacitor in parallel with a meander line, (b) Lumped LC section layout and its equivalent circuit, d = 0.15 mm, W_{line} = 0.76 mm, W = G = W_t = G_e = 0.15 mm, L = 0.5 mm, and D = 3.15 mm (total size = 1.1 mm$\times$ 8.6 mm), (c) The simulated S_{11} and S_{21} of the resonance unit. Reprinted with permission from [8].

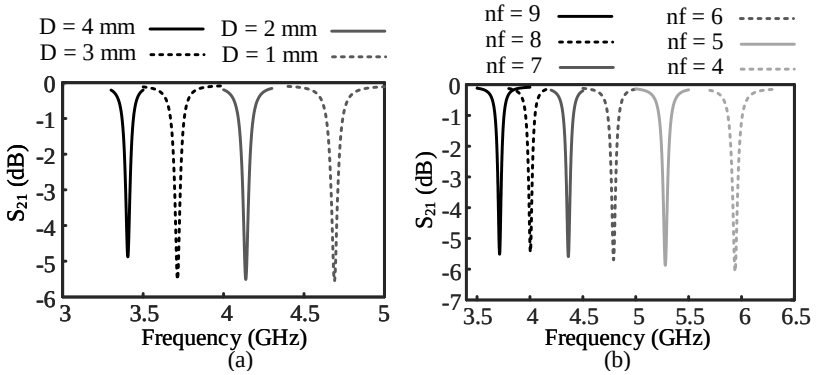

Figure 3.2: Effect of (a) length D on the resonance location (N_f = 9) and (b) N_f on the resonance location (D = 3 mm). Reprinted with permission from [8].

D varies in 11 different lengths and the rest of resonators use N_f = 4 and varying D in 21 different lengths. Table 3.1 shows the optimized values of D for all resonators. According to the simulation

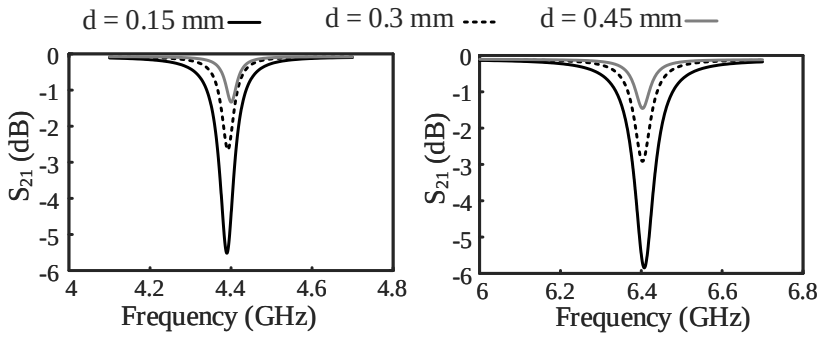

Figure 3.3: Effect of changing resonator distance from the microstrip line for two different resonance positions. Reprinted with permission from [8].

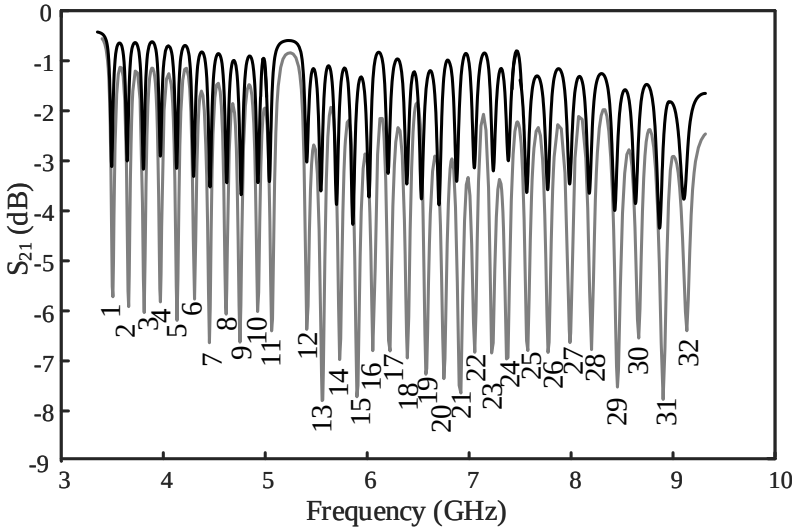

Figure 3.4: Simulated result of all high Q (d = 1.5 mm) and all low Q (d = 0.3 mm) multiresonators. Reprinted with permission from [8].

results in Fig. 3.4, the occupied bandwidth by all resonators is 6.1 GHz ranging from 3.4 GHz to 9.5 GHz.

3.1.3 Implementation Results and Discussions

The photograph of fabricated multiresonators and a sample retransmission-based tag are shown in Fig. 3.5. In this figure, four multiresonators including a multiresonator without any resonator

Table 3.1: D values in mm for LC resonators. N_f is 9 for resonators #1 to #11 and N_f is 4 for resonators #12 to #32. Reprinted with permission from [8].

#	1	2	3	4	5	6	7	8
D	3.15	2.72	2.34	1.98	1.65	1.35	1.1	0.84
#	9	10	11	12	13	14	15	16
D	64	41	23	3.45	3.25	3.05	2.85	2.67
#	17	18	19	20	21	22	23	24
D	2.49	2.31	2.16	2.01	1.88	1.75	1.63	1.52
#	25	26	27	28	29	30	31	32
D	1.4	1.27	1.14	1.02	0.91	0.81	0.71	0.61

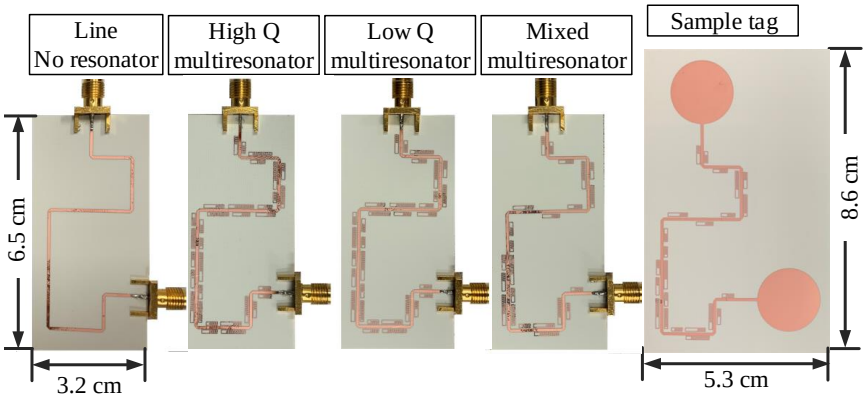

Figure 3.5: Photograph of fabricated multiresonators and a sample tag. Reprinted with permission from [8].

(only microstrip lines), an all high Q resonators, an all low Q resonators, and a mixed resonators are shown. The transmission responses of the multiresonators are shown in Fig. 3.6. This figure presents S_{21} values of all high Q and all low Q multiresonators. Fig. 3.6 is divided to 32 frequency bands where one low Q and one high Q resonance happens inside each band. The low Q and high Q resonances can be clearly distinguished from the difference in S_{21} amplitudes at resonance frequencies. For example, the difference in S_{21} of low Q and high Q resonances in band 1 is 3.1 dB while this difference can reach to 9 dB in band 21. Instead of the S_{21} valleys at resonance, the Q of resonators inside each band can be compared to distinguish between low Q and high Q resonances. The multiresonator response can be evaluated in terms of group delay as well. Fig.

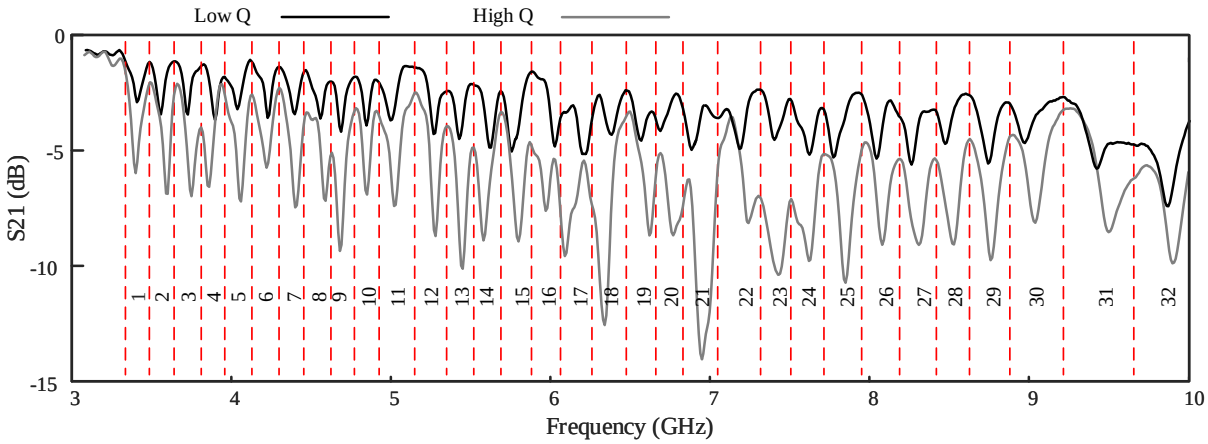

Figure 3.6: Measurement results of all high Q and all low Q multiresonators. Reprinted with permission from [8].

3.7 compares group delay response of all low Q and all high Q tags. As can be seen, the group delay of high Q resonances extends in a wider range compared to the low Q resonances for all 32 resonance positions. For example, for the first resonance, group delay extends from -0.243 ns to 1.33 ns for low Q resonator, while it extends from -1.6 ns to 1.55 ns for high Q resonator. The minimum value of group delay at each resonance can also be used for comparison.

Fig. 3.8 shows the S_{21} and group delay responses of a multiresonator consisting of a mix of high Q, low Q and no-resonator states. At any of the 32 frequency bands, the resonance is compared with the resonance response in Fig. 3.6. As an example, inside band 31, there is a resonance with the minimum value of -9.3 dB. When it is compared with the low Q valley (-5.7 dB) and high Q valley (-8.5 dB) inside band 31 in Fig. 3.6, it is closer to high Q response. Therefore, it is determined that there is a high Q resonance inside band 31. The same comparison is made inside each band as shown in Fig. 3.8.

Two fabricated tags with 9 high Q and low Q resonators are read by two 3164-05 open boundary quad-ridged horn antennas placed 30 cm far from the tag (Fig. 3.9) and connected to an N5227A network analyzer. The normalized S_{21} values of the tags are shown in Fig. 3.10. The normalized S_{21} values are calculated as follows: (i) Complex S_{21} response from the tag is subtracted from

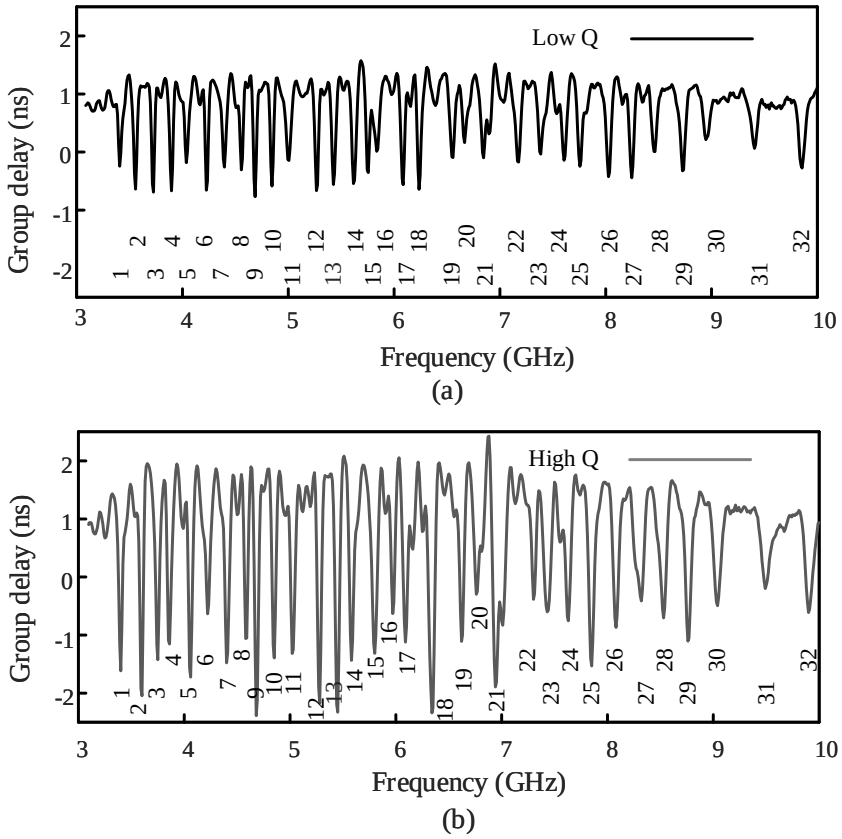

Figure 3.7: Group delay responses of multiresonators, (a) all low Q resonators, and (b) all high Q resonators. Reprinted with permission from [8].

complex S_{21} response from the tag with no resonances, (ii) the result from previous calculation is converted to time-domain through inverse fast Fourier transform (IFFT), (iii) the time-domain signal is windowed to removed the multiple reflections that occure in the reader excitation and inside the tag itself, (iv) the results from previous section is converted to frequency domain through FFT. As can be seen, the high Q and low Q responses are observed at all frequencies shown in Fig. 3.10.

Table 3.2 compares this work with some of the state-of-the-art retransmission-based tags in the literature. As can be seen, this tag outperforms other tags in terms of the total number of bits and the area efficiency. If the first 21 resonances from 3.4 GHz to 7 GHz are considered in computing the spectrum efficiency, the value of spectrum efficiency is 9.24 bit/GHz which is a higher value

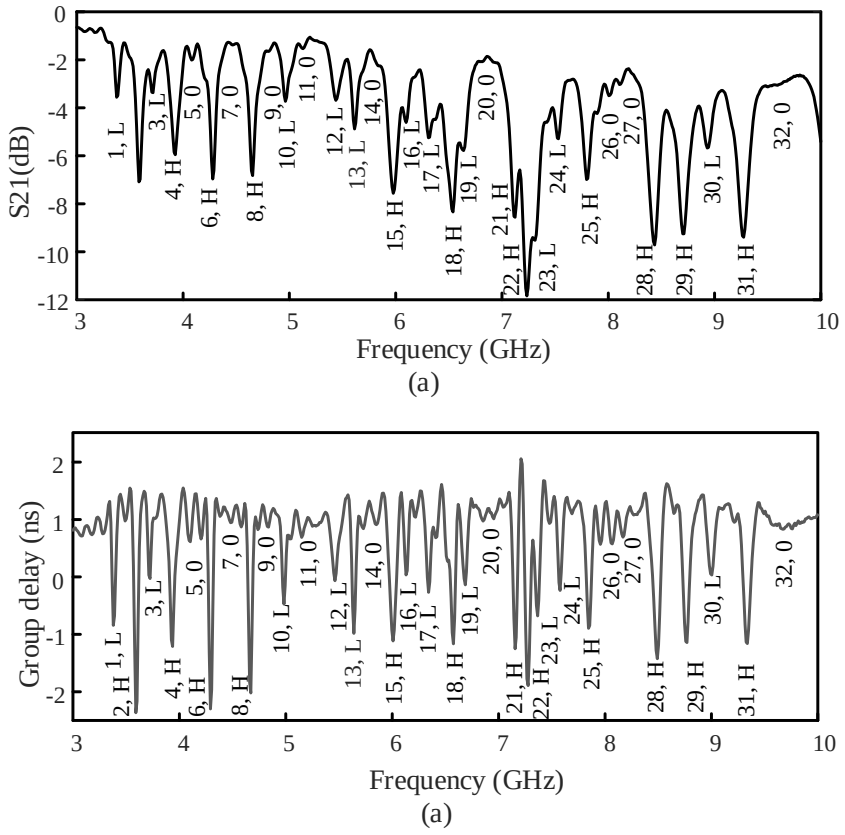

Figure 3.8: Frequency response of a mixed multiresonator, (a) S21 (dB), and (b) group delay. Reprinted with permission from [8].

compared with [55].

3.1.4 Conclusion

A retransmission-based chipless RFID tag operating from 3.4 to 10 GHz has been implemented in this work. The tag employs the resonance frequency position and the Q of the resonance as two dimensions. With 32 resonators, the tag achieves overall capacity of 50.7 bits.

Figure 3.9: Measurement setup and antennas. Reprinted with permission from [8].

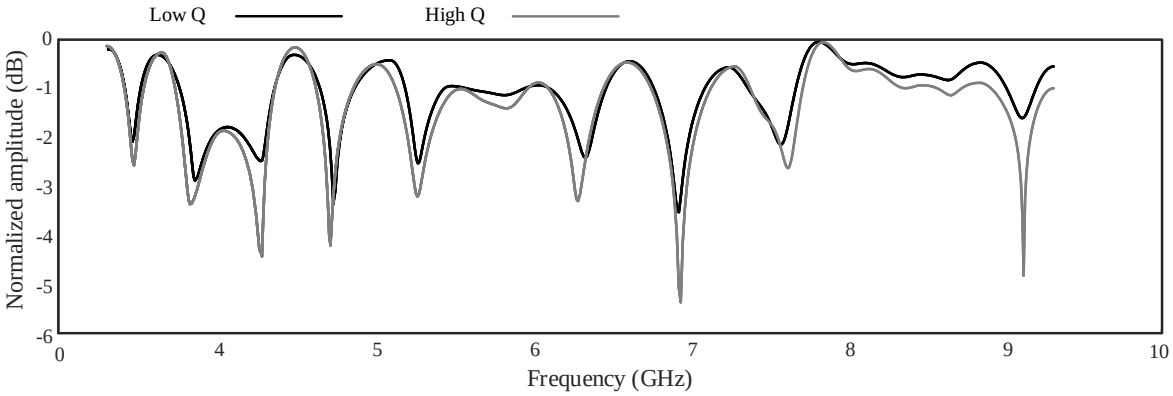

Figure 3.10: Measurement result of the tags. Reprinted with permission from [8].

Table 3.2: Table of Comparison. Reprinted with permission from [8].

	total bits	frequency range (GHz) [bit /GHz]	tag area (cm×cm) [bit /cm^2]	multiresonator area (cm×cm) [bit /cm^2]
[55]	35	3 -7 [8.75]	6.5×8.8 [0.61]	4.1×6.3 [56]
[3]	8	1.9- 4.5 [3.1]	6.6×8.6 [0.14]	2.5×3.0 [0.67]
[57]	5	2- 3 [5]	6.0×7.0 [0.12]	3.5×3.5 [0.41]
this work	50.7	3.4- 10 [7.68]	5.3×8.6 [1.11]	3.2×6.5 [2.43]

3.2 Time-domain Chipless RFID Readers

3.2.1 Introduction

Chipless RFID is a smart, robust, and low cost solution for identification and sensing. Chipless RFID tags are passive and printable electromagnetic structures that are considered as substitutes for traditional barcodes and as alternatives to chipped RFID tags. The chipless (/chipped) RFID shows its usefulness in a wide range of applications including item tracking, transportation, supply chain management, asset management, security and access control, and point-of-sales systems [59]. The development of miniaturized and high-capacity chipless RFID tags has attracted immense attention in the past decade [60, 61]. In addition to the tag, every chipless RFID system requires a microwave UWB reader to interrogate the tag by a UWB transmitter and then acquires the reflected response form the tag by a UWB receiver. Unlike the chipless RFID tags, there is limited research about UWB chipless RFID readers [62, 63, 64]. The focus of this section is comparison of time-domain UWB chipless RFID readers and proposing the dual-comb reader as a novel technique for Chiples RFID application.

In time-domain UWB chipless RFIDs systems, a transmitter emits a short duration pulse to excite a UWB chipless RFID tag, and a receiver acquires the reflected response from the tag at once. In this technique, all frequency signature of the tag is captured simultaneously, without the

need to sweep the excitation frequency. Therefore, time-domain technique is fast and simultaneous in nature. Transmission and reception of a short-duration pulse with the duration of hundreds of pico-seconds is the basis of impulse-radio (IR) UWB technique in time-domain [65].

For the chipless RFID tags that mostly have multiple resonances tightly located in the frequency spectrum, the frequency response of the tag with high resolution is of interest. As a result, time-to-frequency domain conversion is necessary to extract the frequency signature of the chipless RFID tags. Because of the short duration of the IR-UWB pulse, the frequency spectrum resulted through Fourier transformation will show a poor resolution such that the detection of resonance positions is impossible. To have a frequency resolution of MHz range by pure FFT, the length of time-domain signal must be in the order of μs range. Therefore, the response of the tag is needed to be observed in a μs duration. This makes the average power of the IR-UWB pulse extremely small especially in the receiver side in an open environment. Repeating multiple pulses within the μs range will increase the power level of the IR-UWB signal. In addition, averaging the received data is essential to improve the signal-to-noise ratio in the receiver. In practice, IR-UWB-based measurement can take the same amount of time compared to its frequency-domain counter-parts. The broadband chirped pulse Fourier transform microwave (CPFT-MW) [66, 67, 68] is a time-domain techniques that improves the speed that the total spectrum is collected. The CPFT-MW technique, enables collection of UWB microwave frequency with high resolution. In CPFT-MW technique, the broadband pulse is stretched in time to deliver sufficient power at each frequency. With a chirped pulse with the duration of μs order, the UWB microwave response of a chipless RFID tag can be acquired with high resolution, sufficient signal-to-noise ratio, and more quickly than with the IR-UWB method. For both IR-UWB and CPFT-MW techniques, there are numerous customized and low-cost UWB pulse generators [69, 70] in the transmitter. However, the acquisition of UWB pulses in the receiver is challenging due to the requirement for an ultra-high bandwidth and sampling rate analong-to-digital converter. The equivalent time sampling [71] and the filter bank [72] approach are two techniques that reduce the complexity of UWB receivers. In equivalent time sampling method, a broadband sample and hold unit collects all samples of a

periodic UWB input with a low sampling rate but in multiple periods. In filter bank approach, the input UWB signal is divided into multiple sub-bands with small bandwidths by band-pass filters (BPF) and thus each sub-band requires lower sampling rate to be successfully captured compared with the original UWB input. The time equivalent sampling and filter bank techniques have their own complexities in terms of jitter control and precise high-order filter requirements, respectively.

The dual-comb technique [43, 42, 48] is a time-domain technique that can significantly reduce the complexity of UWB Chipless RFID receivers. In this technique, the signal input to the receiver is at low frequency while it contains the UWB characteristics of the tag. The principal of dual-comb technique is based on multi-heterodyne detection of spectrum where two broadband periodic pulses with slightly different repetition rates are mixed to map the high frequency information of one of the periodic signals into low frequency baseband. Dual-comb properly fits into chipless RFID systems by offering high spectrum resolution and low complexity receiver. One of the periodic pulses, called frequency comb, interrogates the tag and the reflected comb that holds the signature of the tag is mixed with a second reference comb at receiver. The result includes a third comb mapped into the baseband frequency and also contains all signature of the UWB tag. As a result, the UWB information of the tag inside the third comb, can be captured by a low-speed oscilloscope with a low complexity. To the best of the author's knowledge, it is the first time that dual-comb technique is used for UWB chipless RFID reader.

For the demonstration of IR-UWB, CPFT-MW, and dual-comb technique as various time-domain chipless RFID systems, a 32 bit frequency coded chipless RFID tag is measured. The tag is retransmission-based and includes a transmission line with 32 miniaturized LC resonators located next to the line. Each LC resonator generates a resonance in the transmission response of the line. The tag operates in 3.5-9 GHz and the minimum distance of the resonances is 100 MHz at lower frequencies. This high-capacity chipless RFID tag is used to compare the time-domain systems in terms of detecting the frequency position of the resonances which appear in the amplitude response of the tag in frequency-domain.

3.2.2 System Design

Three time-domain UWB Chipless RFID systems based IR-UWB, CPFT-MW, and dual-comb time-domain techniques are explained in this section. The aim of these systems is capturing the tag signature with a frequency resolution of at least 10 MHz after converting the time-domain UWB signal to its equivalent frequency-domain signal through fast-Fourier transform (FFT) operation. With this frequency resolution, different resonances with the spacing in the order of 100 MHz in the tag can be easily captured.

3.2.2.1 Impulse-Radio UWB Technique

The block diagram of IR-UWB chipless RFID sysem is shown in Fig. 3.11. This system consists of an IR-UWB pulse generator, a UWB TX antenna, the tag, a UWB RX antenna, and a high-speed oscilloscope receiver. A single IR-UWB pulse has a short duration in a fraction of nanoseconds in time-domain thus has a low level power spectrum. In order to increase the signal-to-noise ratio for this system, repeating and averaging the received signal are necessary. Therefore, the IR-UWB signal is repeatedly sent to make the averaging possible. Fig. 3.12 shows an IR-UWB pulse with 1 V_{pp} amplitude with PRF = 10 MHz. The pulse used is a first-order Rayleigh pulse as given below:

$$f(t) = \frac{-2(t-1)}{a^2} e^{-(\frac{t-1}{a})^2}, \tag{3.1}$$

where a is a pulse parameter equal to 45×10^{-3} ns and t is time in nano-seconds. According to Fig. 3.12 (b), the power spectrum of the periodic IR-UWB signal has maximum of -52 dBm/MHz at frequency of 5 GHz while the power spectrum value for a single IR-UWB pulse is always less than -72 dBm/MHz.

The response of the multi-resonator to the IR-UWB excitation is shown in Fig. 3.13. Fig. 3.13 (a) shows the time-domain response in 1μs. As can be seen from the inset, the multi-resonator response includes a tail of ripples that holds the resonance information. The PRF of the IR-UWB pulse has been selected such that the ripples are diminished before the start of the next period. Fig.

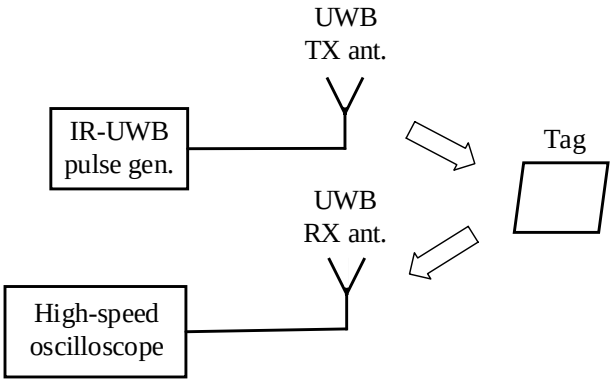

Figure 3.11: Block diagram of IR-UWB Chipless RFID system.

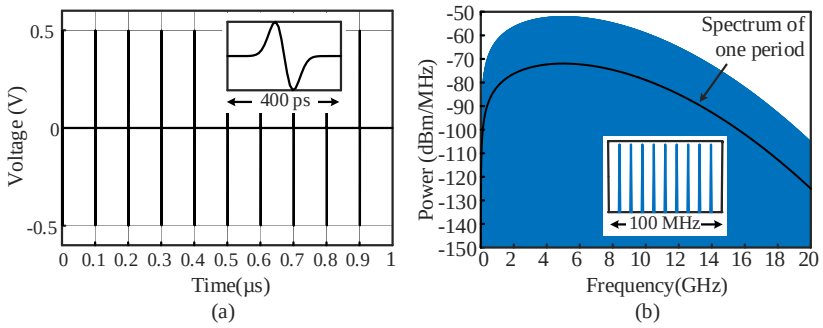

Figure 3.12: Periodic IR-UWB signal in (a) time-domain and (b) frequency-domain with a period of 0.1μs

3.13 (b) shows the multi-resonator response in frequency-domain. As shown, the transmission response of the multi-resonator is reflected in the spectrum in Fig. 3.13 (b).

3.2.2.2 Chirped Pulse Fourier Transform Microwave technique

The block diagram of chirped pulse Fourier transform microwave (CPFT-MW) chipless RFID system is shown in Fig. 3.14. This system consists of a chirped pulse generator, a UWB TX antenna, the tag, a UWB RX antenna, and a high-speed oscilloscope receiver. The duration of the chirp signal is 1 μs and it results in the frequency resolution of 1 MHz through FFT. Equation

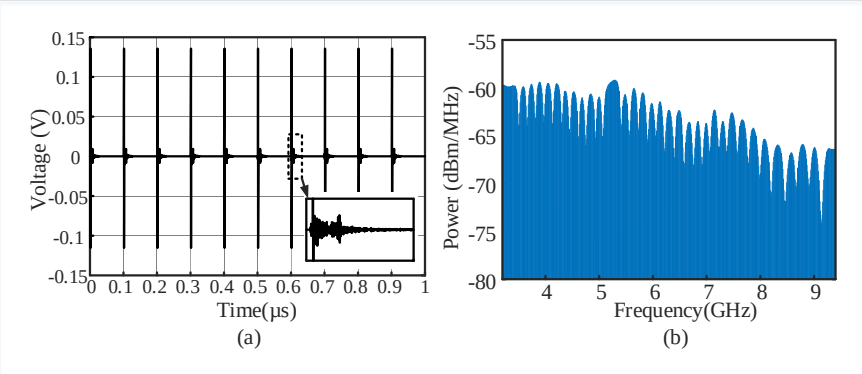

Figure 3.13: (a) Simulation results of response of multi-resonator in time-domain in 10 μs and (b) response of multi-resonator to the periodic UWB pulse excitation in frequency-domain.

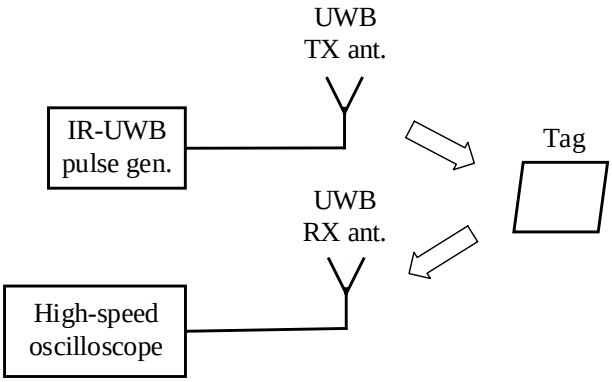

Figure 3.14: Block diagram of CPFT-MW UWB Chipless RFID system.

below used in generating the chirp signal:

$$f(t) = Acos(\frac{f_2 - f_1}{2T}t^2 + f_1 t), \tag{3.2}$$

where f_1 and f_2 are initial and target frequencies equal to 3 GHz and 10 GHz, respectively, T is the sweep time equal to 1 μs, and A is an amplitude constant. Fig. 3.15 shows the chirp signal and the multi-resonator response to that. Because the linear chirp signal has amplitude levels all over the duration of the signal, the power spectrum of one period of this signal can be reached to the same level of IR-UWB with sigmal amplitude of 0.06 V as shown in Fig. 3.15 (a) and (c). One

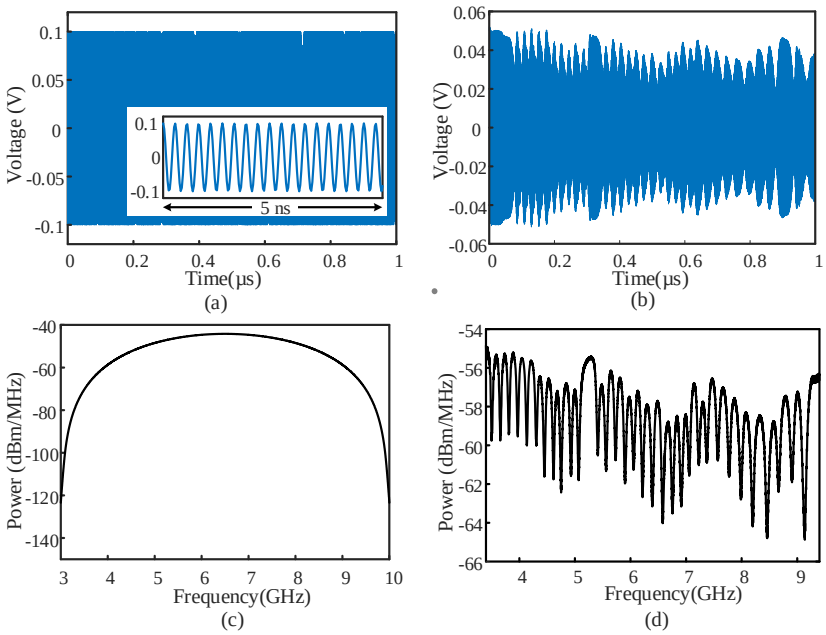

Figure 3.15: Simulation results of (a) input chirped pulse in time-domain, (b) chirped pulse response of the multi-resonator in time-domain, (c) input chirped pulse in frequency-domain, and (d) chirped pulse response of the multi-resonator in frequency-domain.

important practical advantage of chirped pulse with linear sweep is that its frequency bandwidth can be increased by an RF frequency multiplier without changing the pulse duration [66].

The multi-resonator responses to the chirp excitation are shown in Fig.s 3.15 (b) and (d) in time and frequency domains, respectively. As seen, the transmission response of the multi-resonator in Fig. 3.13 (c) is reflected in the power spectrum of the output in Fig. 3.15 (d). In conclusion, the averaging of the received signal by oscilloscope will take much shorter to achieve an acceptable SNR values in CPFT-MW compared to the IR-UWB approach.

3.2.2.3 Dual-Comb Technique

The block diagram of dual-comb UWB chipless RFID sysem is shown in Fig. 3.16. This system consists of two comb generators with slightly different repetition rates, a UWB TX antenna, the tag, a UWB RX antenna, a mixer, a low-pass filter (LPF), and a high-speed oscilloscope receiver. The two comb generators output UWB $Comb_1$ and $Comb_2$ with slightly different pulse repetition

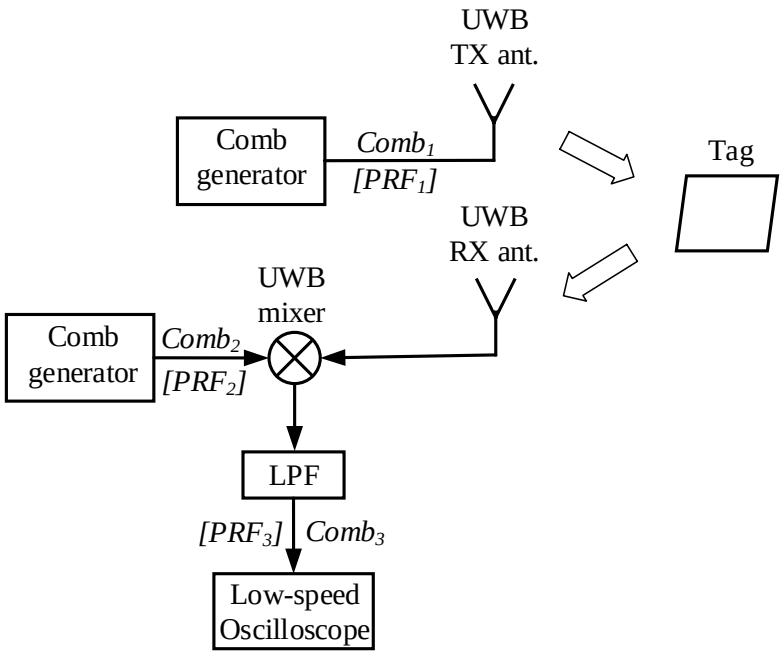

Figure 3.16: Block diagram of dual-comb UWB Chipless RFID system.

rates called PRF_1 and PRF_2, respectively. $Comb_1$ interrogates the tag, and the response of the tag, which contains the frequency signature of the tag, is amplified and then mixed with $Comb_2$. The frequency mixing of two UWB frequency combs with slightly different repetition rates, maps the entire UWB signature of the Chipless RFID into the baseband (BB) frequency. The mixer output contains a third comb, $Comb_3$, expanded in time-domain and condensed in frequency-domain, and holds the UWB information from the tag. The mixer output is passed though the LPF to keep $Comb_3$ and to cancel out any term that can exist at higher frequencies and cause anti-aliasing. Then, $Comb_3$ is sampled by the low-speed oscilloscope. Dual-comb technique eliminates the need for low-speed oscilloscope and it significantly reduces the receiver complexity.

One-to-one mapping of the UWB properties of the tag into $Comb_3$ requires that PRF_1 and PRF_2 meet the following criteria [42]:

$$BW_{UWB} \leq \frac{{PRF_1}^2}{2(|PRF_2 - PRF_1|)}. \tag{3.3}$$

where BW_{UWB} is the microwave UWB bandwidth (7 GHz) that $Comb_1$, $Comb_2$, and the tag response are extended in that range. Therefore, PRF_1 and PRF_2 are selected to be 10 MHz and 10.002 MHz, respectively. The 2 kHz difference between PRF_1 and PRF_2 will be the repetition rate of $Comb_3$ [7] as given below:

$$PRF_3 = PRF_2 - PRF_1. \tag{3.4}$$

While $Comb_1$ and $Comb_2$ are in the frequency range of 3 GHz - 10 GHz, $Comb_3$ is extended in the range of 0.6 MHz - 2 MHz. The ratio of PRF_1 and PRF_3 is called compression factor , m, as defined below:

$$m = \frac{PRF_1}{PRF_3}. \tag{3.5}$$

In such frequency plan, the compression factor is 5000. As an example, if a resonance in the tag response occurs at 8 GHz, this resonance will show itself at 8 GHz/5000 = 1.6 MHz in $Comb_3$ waveform. The comb lines of $Comb_3$ are spaced 2 kHz far apart and $Comb_3$ must have acceptable resolution to resolve the comb lines. To achieve a frequency resolution of 0.2 kHz with FFT, the duration of $Comb3$ must be 5 ms. The higher duration in time-domain will give the higher resolution in frequency domain.

The output of the proposed system results from the interaction of multiple sources operating at different frequencies and this method of measurement depends on averaging the output signal to increase the signal-to-noise ratio (SNR). In this regard, it is necessary to freeze the output waveform on oscilloscope through synchronizing all clock sources involved in the system.

Fig. 3.17 shows simulated $Comb_1$ and $Comb_2$ in time and frequency domains. For better visibility, only a small span of the signals are shown. Fig. 3.17 (a) shows 5 ns duration of $Comb_1$ and $Comb_2$ in time domain. Since $Comb_2$ has slightly higher PRF, it appears first in the figure before $Comb_1$ occurs. The simulated time-domain combs in the time duration of 0.5 ms, results in the equivalent spectrum shown in Fig. 3.17 (b) where only a small span of the spectrum is

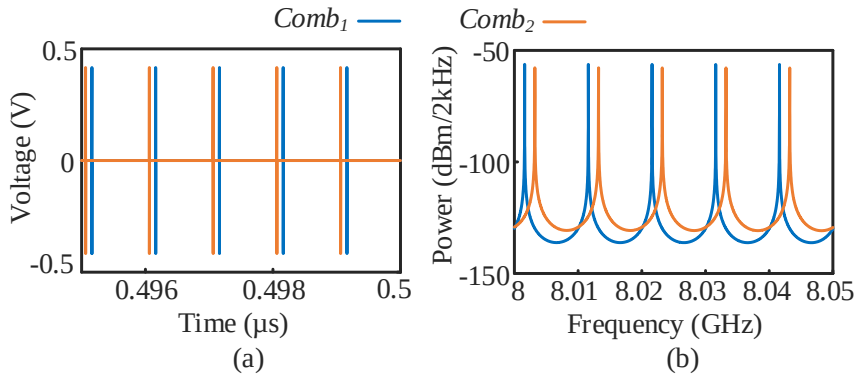

Figure 3.17: Simulated $Comb_1$ and $Comb_2$ in (a) time and (b) frequency domains.

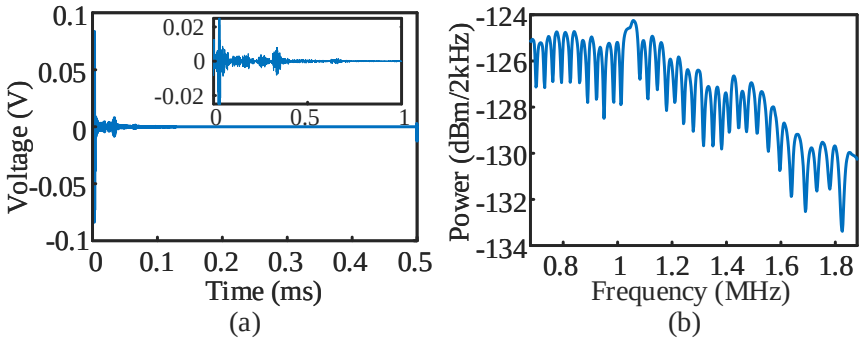

Figure 3.18: Simulated dual-comb output ,$Comb_3$, in (a) time and (b) frequency domains.

shown. Again, because $Comb_2$ has slightly higher PRF, each tooth of $Comb_2$ appears at higher frequency than $Comb_1$. This difference is increased by 2 kHz with every comb tooth. Although the dual-comb system does not require the direct acquisition of $Comb_1$ and $Comb_2$ in 3- 10 GHz range shown in Fig. 3.17, they have been simulated in the system to present step-by-step operation of the system. While the simulation is for the span of 0.5 ms of the inputs, with a larger simulation span the two combs could be spectrally resolved better even below -120 dBm/2kHz with the cost of higher computation. In conclusion, if the simulation time is longer, the cross talk between the combs is smaller.

Fig. 3.18 shows the output of dual-comb system in time and frequency domains. The time domain output signal, shown in the span of 0.5 ms, and it will give a frequency resolution of 2 kHz

after FFT. The frequency resolution of 2 kHz in BB is translated to the resolution of m*2 kHz = 10 MHz in UWB. The equivalent frequency domain output is shown in Fig. 3.18 (b). As can be seen, the tag resonances from 3 GHz to 10 GHz are appeared in the amplitude information of the output spectrum and in they are in the range of 0.6 MHz to 2 MHz. The reduction in the complexity of the receive is significant, because the output in the range of 0.6 MHz to 2 MHz can be easily captured with a low speed oscilloscope or ADC card with the sampling rates of a few ten MHz.

3.2.3 Implementation and Measurement Results

3.2.3.1 Multiresonator measurement results

The 32-bit multiresonator is fabricated on RO4350B substrate with thickness = 0.338 mm, ϵ_r = 3.66, and tanδ = 0.0031 as shown in Fig. 3.19 (a). The total size of multiresonator is 3.2 cm$\times$ 6.5 cm and the measured response of multiresonator by network analyzer is shown in Fig. 3.19 (b). The numbers of 32 separate resonances are labeled in the figure. Although the resonators with close resonance frequencies are printed far from each other, it can be seen that the quality factors of the resonators are not entirely uniform. This response could be improved by realigning the resonators or increasing the spacing between them. Because the focus of this work is to evaluate different time-domain readers, the current multiresonator and its tag are considered as the reference in the next measurements.

Fig. 3.20 shows the setup of IR-UWB system for measuring transmission response of the multiresonator. This system includes a Keysight M8195A 65 GSa/s arbitrary waveform generator (AWG), the 32-bit multiresonator, and a DSA91304A 40 GSa/s infiniium oscilloscope.

The M8185A AWG generates a narrow pulse with the duration of approximately 0.5 ns and a 10-dB bandwidth of 7 GHz extended from 3 to 10 GHz (Fig. 3.21 (a) and (c)). The repetition rate of this pulse is 10 MHz. The response of multiresonator to this pulse in time and frequency domains are shown in Figs 3.21 (b) and (c), respectively. The time-domain response has a tail of about 10 ns that contains the multiresonant information. The frequency domain that has been calculated by taking FFT of the time-domain response shows 32 resonances from 3 to 10 GHz.

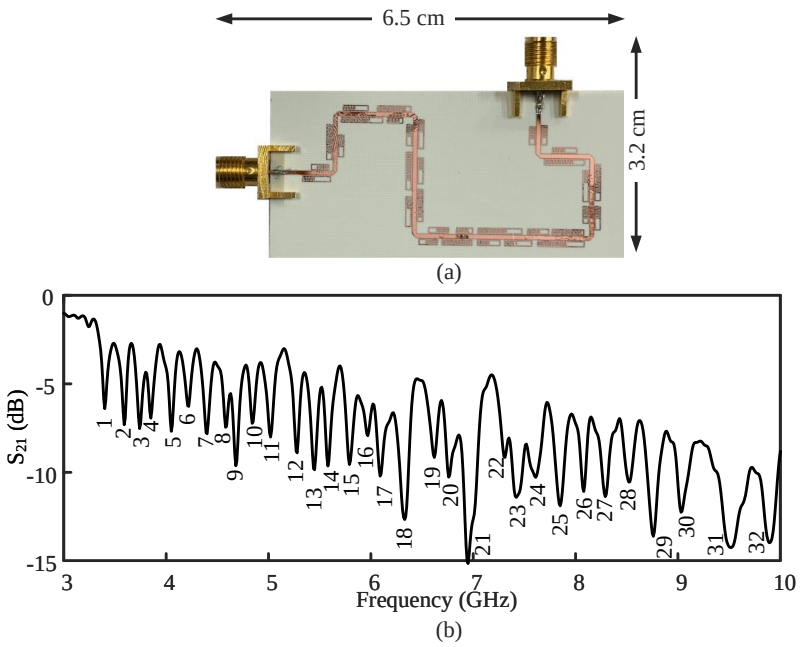

Figure 3.19: (a) Photograph of fabricated 32-bit multiresonator and (b) measured S_{21} of multiresonator.

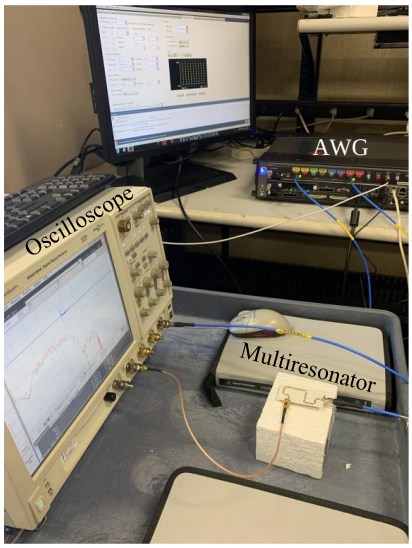

Figure 3.20: Photograph of measurement setup.

The multiresonator response normalized to the input response is shown in Fig. 3.21 (c).

For testing CP-FTMW technique, the AWG generates an up-chirp signal with the duration of

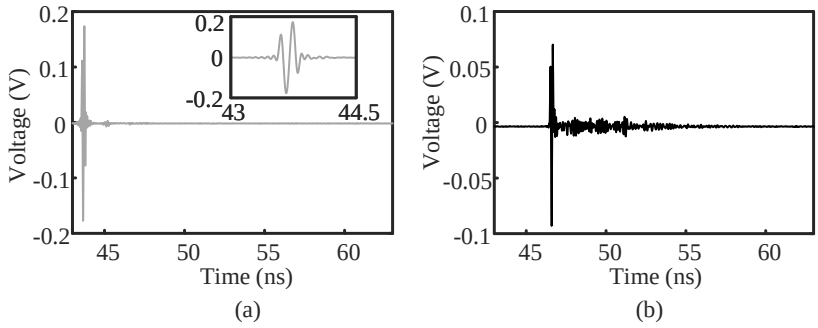

Figure 3.21: (a) Input and (b) output voltages of multiresonator in IR-UWB system. (c) Input and output of multiresonator with IR-UWB system in frequency domain

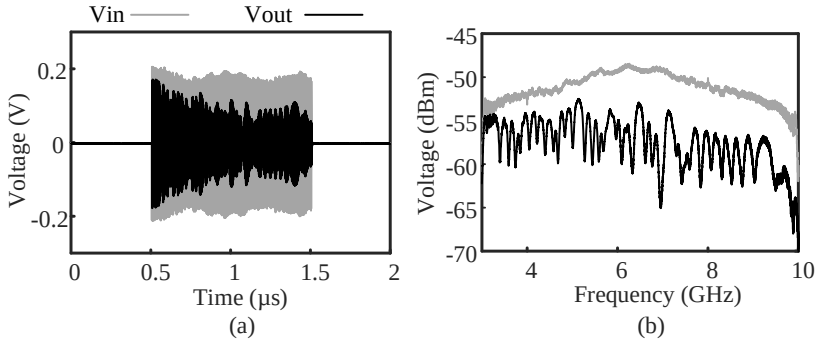

Figure 3.22: (a) Input and (b) output of multiresonator with CP-FTMW system in time domain. (c) Input and output of multiresonator with CP-FTMW system in frequency domain.

1 μs and period of 2 μs as shown in Fig. 3.22(a). The time-domain response of the multiresonator is shown in Fig. 3.22(b). It can be seen that in the time-domain response, 32 resonances are generated. By taking the FFT of input and output voltages, the frequency domain response is shown in Fig. 3.22(c). The frequency response of the multiresonator has 32 resonances as expected.

The setup in Fig. 3.20 is modified to measure the multiresonator response with dual-comb technique as following. Because the repetition rates of $Comb_1$ and $Comb_2$ are too close, it is not possible to independently generate the two combs from one M8195A AWG due to memory limitation. Therefore, $Comb_1$ is generated by an 8719ES 13.5 GHz VNA and $Comb_2$ is generated by the AWG. While the AWG generates $Comb_2$ with time-domain technique, the VNA generates $Comb_1$ with frequency-domain technique through frequency sweeping. In other words, all teeth of

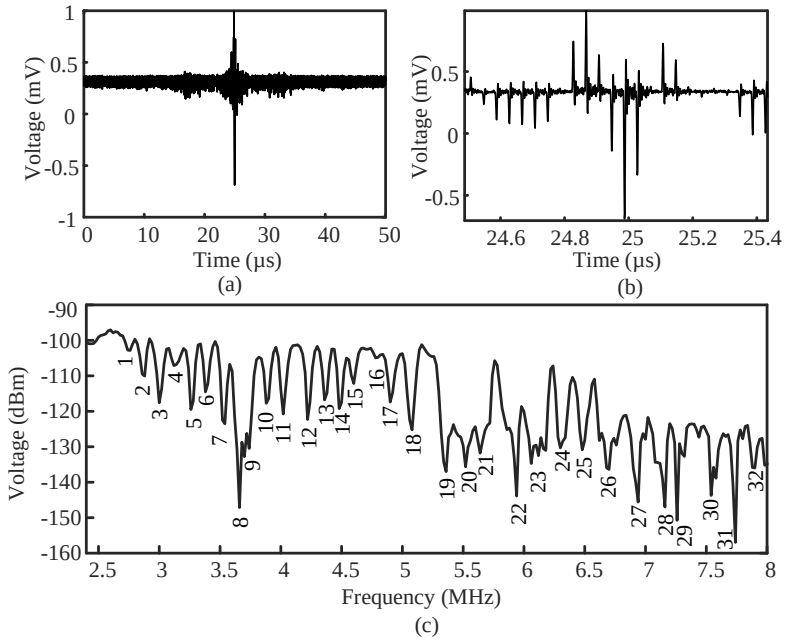

Figure 3.23: Output of multiresonator with dual-comb system in (a) and (b) time domain (zoomed-in) and (c) frequency domain.

$Comb_2$ simultaneously generated but the teeth of $Comb_1$ are sequentially generated. As the result, the output of dual-comb system is gradually generated. When the output is gradually generated with the sweeping speed of the VNA, special consideration is needed for averaging the output. The oscilloscope should be able to capture and average all tones generated by the VNA. For that purpose, the sweeping speed of VNA is reduced to 5 sec to allow oscilloscope captures the entire VNA output. $Comb_1$ is generated from port 1 of the VNA while port 1 is set to measure S_{11} with the start time of 1 GHz, stop time of 11 GHz, number of points 401, and sweep time of 5 seconds. This setting results in the PRF of 25 MHz for $Comb_1$. It is worthwhile mentioning that when the oscilloscope averages VNA output with the abovementioned setting, with the accumulation of all VNA tones by the oscilloscope, the signal on the screen of oscilloscope looks like a short-duration time-domain pulse.

For mixing of the two combs, an HMC787ALCB mixer is used and an 80-MHz VLF-80+ LPF used as low pass filter. The PRF of $Comb_1$ is 25 MHz and the PRF of $Comb_2$ is selected to 25.02 MHz. With such setting, the compression factor is m = (25 MHz)/(20 kHz) = 1250. It

means that 3 GHz is mapped to 2.4 MHz and 10 GHz is mapped to 8 MHz. From Fig. 3.23 (b), all resonance frequencies can be seen, however, it should be noted that the result is not exactly the same as the other techniques. First, the signal level is smaller and therefore needs a longer time of averaging (about 50 times larger number of averaging). Second, the spectrum shape in dual-comb technique is the result of mixing LO and RF combs, and the amplitude of IF signal is the result of multiplication of corresponding teeth of RF and LO amplitudes.

Fig. 3.23 shows the output of dual-comb system in time and frequency domains. Fig. 3.23 (a) is one period of dual-comb system output in time-domain which is equal to 50 μs (= 1/20 kHz). The zoomed-in version of the output dual-comb output in duration of 1 μs is presented in Fig. 3.23 (b). It is seen that in the time-domain signal, $Comb_1$ is sampled by $Comb_2$ with the period of 40 ns (= 1/25 MHz). Fig. 3.23 (c) shows the FFT of system output where the 32 resonances are labeled. With a low frequency amplifier after filtering, the output spectrum density can be increased. The dual-comb output is captured with the sampling rate of 200 MHz. Number of averaging on oscilloscope is 4096.

3.2.3.2 Comparison among different techniques

The IR-UWB, CP-FTMW, and dual-comb techniques were demonstrated. With the same amplitude levels, the IR-UWB signal has small power density compared to CP-FTMW as shown in Fig. 3.21 (c) and Fig. 3.22 (c). With IR-UWB systems, because of the short duration of pulse in time domain (about 0.5 ns), it is possible to measure and quantify coupling effect, multiple reflection, and multipath in various systems, but CP-FTMW does not provide this flexibility. However, the CP-FTMW system could provide time and frequency signatures of the multiresonator even without the need for taking FFT (Fig. 3.22 (b)). Dual comb technique offers extensive reduction in receiver complexity. While IR-UWB and CP-FTMW systems need the sampling rates of at least 20 GSa/s, the dual-comb technique needs sampling rate of 160 MSa/s twice the cutoff frequency of LPF and it could be reduced to 16 MSa/s with an LPF of 8 MHz cutoff frequency. The accuracy is measured with the amount of SNR in receiver. Because CP-FTMW provides the higher power spectrum density, for the same amount of averaging time, CP-FTMW offers better accuracy com-

pared with IR-UWB technique. Dual-comb system needs averaging because of two reasons: one is the sweeping nature of VNA output and the other, the same as IR-UWB, is the short duration of pulse in a complete period. For this reason, the dual-comb system demonstrated in this paper needs longer averaging time compared to CP-FTMW and IR-UWB to reach high accuracy. The number of 128 averaging for IR-UWB and CP-FTMW systems is about 10 seconds while the number of 4096 averaging for dual-comb system is about three minutes.

One period of IR-UWB, CP-FTMW, and dual-comb signals are of 0.1 μs, 2 μs, and 50 μs, respectively. Therefore, the frequency resolutions of IR-UWB, CP-FTMW, and dual-comb signals are 10 MHz, 2 MHz, and 25 MHz, respectively. In order to measure a higher capacity tag with more tight resonance frequencies, the dual-comb system requires a smaller repetition rate than 25 MHz.

Table 3.3: Table of comparison between time-domain readers for Chipless RFID systems.

Time-domain technique	Speed	Frequency resolution	Receiver complexity
IR-UWB	Moderate	Low	High
CP-FTMW	High	High	High
Dual comb	Low	Moderate*	Low

* Adjustable by the repetition rate of the frequency combs

Table 3.3 compares various time-domain readers for Chipless RFID applications. CP-FTMW technique outperforms other time-domain readers in terms of speed, signal-to-noise ratio and frequency resolution. On the other hand, dual-comb technique is superior if system simplicity is concerned.

3.2.3.3 Chipless RFID tag measurement results

Fig. 3.24 shows photograph of IR-UWB system for tag measurements. In this system, two 3164-05 open boundary quad-ridged horn antennas are used as the reader antennas. The IR-UWB

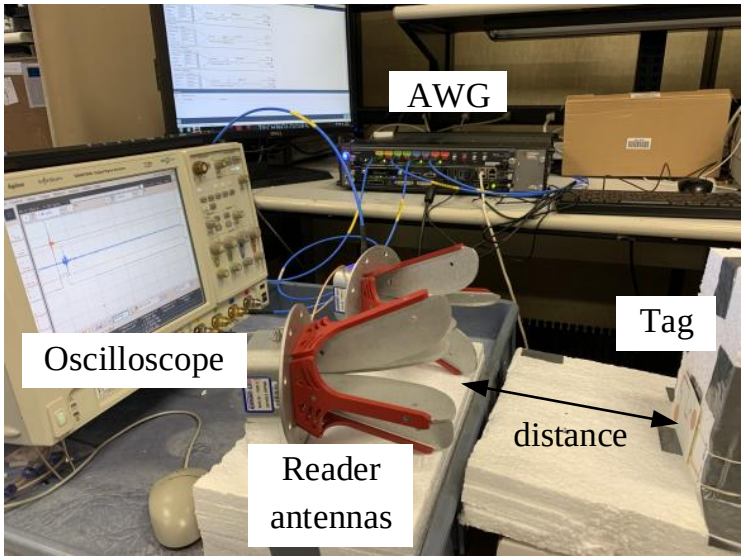

Figure 3.24: Setup of tag measurement with IR-UWB technique.

system of measurement has been selected in order to separately show coupling between reader antennas. The input voltage of the system generated by the AWG has 0.8 V_{pp} amplitude in time domain as shown in Fig. 3.25. The environment response which includes the signal coupled from the transmitter reader antenna to the receiver reader antenna is shown in Fig. 3.25 with the peak-to-peak voltage of less than 2 mV appears at 6 ns. This coupled response is present in all tag measured results with various reading distances (20, 30, and 40 cm). As can be seen from Fig. 3.25, measured with 1024 number of averaging, the response due to the tag at distance of 20 cm is seen about 1.5 ns after the coupling response. Therefore, the coupling response can be either windowed or subtracted from the total tag response. The 1024 number of averaging is to overcome the path loss from transmitter to the receiver antenna. At distance of 30 cm, the same coupled response is present, and the actual tag response is seen with a larger delay and a lower amplitude compared to the case of 20 cm distance. This delay is further increased and amplitude is decreased at 40 cm distance. After subtracting the coupled response from complete tag response at the distance of 40 cm and then taking FFT, the response of chipless RFID tag in frequency-domain

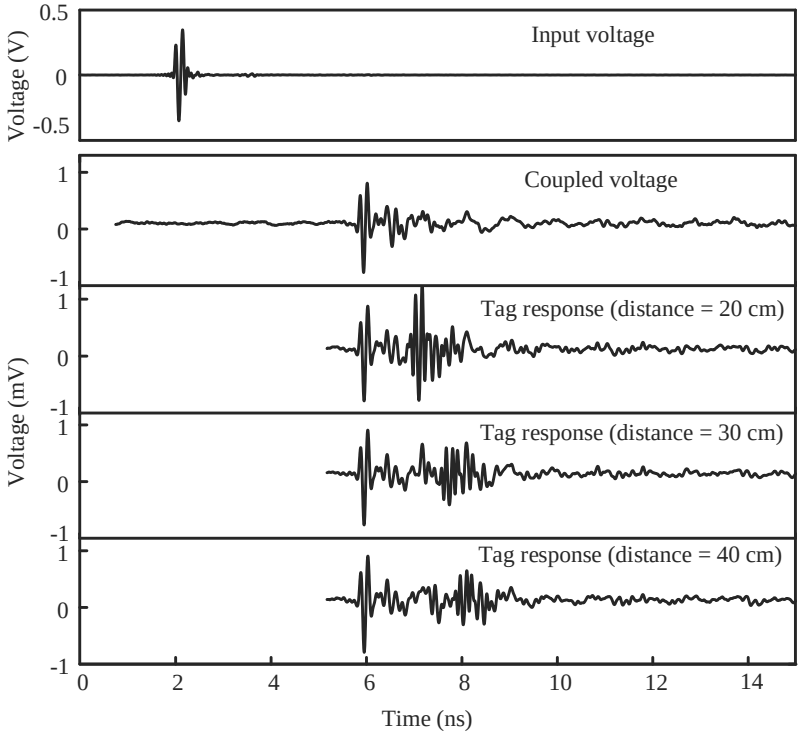

Figure 3.25: Measured input IR-UWB voltage, coupled voltage from reader antennas, and tag response from 20, 30, and 40 cm distances.

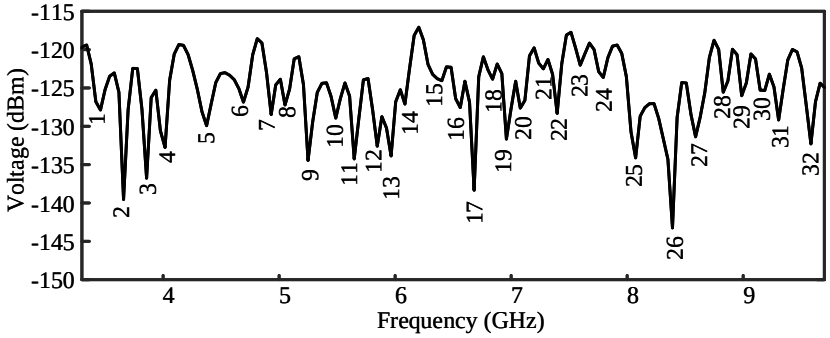

Figure 3.26: Response of chipless RFID tag at distance of 40 cm.

is calculated to be as shown in Fig. 3.26. As can be seen from this figure, the chipless RFID tag in frequency-domain has 32 resonances labeled in Fig. 3.26.

3.2.4 Conclusion

Three time-domain readers and a 32-bit tag for ultra-wideband (UWB) chipless RFID applications have been designed and implemented in this paper. The readers include IR-UWB, CP-FTMW, and dual-comb. In IR-UWB, the coupling effect between TX and RX antennas can be separated from the tag response from time-domain results. CP-FTMW is high-resolution, high SNR, and fast technique by sending a chirp extended through a long time compared with the IR-UWB short pulse. Unlike IR-UWB and CP-FTMW methods, the dual-comb technique requires a simple receiver with low sampling rate to extract UWB information from the UWB multiresonator/tag.

4. SUMMARY AND CONCLUSIONS

Time-domain dielectric spectroscopy can be considered as an alternative to frequency-domain dielectric spectroscopy. In this proposal, several time-domain UWB dielectric spectroscopy systems have been implemented to prove the strength of this technique. These systems included a contactless spectroscopy system by using Vivaldi antennas and a contact-based system with planar periodic sensing structures. In addition, a dual-comb spectroscopy system that greatly reduces the system complexity is implemented as an accurate, fast, and low-cost time-domain spectroscopy system with the possibility of being self-sustained and independent of laboratory facility.

Time-domain technique is a viable solution for UWB Chipless RFID readers. The successful demonstrations of time-domain readers based IR-UWB, Chirped pulse Fourier transform Microwave, and dual-comb techniques have been presented in this thesis.

REFERENCES

[1] R. Ebrahimi Ghiri, A. Pourghorban Saghati, E. Kaya, and K. Entesari, "A miniaturized contactless uwb microwave system for time-domain dielectric spectroscopy," *IEEE Trans. Microw. Theory Techn.*, vol. 65, pp. 5334–5344, Dec 2017.

[2] R. Ebrahimi Ghiri, A. P. Saghati, E. Kaya, and K. Entesari, "A 3-10 ghz contact-less complex dielectric spectroscopy system," in *Int. Microw. Symp. Dig.*, pp. 621–623, June 2017.

[3] J. Wu, Z. Zhao, Z. Nie, and Q. H. Liu, "A printed uwb vivaldi antenna using stepped connection structure between slotline and tapered patches," *IEEE Antennas and Wireless Propagation Letters*, vol. 13, pp. 698–701, 2014.

[4] R. E. Ghiri, E. Kaya, and K. Entesari, "A miniaturized 3-10 ghz time-domain contact-based dielectric spectroscopy system," in *IEEE MTT-S Int. Microw. Symp. Dig.*, IEEE, 2018.

[5] R. Ebrahimi Ghiri, E. Kaya, and K. Entesari, "Time-domain dielectric spectroscopy using a miniaturized contact-based uwb system," *IEEE Trans. Microw. Theory Techn.*, vol. 66, pp. 5863–5872, Dec 2018.

[6] R. E. Ghiri and K. Entesari, "A miniaturized 3-10ghz dual-comb spectroscopy system for chemical detection," in *Int. Microw. Symp. Dig.*, pp. 1492–1494, June 2019.

[7] R. Ebrahimi Ghiri and K. Entesari, "A miniaturized uwb microwave dual-comb dielectric spectroscopy system," *IEEE Transactions on Microwave Theory and Techniques*, vol. 67, no. 12, pp. 5218–5227, 2019.

[8] R. E. Ghiri and K. Entesari, "A 50.7-bit retransmission-based chipless rfid tag with miniaturized resonators,," in *2021 IEEE Topical Conference on Wireless Sensors and Sensor Networks (WiSNet)*, 2021.

[9] R. E. Ghiri and K. Entesari, "A frequency selective surface with miniaturized elements for chemical sensing," in *2019 IEEE Texas Symposium on Wireless and Microwave Circuits and*

Systems (WMCS), pp. 1–3, 2019.

[10] M. M. Bajestan, A. A. Helmy, H. Hedayati, and K. Entesari, "A 0.62–10 ghz complex dielectric spectroscopy system in cmos," *IEEE Transactions on Microwave Theory and Techniques*, vol. 62, no. 12, pp. 3522–3537, 2014.

[11] F. Kremer, "Dielectric spectroscopy–yesterday, today and tomorrow," *Journal of Non-Crystalline Solids*, vol. 305, no. 1-3, pp. 1–9, 2002.

[12] I. Ermolina, Y. Polevaya, Y. Feldman, B.-Z. Ginzburg, and M. Schlesinger, "Study of normal and malignant white blood cells by time domain dielectric spectroscopy," *IEEE Transactions on Dielectrics and Electrical Insulation*, vol. 8, no. 2, pp. 253–261, 2001.

[13] Y. Feldman, I. Ermolina, and Y. Hayashi, "Time domain dielectric spectroscopy study of biological systems," *IEEE transactions on dielectrics and electrical insulation*, vol. 10, no. 5, pp. 728–753, 2003.

[14] B. P. Kwok, S. O. Nelson, and E. Bahar, "Time-domain measurements for determination of dielectric properties of agricultural materials," *IEEE Transactions on Instrumentation and Measurement*, vol. 28, no. 2, pp. 109–112, 1979.

[15] D. K. Ghodgaonkar, V. V. Varadan, and V. K. Varadan, "A free-space method for measurement of dielectric constants and loss tangents at microwave frequencies," *IEEE Transactions on Instrumentation and Measurement*, vol. 38, pp. 789–793, Jun 1989.

[16] J. Han and C. Nguyen, "Development of a tunable multiband uwb radar sensor and its applications to subsurface sensing," *IEEE Sensors Journal*, vol. 7, pp. 51–58, Jan 2007.

[17] I. Vakili, L. Ohlsson, L. E. Wernersson, and M. Gustafsson, "Time-domain system for millimeter-wave material characterization," *IEEE Transactions on Microwave Theory and Techniques*, vol. 63, pp. 2915–2922, Sept 2015.

[18] Z. Akhter and M. J. Akhtar, "Free-space time domain position insensitive technique for simultaneous measurement of complex permittivity and thickness of lossy dielectric samples," *IEEE Transactions on Instrumentation and Measurement*, vol. 65, pp. 2394–2405, Oct 2016.

[19] M. Zhao, J. D. Shea, S. C. Hagness, and D. W. van der Weide, "Calibrated free-space microwave measurements with an ultrawideband reflectometer-antenna system," *IEEE Microwave and Wireless Components Letters*, vol. 16, pp. 675–677, Dec 2006.

[20] Y. Feldman, I. Ermolina, and Y. Hayashi, "Time domain dielectric spectroscopy study of biological systems," *IEEE Transactions on Dielectrics and Electrical Insulation*, vol. 10, pp. 728–753, Oct 2003.

[21] A. A. Helmy and K. Entesari, "A 1–8-ghz miniaturized spectroscopy system for permittivity detection and mixture characterization of organic chemicals," *IEEE transactions on microwave theory and techniques*, vol. 60, no. 12, pp. 4157–4170, 2012.

[22] K. Saeed, A. C. Guyette, I. C. Hunter, and R. D. Pollard, "Microstrip resonator technique for measuring dielectric permittivity of liquid solvents and for solution sensing," in *2007 IEEE/MTT-S International Microwave Symposium*, pp. 1185–1188, IEEE, 2007.

[23] A. P. Saghati, J. S. Batra, J. Kameoka, and K. Entesari, "A metamaterial-inspired wideband microwave interferometry sensor for dielectric spectroscopy of liquid chemicals," *IEEE Transactions on Microwave Theory and Techniques*, vol. PP, no. 99, pp. 1–14, 2017.

[24] H. Hedayati and K. Entesari, "A 90-nm cmos uwb impulse radio transmitter with 30-db in-band notch at ieee 802.11a system," *IEEE Transactions on Microwave Theory and Techniques*, vol. 61, no. 12, pp. 4220–4232, 2013.

[25] C. A. Balanis, *Antenna Theory: Analysis and Design*. John Wiley Sons, second ed., 1997.

[26] R. Ebrahimi Ghiri, A. Pourghorban Saghati, E. Kaya, and K. Entesari, "A 3-10 ghz contactless complex dielectric spectroscopy system," in *IEEE MTT-S Int. Microw. Symp. Dig., accepted for presentation,*, Jun. 2017.

[27] J. L. Moll and S. A. Hamilton, "Physical modeling of the step recovery diode for pulse and harmonic generation circuits," *Proceedings of the IEEE*, vol. 57, pp. 1250–1259, July 1969.

[28] J. Han and C. Nguyen, "On the development of a compact sub-nanosecond tunable monocycle pulse transmitter for uwb applications," *IEEE Transactions on Microwave Theory and Techniques*, vol. 54, pp. 285–293, Jan 2006.

[29] T. Xia, A. S. Venkatachalam, and D. Huston, "A high-performance low-ringing ultrawideband monocycle pulse generator," *IEEE Transactions on Instrumentation and Measurement*, vol. 61, pp. 261–266, Jan 2012.

[30] J. Zhang and A. Raisanen, "A new model of step recovery diode for cad," in *Proceedings of 1995 IEEE MTT-S International Microwave Symposium*, pp. 1459–1462 vol.3, May 1995.

[31] V. Sekar, W. J. Torke, S. Palermo, and K. Entesari, "A self-sustained microwave system for dielectric-constant measurement of lossy organic liquids," *IEEE Transactions on Microwave Theory and Techniques*, vol. 60, no. 5, pp. 1444–1455, 2012.

[32] F. Buckley, "Tables of dielectric dispersion data for pure liquids and dilute solutions," *Natl. Bur. Stand. Circ.*, vol. 589, pp. 7–8, 1958.

[33] H. Fröhlich, *Theory of dielectrics: dielectric constant and dielectric loss*. Clarendon Press, 1958.

[34] I. Bahl and S. S. Stuchly, "Analysis of a microstrip covered with a lossy dielectric," *IEEE Trans. Microw. Theory Tech.*, vol. 28, no. 2, pp. 104–109, 1980.

[35] G. Gonzalez, *Microwave Transistor Amplifiers Analysis and Design, 2nd*. Prentice hall, 1997.

[36] K. Entesari and A. P. Saghati, "Fluidics in microwave components," *IEEE Microw. Mag.*, vol. 17, no. 6, pp. 50–75, 2016.

[37] G. Natta and P. Corradini, "Structure and properties of isotactic polypropylene," *Il Nuovo Cimento (1955-1965)*, vol. 15, no. 1, pp. 40–51, 1960.

[38] A. P. Saghati and K. Entesari, "A uwb near-field contactless sensor for solid and liquid material characterization," in *Proc. IEEE Int. Symp. Antennas Propag. USNC/URSI Nat. Radio Sci. Meeting*, pp. 901–902, IEEE, 2017.

[39] Keysight Technologies, *Dielectric Probe Kit 10MHz to 50GHz*, 2 2018.

[40] R. E. Ghiri, A. P. Saghati, E. Kaya, and K. Entesari, "A 3–10 ghz contact-less complex dielectric spectroscopy system," in *2017 IEEE MTT-S International Microwave Symposium (IMS)*, pp. 621–623, IEEE, 2017.

[41] S. B. Jones, J. M. Wraith, and D. Or, "Time domain reflectometry measurement principles and applications," *Hydrological processes*, vol. 16, no. 1, pp. 141–153, 2002.

[42] I. Coddington, N. Newbury, and W. Swann, "Dual-comb spectroscopy," *Optica*, vol. 3, no. 4, pp. 414–426, 2016.

[43] S. Schiller, "Spectrometry with frequency combs," *Opt. Lett.*, vol. 27, pp. 766–768, May 2002.

[44] Z. Chen, T. W. Hänsch, and N. Picqué, "Mid-infrared feed-forward dual-comb spectroscopy," *Proc. Natl. Acad. Sci.*, vol. 116, no. 9, pp. 3454–3459, 2019.

[45] Z. Chen, M. Yan, T. W. Hänsch, and N. Picqué, "A phase-stable dual-comb interferometer," *Nat. Commun.*, vol. 9, no. 1, p. 3035, 2018.

[46] G. Millot, S. Pitois, M. Yan, T. Hovhannisyan, A. Bendahmane, T. W. Hänsch, and N. Picqué, "Frequency-agile dual-comb spectroscopy," *Nat. Photonics*, vol. 10, no. 1, p. 27, 2016.

[47] P. Martín-Mateos, B. Jerez, and P. Acedo, "Dual electro-optic optical frequency combs for multiheterodyne molecular dispersion spectroscopy," *Optics express*, vol. 23, no. 16, pp. 21149–21158, 2015.

[48] N. Picqué and T. W. Hänsch, "Frequency comb spectroscopy," *Nat. Photonics*, vol. 13, no. 3, pp. 146–157, 2019.

[49] T. Hilgeman, "Phase correction in fourier transform spectroscopy," *Astron. Astrophys.*, vol. 15, p. 399, 1974.

[50] T. Ideguchi, A. Poisson, G. Guelachvili, N. Picqué, and T. W. Hänsch, "Adaptive real-time dual-comb spectroscopy," *Nat. Commun.*, vol. 5, p. 3375, 2014.

[51] A. Pourghorban Saghati, J. S. Batra, J. Kameoka, and K. Entesari, "A metamaterial-inspired wideband microwave interferometry sensor for dielectric spectroscopy of liquid chemicals," *IEEE Trans. Microw. Theory Techn.*, vol. 65, pp. 2558–2571, July 2017.

[52] A. P. Gregory and R. Clarke, *Tables of the complex permittivity of dielectric reference liquids at frequencies up to 5 GHz.* National Physical Laboratory Teddington, 2001.

[53] A. Sihvola, "Mixing rules with complex dielectric coefficients," *Subsurface Sens. Technol. Appl.*, vol. 1, no. 4, pp. 393–415, 2000.

[54] S. Tedjini, N. Karmakar, E. Perret, A. Vena, R. Koswatta, and R. E-Azim, "Hold the chips: Chipless technology, an alternative technique for rfid," *IEEE Microwave Magazine*, vol. 14, pp. 56–65, July 2013.

[55] S. Preradovic, I. Balbin, N. C. Karmakar, and G. F. Swiegers, "Multiresonator-based chipless rfid system for low-cost item tracking," *IEEE Transactions on Microwave Theory and Techniques*, vol. 57, pp. 1411–1419, May 2009.

[56] C. M. Nijas, R. Dinesh, U. Deepak, A. Rasheed, S. Mridula, K. Vasudevan, and P. Mohanan, "Chipless rfid tag using multiple microstrip open stub resonators," *IEEE Transactions on Antennas and Propagation*, vol. 60, pp. 4429–4432, Sep. 2012.

[57] Y. J. Zhang, R. X. Gao, Y. He, and M. S. Tong, "Effective design of microstrip-line chipless rfid tags based on filter theory," *IEEE Transactions on Antennas and Propagation*, vol. 67, pp. 1428–1436, March 2019.

[58] B. Shao, Y. Amin, Q. Chen, R. Liu, and L. Zheng, "Directly printed packaging-paper-based chipless rfid tag with coplanar lc resonator," *IEEE Antennas and Wireless Propagation Letters*, vol. 12, pp. 325–328, 2013.

[59] T. Athauda and N. Karmakar, "Chipped versus chipless rf identification: A comprehensive review," *IEEE Microwave Magazine*, vol. 20, no. 9, pp. 47–57, 2019.

[60] C. Herrojo, M. Moras, F. Paredes, A. Nunez, J. Mata-Contreras, E. Ramon, and F. Martin, "Time-domain-signature chipless rfid tags: Near-field chipless-rfid systems with high data capacity," *IEEE Microwave Magazine*, vol. 20, no. 12, pp. 87–101, 2019.

[61] F. Babaeian and N. C. Karmakar, "Hybrid chipless rfid tags- a pathway to epc global standard," *IEEE Access*, vol. 6, pp. 67415–67426, 2018.

[62] M. Garbati, E. Perret, R. Siragusa, and C. Halope, "Ultrawideband chipless rfid: Reader technology from sfcw to ir-uwb," *IEEE Microwave Magazine*, vol. 20, no. 6, pp. 74–88, 2019.

[63] J. Aliasgari, M. Forouzandeh, and N. Karmakar, "Chipless rfid readers for frequency-coded tags: Time-domain or frequency-domain," *IEEE Journal of Radio Frequency Identification*, pp. 1–1, 2020.

[64] M. Garbati, R. Siragusa, E. Perret, and C. Halopé, "Impact of an ir-uwb reading approach on chipless rfid tag," *IEEE Microwave and Wireless Components Letters*, vol. 27, no. 7, pp. 678–680, 2017.

[65] J. R. Fernandes and D. Wentzloff, "Recent advances in ir-uwb transceivers: An overview," in *Proceedings of 2010 IEEE International Symposium on Circuits and Systems*, pp. 3284–3287, 2010.

[66] G. G. Brown, B. C. Dian, K. O. Douglass, S. M. Geyer, S. T. Shipman, and B. H. Pate, "A broadband fourier transform microwave spectrometer based on chirped pulse excitation," *Review of Scientific Instruments*, vol. 79, no. 5, p. 053103, 2008.

[67] G. G. Brown, B. C. Dian, K. O. Douglass, S. M. Geyer, S. T. Shipman, and B. H. Pate, "A broadband fourier transform microwave spectrometer based on chirped pulse excitation," *Rev. Sci. Instrum.*, vol. 79, no. 5, p. 053103, 2008.

[68] G. B. Park and R. W. Field, "Perspective: The first ten years of broadband chirped pulse fourier transform microwave spectroscopy," *J. Chem. Phys.*, vol. 144, no. 20, p. 200901, 2016.

[69] M. Garbati, E. Perret, R. Siragusa, and C. Halopé, "Ultra-low-jitter fully tunable baseband pulse generator for uwb applications," *IEEE Transactions on Microwave Theory and Techniques*, vol. 66, no. 1, pp. 420–430, 2018.

[70] R. K. Dokania, X. Y. Wang, S. G. Tallur, and A. B. Apsel, "A low power impulse radio design for body-area-networks," *IEEE Transactions on Circuits and Systems I: Regular Papers*, vol. 58, no. 7, pp. 1458–1469, 2011.

[71] M. Garbati, R. Siragusa, E. Perret, A. Vena, and C. Halopé, "High performance chipless rfid reader based on ir-uwb technology," in *2015 9th European Conference on Antennas and Propagation (EuCAP)*, pp. 1–5, 2015.

[72] A. Mollfulleda, C. Ibars, J. A. Leyva, and L. Berenguer, "Practical demonstration of filter-bank receiver for ultra-wideband radios," in *2006 European Conference on Wireless Technology*, pp. 107–110, 2006.

[73] S.-D. Jang, B.-W. Kang, and J. Kim, "Frequency selective surface based passive wireless sensor for structural health monitoring," *Smart Materials and Structures*, vol. 22, no. 2, p. 025002, 2012.

[74] M. Mahmoodi and K. M. Donnell, "Performance metrics for frequency selective surface-based sensors," *IEEE Sensors Letters*, vol. 1, no. 6, pp. 1–4, 2017.

[75] K. Sarabandi and N. Behdad, "A frequency selective surface with miniaturized elements," *IEEE Transactions on Antennas and propagation*, vol. 55, no. 5, pp. 1239–1245, 2007.

[76] K. Song and P. Mazumder, "Design of highly selective metamaterials for sensing platforms," *IEEE Sensors Journal*, vol. 13, no. 9, pp. 3377–3385, 2013.

[77] O. Elhadidy, S. Shakib, K. Krenek, S. Palermo, and K. Entesari, "A wide-band fully-integrated cmos ring-oscillator pll-based complex dielectric spectroscopy system," *IEEE Transactions on Circuits and Systems I: Regular Papers*, vol. 62, no. 8, pp. 1940–1949, 2015.

[78] A. A. Helmy, H.-J. Jeon, Y.-C. Lo, A. J. Larsson, R. Kulkarni, J. Kim, J. Silva-Martinez, and K. Entesari, "A self-sustained cmos microwave chemical sensor using a frequency synthesizer," *IEEE journal of solid-state circuits*, vol. 47, no. 10, pp. 2467–2483, 2012.

APPENDIX A

FREQUENCY SELECTIVE SURFACES FOR SENSING *

A.1 Introduction

Frequency selective surfaces (FSSs) are usually constructed from periodic arrays of metallic geometries to manipulate the transmission and reflection properties of incident electromagnetic waves. In essence, FSSs have found widespread applications as spatial filters, reflectors and absorbers, and more recently as sensors [73], [74].

In this work, a spatial sensing architecture with miniaturized sub-wavelength elements is utilized. The proposed highly selective sensing structure is achieved by exploiting miniaturized-element frequency selective surfaces (MEFSS) including periodic arrays of lumped capacitive and inductive elements [75], [76]. Miniaturized lumped capacitive and inductive elements can be realized by printing various combinations of metallic patch and wire elements on very thin substrate, respectively. The detailed study in [76] shows that the parallel arrangement of loop and wire elements, outperforms the combination of patch and wire elements, patch and complementary loop elements, and loop and complementary loop elements in terms of narrow transmission bandwidth and selectivity for sensing. In [76], only the gap between capacitive loop elements is exposed to the material under test (MUT), while the effect of different MUTs on the inductive wire mesh response is considered negligible. In addition, the loop and wire elements are printed on two sides of a single substrate. The work presented in this paper, suggests printing loop and wire elements on one side of separate substrates and placing the liquid MUT inside a container between the elements. While the MUT is not in direct contact with the metallic elements, it effects the fringing field surrounding each element. This platform is designed and optimized, and the capability of the structure for sensing is demonstrated by showing the transmission characteristics through software

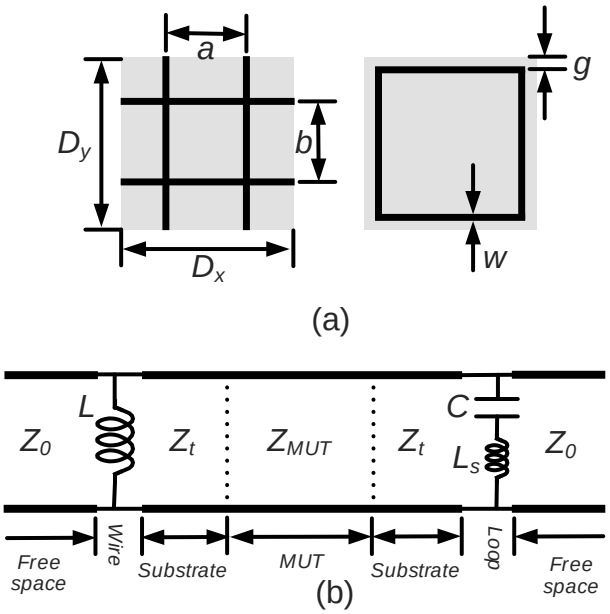

Figure A.1: (a) Unit cell of MEFSS with loop and wire elements, D_x=3.27mm, D_y=3.39mm, a=b=1.65mm, w=0.1mm, g=0.2mm, (b) Equivalent circuit model of the sensing platform for an incident TEM wave. Reprinted with permission from [9].

simulation.

A.2 Miniaturized-Element FSS Design for Sensing

In order to achieve a miniaturized and selective structure for sensing, the combination of wire grids and loop elements is employed. The unit cell of the MEFSS is shown in Fig. A.1(a) including the design parameters. For the purpose of sensing, the MUT is sandwiched between the wire elements and the loop elements periodically printed on separate thin substrates. The loop element has a capacitive property C in series with an inductor L_s, the wire element has an inductive property L, and the intrinsic characteristics of the MUT are modulated by the transmission line area, labeled as Z_{MUT}, as shown in the equivalent circuit model in Fig. A.1 (b). Z_t denotes the characteristic impedance of the substrate.

The lumped capacitive and lumped inductive properties of MEFSS coupled to the incident electric and magnetic waves, respectively, offer a miniaturized resonance sensing structure where the

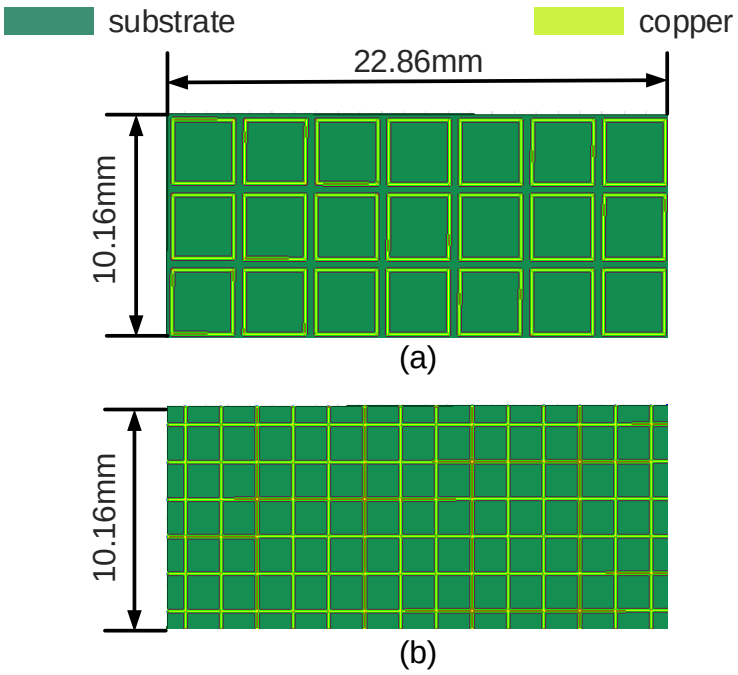

Figure A.2: (a) Periodic loop elements and (b) periodic wire elements printed on 0.338mm RO4350B substrate. Reprinted with permission from [9].

maximum dimension of each unit cell is $\sim 0.15\lambda$ at 10GHz. In order to show its sensing capability, the structure is simulated inside a standard X band WR90 waveguide with a finite periodic array of wire elements and loop elements on 0.338mm RO3450 substrate to cover the waveguide aperture area, 10.16mm$\times$22.86mm. With this area, each unit cell will be repeated 7$\times$3 times as shown in Fig. A.2. The simulation platform is shown in Fig. A.3. The substrates are aligned and attached to the opposite walls of a plastic container with the dielectric constant of 2.8 and the thickness of 4mm. A rectangular hollow area of 2mm width is created inside the container to carry the MUT. While the MEFSS elements are placed at the aperture of the waveguides, the MUT is outside of the waveguide and can be filled and emptied by different MUTs. The parameters of the wire grid and loop elements are obtained through optimization by HFSS finite element method (FEM), with the goal of successful detection of air, ethanol, and methanol in X band. The permittivity of air is considered to be 1 in simulations, while the complex permittivity of ethanol and methanol follow

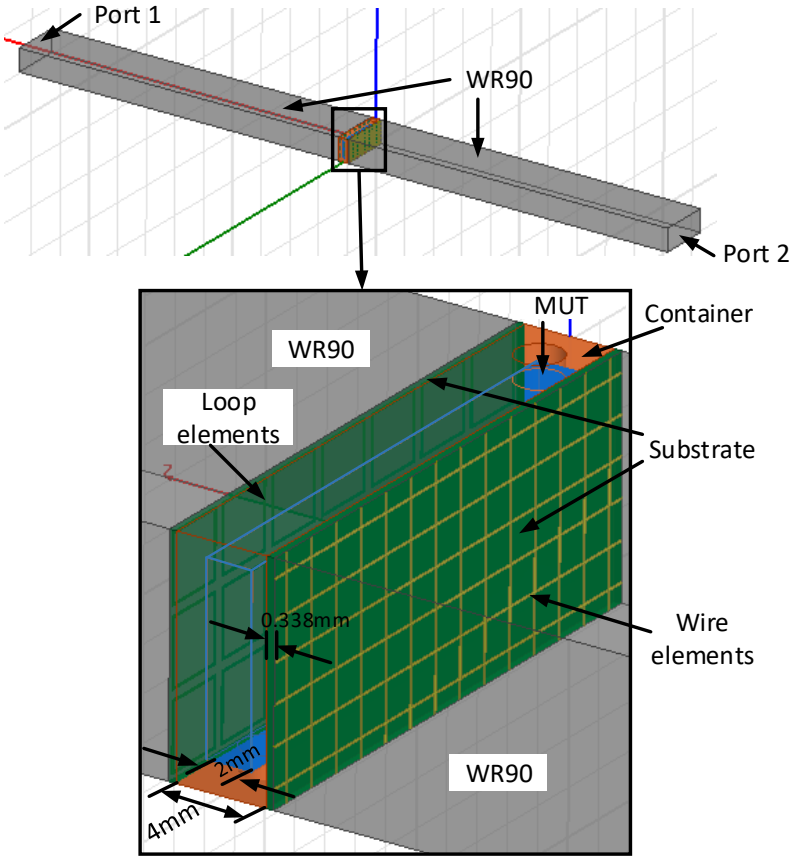

Figure A.3: Simulation setup of the MEFSS sensor. Reprinted with permission from [9].

Debye-Γ model and single-Debye model, respectively, as shown below [23]

$$\epsilon^*_{ethanol} = 4.505 + \frac{19.925}{1 + jf/(0.964 \times 10^9)} - jf \times 0.056, \tag{A.1}$$

$$\epsilon^*_{methanol} = 5.563 + \frac{27.097}{1 + jf/(3.141 \times 10^9)}. \tag{A.2}$$

A.3 MEFSS Sensor Full-Wave Results

Fig. A.4 shows the numerical simulation results of MEFSS sensing platform.

According to Fig. A.4, the resonance frequency and the resonance magnitude of S_{21} changes

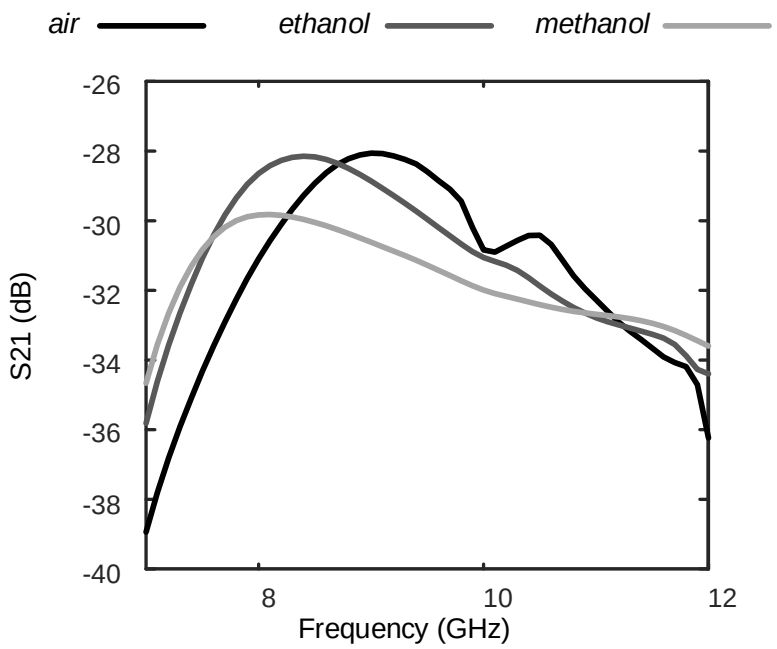

Figure A.4: Transmission results of the MEFSS sensor for three MUTs: air, ethanol, and methanol. Reprinted with permission from [9].

with different MUTs; therefore, this architecture can be used for sensing. The results are tabulated in Table A.1 for different MUTs. According to Table A.1, the resonance frequency shifts by 900MHz when the MUT changes from air to methanol. The resonance magnitude also changes by -1.76dB in that case. For the case of ethanol compared to air, the shifts in the resonance frequency and the resonance magnitude are 300MHz and -0.09dB, respectively. The smaller shift in the latter case is attributed to the smaller differences between both the ϵ' and ϵ'' of ethanol and air compared to the case of methanol-air.

Table A.1: Results of MUTs air, ethanol, and methanol at resonance. Reprinted with permission from [9].

MUT	Frequency (GHz)	Max(S_{21}) dB
air	9	-28.06
ethanol	8.4	-28.15
methanol	8.1	-29.82

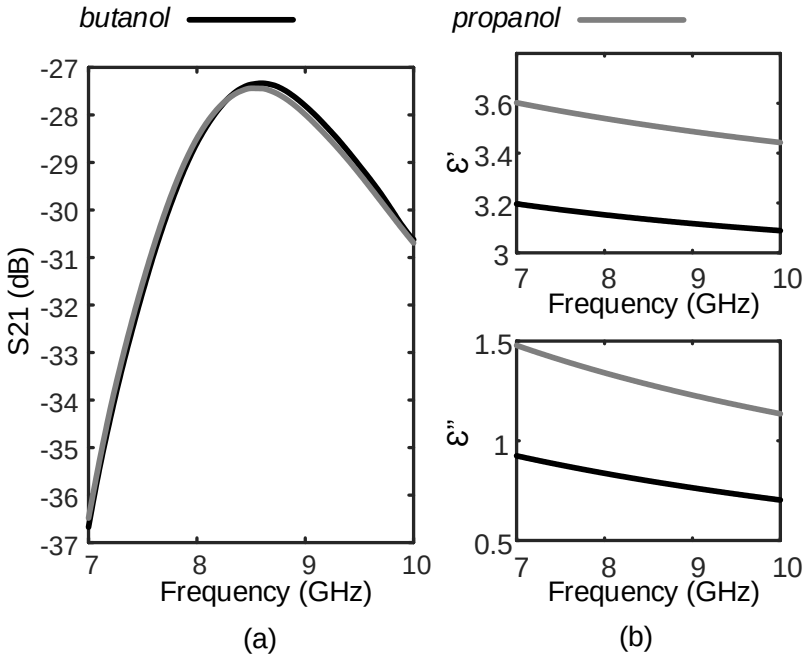

Figure A.5: (a) The MEFSS sensor transmission results for butanol and propanol, (b) ϵ' and ϵ'' of butanol and propanol. Reprinted with permission from [9].

In order to study the sensitivity of the MEFSS sensor, butanol and propanol, that have small differences in both their ϵ' and their ϵ'', are simulated and the S_{21} results are shown in Fig. A.5 and tabulated in Table A.2. As can be seen in Fig. A.5, the difference between ϵ' of butanol and propanol is in the range of 0.35-0.4 and it is in the range of 0.43-0.55 for their ϵ''. The difference in the resonance frequency of butanol and propanol is 80MHz and the difference in resonance magnitude is 0.11dB.

An interesting study could be to determine whether such small differences in ϵ' or ϵ'' of MUTs would give similar shifts in the resonance frequency and magnitude for large values of ϵ' and ϵ''. According to Table A.1, it is expected to achieve the same order of sensitivity for large ϵ' and ϵ'' values. It is because the resonance frequency shifts between air and ethanol (500MHz), and also between ethanol and methanol (400MHz) are almost in the same order. A similar statement can be made about resonance magnitude.

The dynamic range of the setup is evaluated by testing methanol-water mixtures [77] with

Table A.2: Results of butanol and propanol at resonance. Reprinted with permission from [9].

MUT	Frequency (GHz)	Max(S_{21}) dB
butanol	8.58	-27.33
propanol	8.5	-27.44

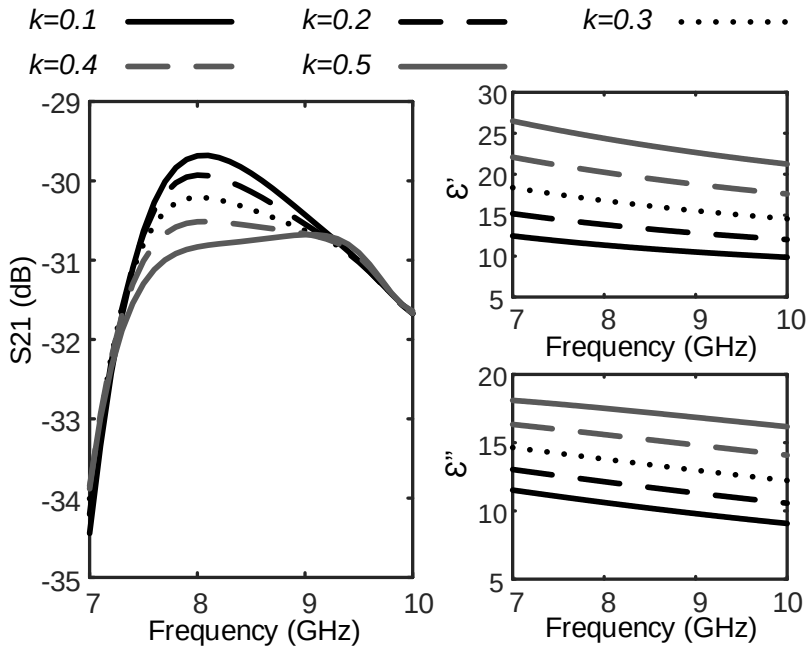

Figure A.6: (a) The MEFSS sensor transmission results for methanol-water mixtures with mixing ratios k=0.1, 0.2, 0.3, 0.4, 0.5, (b) ϵ' and ϵ'' of the mixtures. Reprinted with permission from [9].

mixing ratios of 0.1, 0.2, 0.3, 0.4, 0.5, defined as $k = \frac{V_{water}}{V_{total}}$ where V is referred to the liquid volume. Here, the Maxwell Garnett formula [78] is used to generate the complex permittivity of methanol-water mixtures and Fig. A.6 shows the simulation results. From this figure, the case k=0.5 does not show a peak resonance; hence, methanol-water mixture with k=0.5 (ϵ'=26.5-21.2 and ϵ''=18.1-16.1 in the 7-10GHz range) has the maximum possible ϵ' or ϵ'' that can be measured by the structure.

A.4 Conclusion

A sensing structure based on miniaturized-element frequency selective surfaces has been designed. The elements are periodic arrays of metallic wires and loops printed on separate thin substrates to exhibit inductive and capacitive behaviors, respectively. The transmission responses of the structure are affected by changing an MUT located between the two arrays. It has been shown that the structure is sensitive to little changes in ϵ' and ϵ'' as small as 0.4 and 0.55, respectively. Furthermore, The maximum dynamic range is 21.2 and 16.1 at 7-10GHz for ϵ' and ϵ'', respectively. Therefore, the propsed structure provides an accurate method for sensing chemicals in X band.